



Investigation of high-sensitivity superconducting HEB mixers for Antarctic astronomy

Kang-Min Zhou

► To cite this version:

Kang-Min Zhou. Investigation of high-sensitivity superconducting HEB mixers for Antarctic astronomy. Astrophysics [astro-ph]. Observatoire de Paris, 2015. English. NNT : . tel-02095300

HAL Id: tel-02095300

<https://hal.science/tel-02095300>

Submitted on 10 Apr 2019

HAL is a multi-disciplinary open access archive for the deposit and dissemination of scientific research documents, whether they are published or not. The documents may come from teaching and research institutions in France or abroad, or from public or private research centers.

L'archive ouverte pluridisciplinaire **HAL**, est destinée au dépôt et à la diffusion de documents scientifiques de niveau recherche, publiés ou non, émanant des établissements d'enseignement et de recherche français ou étrangers, des laboratoires publics ou privés.

OBSERVATOIRE DE PARIS

ECOLE DOCTORALE
ASTRONOMIE ET ASTROPHYSIQUE D' ILE-DE-FRANCE

Doctorat
ASTRONOMIE ET ASTROPHYSIQUE

AUTEUR: KANG-MIN ZHOU

Investigation of High-sensitivity Superconducting HEB Mixers for Antarctic Astronomy

Thèse dirigée par Y. Delorme, S.C. Shi and A. Maestrini

Soutenue le 30 Septembre 2015 devant le jury composé de:

M. Zhen Wang	Président du jury
M. Philippe Feautrier	Rapporteur
M. Jian Chen	Rapporteur
M. Sheng-Cai Shi	co-Directeur de thèse
Mme. Yan Delorme	co-Directeur de thèse
M. Alain Maestrini	co-Directeur de these
M. François Pajot	Examineur
M. Qi-Jun Yao	Examineur



Acknowledgments

Particular appreciation goes to Dr. Yan Delorme and Prof. Sheng-Cai Shi, for not only the countless hours of rough draft reading as it was in progress, inspiring suggestions, encouragement, and great patience with my seemingly endless revisions and questions but also for the immeasurable intellectual input and lively discussion through the duration of this work in their offices. I am so lucky and proud to be their dissertation supervisee. They have been wonderfully supportive and always a joy to be with.

I am also grateful cordially to Prof. Alain Maestrini, for his guidance and support during the past years. He is one of the most enthusiastic and friendly people I have ever met.

I, especially, would like to give my special thanks to my father and mother whose love and support guide me to the final destination. I also dedicate the dissertation to my wife Zirui Li, she is the one always being there for me.

My sincere thanks also go to my colleague W. Miao, who has stood beside me, answering my questions generously, sharing useful academic experience, and helping with my experiments.

I would also like to thank my colleagues, namely Michele Batrung, Alexandre Feret, Rolland Lefevre, Frederic Dauplay, Jean-Michel, Krieg, Maurice Gheudin, Martina Wiedner, Gregory Gay, and other people of LERMA at Observatoire de Paris who have always been willing to help support my thesis research in any way they could, and they did.

I am deeply grateful to the entire faculty of Millimeter and Submillimeter lab at Purple Mountain Observatory, namely Wen Zhang, Jing Li, Qi-Jun Yao, Zhen-Hui Lin, Qin-Gen Huang, Zheng Lou, Wen-Ying Duan, Sheng Li, Dong Liu, Jia-Qiang Zhong, Kun Zhang, Jie Hu, Shao-Liang Li, Min Yao, Jie Liu, Zheng Wang, Wen-Tao Wu, Wen-Lei Shan, Ying-Xi Zuo, Jun-Da Jin, Xuan Zhang, and Xin Huang, for their helpful discussions and assistance. I feel very fortunate to have the opportunity to work with them and I value the friendship.

Finally, I am also happy to acknowledge Eiffel Excellence Scholarship from French Ministry of Foreign Affairs and International Development for the funding.

Resume

China is now building an astronomical observatory including a THz telescope at Dome A on the Antarctic plateau. The development of superconducting HEB (Hot Electron Bolometer) mixers, the best choice for coherent detection at frequencies beyond 1 THz, becomes increasingly crucial. We present in this manuscript the investigation of high-sensitivity superconducting HEB mixers using quasi-optical technology in the THz region.

The main results of this study are as follows:

- 1) We developed a vector measurement system to measure the dielectric constant of high-resistivity silicon at 77 K and 295 K and at millimeter wavelengths. The measured permittivity is adopted to simulate the far-field beam pattern of our quasi-optical superconducting HEB mixers.
- 2) We studied the far-field beam pattern of a superconducting HEB mixer by using both near-field heterodyne and far-field direct detection measurement system. The measured results accord well with the simulation. We also investigated the effect of HEB bias voltages and bath temperature on the far-field beam-pattern.
- 3) We successfully developed a high-sensitivity superconducting HEB mixer at 1.4 THz. The uncorrected measured double-sideband noise temperature is 600 K, which is a state-of-the-art result at this frequency. We systematically characterized heterodyne performances such as RF noise, conversion gain and noise bandwidth. We also measured the frequency response and calibrated it with a new method. Furthermore, we investigated the performance of this superconducting HEB device integrated with different elliptical lenses.
- 4) Finally, we measured the noise performance and the frequency response of a HEB mixer coupled to a 0.1-1.5 THz spiral antenna, the frequency dependence of the noise temperature has also been characterized.

This study has provided a further understanding of superconducting HEB mixers and allowed the realization of a HEB mixer with state-of-the-art sensitivity at 1.4 THz. Hence the results of this study can find good use in the 5 m terahertz telescope (DATE5) at Dome A.

Key words: Terahertz (THz), superconducting HEB mixer, high-sensitivity, heterodyne detection, quasi-optical.

Resumé en Français

La Chine est en train de construire un observatoire astronomique comprenant un télescope dans le domaine THz au Dome A en Antarctique. Le développement de mélangeurs HEB (Bolomètre à Electron Chaud) à supraconducteur, le meilleur choix pour la détection cohérente aux fréquences au-delà de 1 THz, devient de plus en plus crucial. Nous présentons dans ce manuscrit une étude approfondie de mélangeurs HEB à supraconducteur à haute sensibilité en utilisant la technologie quasi-optique.

Les principaux résultats de cette étude sont les suivants:

- 1) Nous avons développé un système de mesure vectorielle pour mesurer la constante diélectrique du silicium à haute résistivité à 77 K et 295 K. La permittivité mesurée est utilisée pour simuler le diagramme de rayonnement en champ lointain du mélangeur HEB en configuration quasi-optique utilisant une lentille au Si.
- 2) Nous avons mesuré le diagramme de rayonnement en champ lointain d'un mélangeur HEB à supraconducteur à la fois par le système de mesure hétérodyne en champ proche et par le système de mesure de détection directe en champ lointain. Les résultats de mesure concordent bien avec la simulation. Nous avons également étudié l'effet de la tensions de polarisation et de la température de bain du HEB sur le diagramme de rayonnement en champ lointain.
- 3) Nous avons développé avec succès un mélangeur HEB à supraconducteur à haute sensibilité à 1,4 THz. La température du bruit mesurée non corrigée à double bande latérale est de 600 K, qui se situe à l'état de l'art pour cette fréquence. Nous avons caractérisé systématiquement les performances hétérodynes du mélangeur, comme le bruit RF, le gain de conversion et la bande passante de bruit. Nous avons également mesuré et calibré la réponse en fréquence du mélangeur par un nouveau procédé. En outre, nous avons étudié la performance de ce mélangeur HEB en l'intégrant avec différentes lentilles elliptiques.
- 4) Enfin, nous avons mesuré la performance en bruit et la réponse en fréquence d'un mélangeur HEB couplé à une antenne spirale fonctionnant entre 0,1 et 1,5 THz, la

dépendance en fréquence de la température de bruit a aussi été caractérisée.

Cette étude a fourni une meilleure compréhension des mélangeurs HEB à supraconducteurs et a permis la réalisation d'un mélangeur HEB dont la sensibilité à 1,4 THz atteint l'état de l'art. Ces résultats peuvent ainsi trouver un bon usage dans le télescope THz de 5 m (DATE5) au Dome A en Antarctique.

Content

Acknowledgments.....	2
Resume	3
Resumé en Français.....	5

Chapter 1

Introduction	11
1.1 Terahertz sciences.....	11
1.1.1 Terahertz astronomy.....	12
1.1.2 Other applications of THz technology.....	15
1.2 Terahertz detecting technology	17
1.2.1 Direct (incoherent) detection	17
1.2.2 Heterodyne (coherent) detection	18
1.3 Background and future of superconducting HEB mixers	21
1.4 Thesis overview	22

Chapter 2

Theory of Superconducting HEB Mixers.....	27
2.1 Basic principle of bolometer	27
2.1.1 Basics of operation	28
2.1.2 Superconducting Hot-Electron Bolometers.....	30
2.1.3 Phonon-cooled & diffusion-cooled HEB.....	32
2.2 Mixing characteristics of HEB mixers	34
2.2.1 Mixing theory in bolometers	35

2.2.2 Conversion efficiency	36
2.2.3 Noise in HEB mixer	40
2.2.4 Gain bandwidth and noise bandwidth	46
2.2.5 Small signal impedance	49
2.3 Hot spot model	51
2.3.1 Standard model	51
2.3.2 One dimensional hot spot model	52
2.3.3 Andreev reflection and critical current	57
2.4 Resume	59

Chapter 3

Design and Simulation of Integrated Lens Antenna of Quasi-optical HEB Mixers..... 63

3.1 Quasi-optical HEB mixers	63
3.1.1 Dielectric lens	64
3.1.2 Planar antenna	68
3.2 Far-field beam pattern simulation of integrated lens antenna	72
3.2.1 GO/PO hybrid calculation	72
3.2.2 MoM/PO calculation	74
3.2.3 Comparison of two simulation methods	75
3.3 Gaussian beam and Gaussian coupling efficiency	77
3.4 Conclusion	79

Chapter 4

Investigation of Far-field Beam Patterns of Quasi-optical HEB Mixers..... 82

4.1 Measurement of Si dielectric constant	82
4.1.1 Measurement setup	83
4.1.2 Calculation of permittivity	84

4.1.3 Si permittivity at 77 K and 295 K.....	85
4.2 Far-field Beam pattern simulation with measured Si permittivity	88
4.3 Beam pattern measurements of a HEB mixer at 600 GHz.....	92
4.3.1 Direct far-field beam pattern measurement	92
4.3.2 Vector near-field measurement.....	95
4.3.3 Comparison between near-field and far-field measurement	97
4.4 Effect of HEB bias voltage and bath temperature on far-field beam patterns.....	98
4.5 Conclusion	100

Chapter 5

Investigation of a 1.4-THz Quasi-optical HEB Mixer	103
5.1 Mixer design	103
5.2 Device fabrication.....	106
5.3 DC characteristic.....	108
5.4 Receiver noise temperature and IF bandwidth.....	109
5.4.1 Receiver noise temperature and analysis	109
5.4.2 IF noise bandwidth	120
5.5 Intrinsic frequency response	121
5.6 Far-field beam pattern.....	125
5.7 Effect of lens's extension length on the mixer's performance.....	127
5.8 Conclusion	132

Chapter 6

Investigation of a 0.1-1.5 THz broadband HEB Mixer	134
6.1 Mixer design	134
6.2 DC characteristic.....	136
6.3 Receiver noise temperature.....	138

6.4 Spectral Response	141
6.5 Conclusion	143

Chapter 7

Conclusions	145
--------------------------	------------

Publications	148
---------------------------	------------

Chapter 1

Introduction

1.1 Terahertz sciences

The terahertz (THz) radiation, covering the frequency range between 0.1 THz to 10 THz (wavelength correspondingly ranges from 3 mm to 0.03 mm), falls in between infrared radiation and microwave radiation in the electromagnetic spectrum (see in Figure 1.1).

The terahertz region occupies approximately half the total luminosity in universe after the cosmic microwave background (CMB) radiation, about equal to that in the ultraviolet/visible/near-IR band. In this frequency range lie a lot of vibration and absorption lines of molecules which makes it interesting for deep space radio astronomy and for spectroscopic analysis [1]. Besides applications in radio astronomy, the THz technology has also been widely applied to other fields, e.g., atmospheric and environmental science, medical and dental imaging, gene theory, communications and detecting the DNA sequence of virus and bacteria. Astrophysics, Spectroscopy, medicine and security applications are only a few areas in science and technology that show an increased interest in measurements in this frequency range.

However, there are two factors restricting the development of terahertz technology: one is the lack of high-sensitivity detecting technology and the other is water-vapor absorption in atmosphere. The former one concerns in particular the lack of terahertz source which seriously restricts the development of heterodyne detection. The later one is mainly caused by the interactions between THz wave and rotating molecular (mainly oxygen and water) and the scattering of atmospheric particle [2].

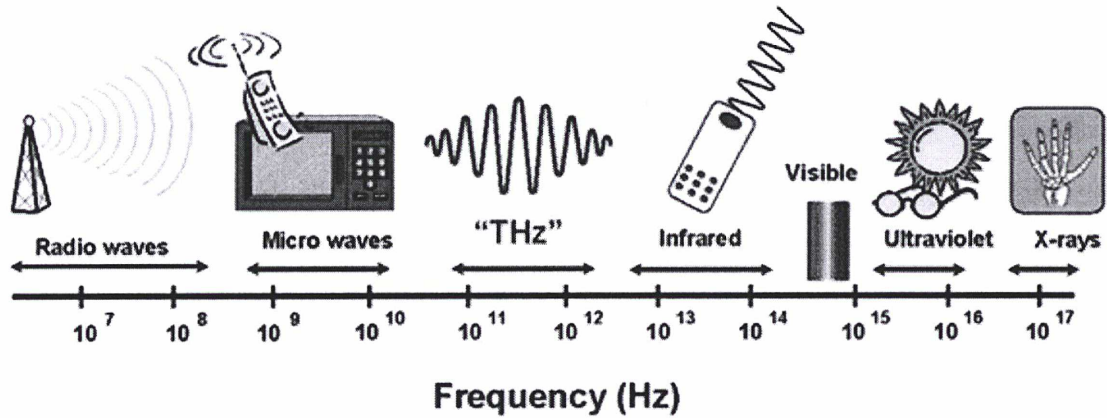


Figure 1.1: Terahertz region in the electromagnetic spectrum.

1.1.1 Terahertz astronomy

Terahertz astronomy is becoming more and more important in observational astronomy in the past two decades. Terahertz wave has higher interstellar penetration and space resolution than infrared and millimeter wave. In astrophysics, terahertz region is the most important band for cold and dark matter research in universe since approximately half the total energy of Milky Way and other spiral galaxies emits in this frequency. Therefore, terahertz astronomy is of great importance for studying star and galaxy formation, cosmology, etc.

The major research contents of terahertz astronomy include:

- 1) Cosmic Background Radiation: the research of cosmic background radiation (see in Figure 1.2) in terahertz frequency can provide abundant information for cosmology.
- 2) Cool interstellar dust and early universe: according to Wein's displacement law of radiation, the peak power of a 10 K blackbody radiation locates around 1 THz; the radiation of early distant objects also falls in THz band due to the Doppler shift effect.
- 3) Molecular and atomic spectral lines of fine construction: there are a great number of individual spectral lines in THz band, only a few thousand of which, a small part of the existing spectral lines, have been identified (see in Figure 1.3). These spectral

lines can help scientists study the physical and chemical characteristics of astronomical objects and provide information for understanding the formation of planets and stars.

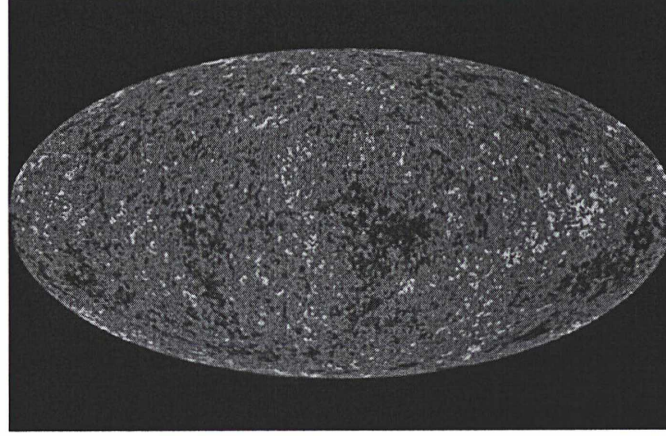


Figure 1.2: Picture of cosmic microwave background (CMB) radiation [3]

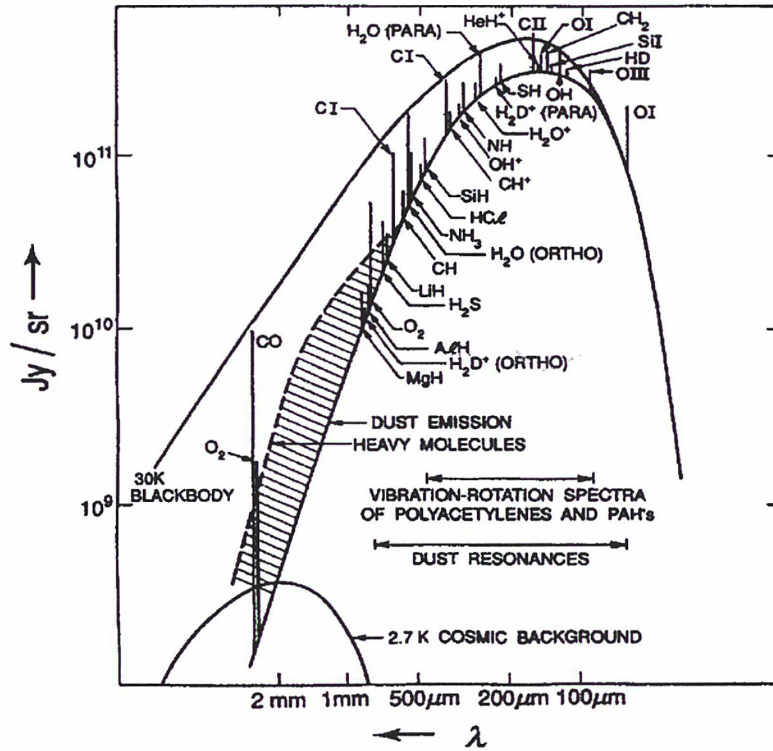


Figure 1.3: Schematic presentation of a 30-K interstellar molecular cloud. The spectrum includes dust continuum, molecular rotation- and atomic fine-structure line emissions in the THz regime (reprinted from [4]).

Since terahertz band plays an important role in modern astronomy, many countries have built Earth-based or space-based observatories and developed high-sensitivity detectors for them. However, THz signals are strongly absorbed by water vapor in atmosphere, they are

obscured from most Earth-based observations (except from a very few high-altitude observatories). This provides strong motivation for a number of existing or upcoming space astrophysics instruments. Stratospheric Observatory for Infrared Astronomy (SOFIA) [5] is a telescope set in a Boeing 747 aircraft. Space Infrared Telescope Facility (SIRTF) [6], covering the wavelength of 3.5-180 μm , is launched in 2003 by NASA. The most notably instrument is Herschel [7] satellite launched in 2009 by ESA (see in Figure 1.4 left), which is the largest sub-millimeter satellite and covers the frequency range of 0.48-1.91 THz by HIFI instrument. The detectors of HIFI are superconducting SIS mixer and superconducting HEB (Hot Electron Bolometer) mixer [8], which is the first time that superconducting THz detectors are applied to space astronomy observation.

Although space telescope can avoid water vapor absorption in atmosphere, its small aperture and short service life restrict the capacity of long time observation. Therefore, building THz observatories in high-altitude and dry area becomes another kind of economic and reliable choice. Many sub-millimeter (THz) and far-infrared (FIR) telescopes have been built in recent years, e.g. Atacama Large Millimeter /sub-millimeter Array (ALMA) [9] and CCAT [10] located on the Chajnantor plateau, at 5000 meters altitude in northern Chile (see in Figure 1.4 right); South Pole Telescope (SPT) [11], a 10 meter diameter telescope located on the Antarctic Plateau at an altitude of 2800 m.

China is now building an astronomical observatory including a THz telescope at Dome A on the Antarctic plateau. As the highest point on the plateau (4092 m above the sea level), Dome A is likely to be the coldest and driest location on the planet, opening up new windows for terahertz astronomy. Meanwhile, the climate in Dome A is very stable and the wind speed is low. These unique features of climate and geography make Dome A an excellent location for a THz astronomical observatory, as already demonstrated by early site testing result [12]. The development of high-sensitivity detector is crucial for the observatory at Dome A and consists of the main content of this thesis.

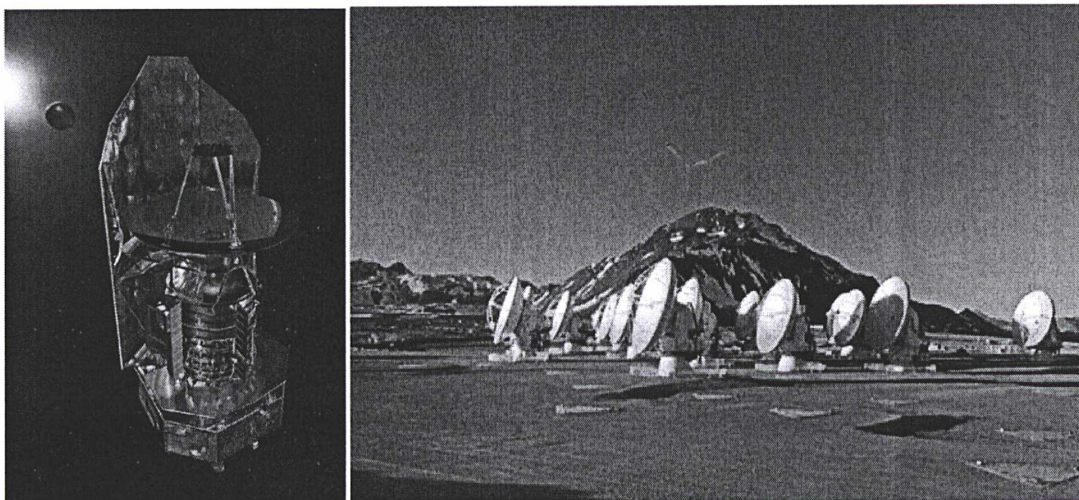


Figure 1.4: (left) Herschel space telescope (credit: ESA) and (right) Atacama Large Millimeter Array (ALMA-provide by NAOJ)

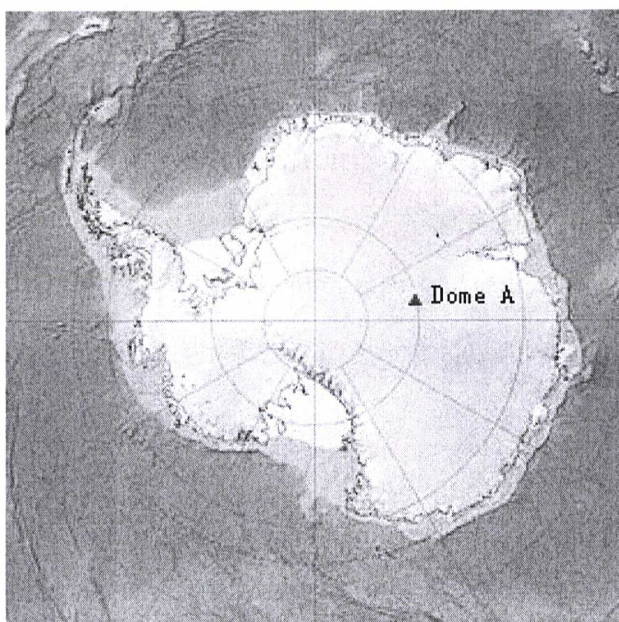


Figure 1.5: Dome A in Antarctic

1.1.2 Other applications of THz technology

In addition to astronomy, terahertz technology is rich in application in many other fields [13]. The unique properties of terahertz wave can have a great effect on atmospheric observation, communication, medical imaging, nondestructive testing, security etc. The main applications are as follow:

1) atmospheric observation:

The earth warming and the greenhouse effect are the biggest climate issues for human now. Observing the change of atmospheric ozone layer is a major means to monitor the greenhouse effect. OH group and HCl molecule play an important role in the deterioration of the ozone layer. Both of them have spectrum lines in THz band, this makes THz band crucial for monitoring the greenhouse effect. The atmospheric research in THz band can help scientists establish an accurate model of atmosphere and predict the destruction of atmospheric ozone layer and global warming trend.

2) Terahertz imaging:

Because the rotation and vibration energy level of many important biological macromolecules such as DNA, RNA and protein fall in THz band, scientists can use THz wave to analyze or accurately adjust the structure and characteristic of biological macromolecules. What's more, THz radiation can also pass through many materials used for packaging and clothing which, in recent years, attracted the interest of security agencies all around the world. By using sensitive THz detectors, it is possible to measure the THz emission from a human body. Concealed objects will (in contrast to the clothing which is transparent) show a different THz emission than the rest of the body and thus can be detected even if they are beneath clothes. It is also interesting for non-destructive material testing where transmission measurements of THz radiation can reveal internal inclusions inside materials.

3) Terahertz communication:

Terahertz communication includes the advantages of microwave communication and optical communication. It can provide a data rate as high as 10 Gb/s in wireless communication, the effective data transmission per second is more than 1T bit which is hundreds or even thousands of times faster than current ultra broadband technology. At the same time, terahertz communication has better secrecy and anti-jamming ability since it has very high directivity and strong penetration in cloud. Comparing to optical communication, terahertz wave has wider beam-pattern and lower quantum noise, so its antenna system can achieve

miniaturization and planarization.

Another important application of terahertz wave in communication technology is the remote sensing and communication of re-entry air vehicle such as missiles, satellites and spacecraft since terahertz wave won't be affected by the signal interruption caused by air ionization.

1.2 Terahertz detecting technology

According to the difference of working mechanism, there are two kinds of terahertz detecting technology: direct (incoherent) detection and heterodyne (coherent) detection. In this section, characterization techniques for both kinds of detectors are briefly discussed.

1.2.1 Direct (incoherent) detection

Direct detectors are not able to preserve the phase information of the incoming signal, they only detect amplitude information and generate a DC voltage or current signal proportional to the amount of the incoming signal power. The detector's sensitivity is characterized by NEP ($\text{W}/\sqrt{\text{Hz}}$), which is defined as the absorbed radiation power that produces a signal to noise ratio of unity at the output of the detector in the bandwidth of one hertz. Since direct detectors don't measure the phase information, its sensitivity isn't restricted by the Heisenberg uncertainty principle and has no upper limit. The main noise sources of a direct detector system are thermal fluctuation noise [14], noise in follow up amplifiers and $1/f$ noise. Figure 1.6 schematically illustrates the process of a typical direct detector system. The bandwidth of the system is determined by the RF filter and detector itself.

The most popular direct detector in THz band is transition edge bolometer (TES) [15]. Operation of this device is based on the sharp change of resistance of a superconductor at its transition temperature. Such a bolometer can be put in the center of its transition region by

applying a suitable bias current. Thus, even a small amount of absorbed radiation can increase the temperature of the bolometer such that it gives rise to a strong increase of resistance. Read out electronics can react to this increase and decrease the bias current accordingly to keep the bolometer at its transition edge point.

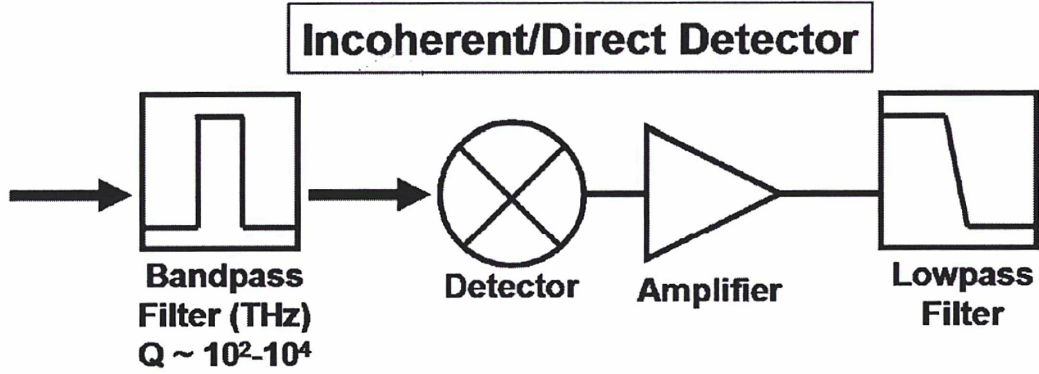


Figure 1.6: Schematic layout of a direct detector system [16].

1.2.2 Heterodyne (coherent) detection

Unlike direct detectors, heterodyne detectors can measure both amplitude and phase information by mixing the incoming local oscillator (LO) signal and RF signal. Heterodyne detectors are mainly used in high-resolution molecular and atomic spectrum observations, and high space resolution interferometers. The detector's sensitivity is characterized by equivalent noise temperature.

Figure 1.7 schematically illustrates the process of a typical heterodyne receiver. A weak signal of interest at frequency ω_s and a strong local oscillator signal ω_{LO} are coupled to the mixer by a beam splitter. Then an amplitude modulation is generated since the mixer has a strong nonlinear current-voltage characteristic. At the output of the mixer, the generated modulations will contain many components at the frequencies $m\omega_{LO} \pm n\omega_s$ for all integers m and n . In most practical cases, we are only interested in the component at the frequency $\omega_{IF} = |\omega_{LO} - \omega_s|$, which is called intermediate frequency. The intermediate frequency is amplified by a low noise amplifier and then be analyzed by a spectrum analyzer. A low pass

filter is commonly placed between the IF amplifier and the spectrum analyzer to make sure that only the IF part of the signal is coupled out and that the other frequencies are rejected.

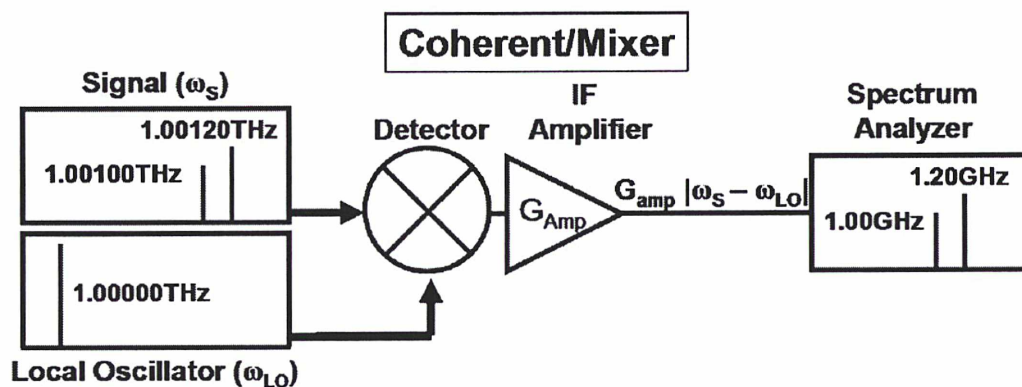


Figure 1.7: Schematic layout of a heterodyne detector system, the two signals are superimposed on a mixer. At the IF output port, the signal is amplified and filtered first and then measured by a spectrum analyzer [16].

The equivalent noise temperature of total receiver system can be expressed as:

$$T_{rec} = T_{RF} + \frac{T_m}{G_{RF}} + \frac{T_{IF}}{G_m G_{RF}} \quad (1.1)$$

where T_{rec} is the equivalent receiver noise temperature, T_{RF} is the noise temperature of the RF optics, T_m is the noise temperature of mixer itself whose upper limit is determined by quantum limit ($\hbar\omega / 2kB$), T_{IF} is the input noise temperature of the IF amplifier, G_{RF} is the gain of RF optics, G_m is the conversion gain of the mixer. It is obvious that the noise temperature and conversion gain of mixer is particularly important in a heterodyne receiver system. Here we briefly present three heterodyne detectors in THz frequency: Schottky-barrier diodes, superconductor-insulator-superconductor (SIS) junctions and hot electron bolometers (HEB).

a) Schottky-barrier diodes:

Schottky-barrier diodes are the most commonly used heterodyne detectors before superconducting detectors appeared. The most significant advantage of Schottky-barrier diodes is that they can work over a wide temperature range with

good sensitivity and do not require cooling to cryogenic temperatures. They can therefore be utilized where cryogenic cooling is not possible or unfavorable. They can also work over a wide frequency range (up to several THz) with good stability. The major disadvantage of Schottky-barrier diodes is that the receiver noise temperature increases rapidly with frequency, especially beyond 1 THz. Another disadvantage is that Schottky-barrier diodes require a relatively high level of LO power (typically a few milliwatt) [17], which is difficult to achieve in most THz astronomy observations.

b) Superconductor-insulator-superconductor junctions:

Superconducting SIS mixers consist of two superconductors separated by a very thin (only several atoms thick) layer of insulator, typically an oxide. The basis of mixing mechanism in SIS junction is the photon assisted tunneling of quasiparticles. Superconducting SIS mixer is the most sensitive detector at frequencies below 1 THz, the noise temperature is only 3~5 times of quantum limit at frequencies below 0.7 THz [18]. Meanwhile, Superconducting SIS mixer has wide IF bandwidth (more than dozens of GHz) and high conversion gain (about 0 dB), the requirement of LO power is small too. However, the application of SIS mixers is limited by its gap frequency that is determined by the material of superconductor (~ 0.7 THz for Niobium). The mixing performance will be degraded when the working frequency is beyond the gap frequency and is expected to degrade sharply at twice this frequency.

c) Superconducting Hot-Electron Bolometers (HEB)

Superconducting HEB mixers are currently the most sensitive detectors at frequencies beyond 1 THz. It normally consists of a very thin strip of superconductor placed between two bulky electrodes made of normal metal. The RF signal is coupled to the mixer via a planar antenna or waveguide. A DC bias voltage or current is also applied to the HEB device to keep it in resistance states, thus the device is heated close to its critical temperature T_c and has the sharpest rise of the resistance for mixing.

In contrast to superconducting SIS mixers, superconducting HEB mixers don't

suffer from a cut-off frequency set by the superconductor's energy gap (gap frequency). It has the lowest noise temperature at frequencies beyond 1 THz (see in Figure 1.8), nearly 10 times of quantum limit. Moreover, the LO power requirement for HEB mixers is very low. A minimal LO power requirement of 30 nW has been experimentally demonstrated [20]. Although the IF instantaneous bandwidth of superconducting HEB mixers has been found to be on the order of several GHz, it is enough for many astronomical applications. Overall, the superconducting HEB mixer is the most sensitive receiver for coherent detection at frequencies beyond 1 THz.

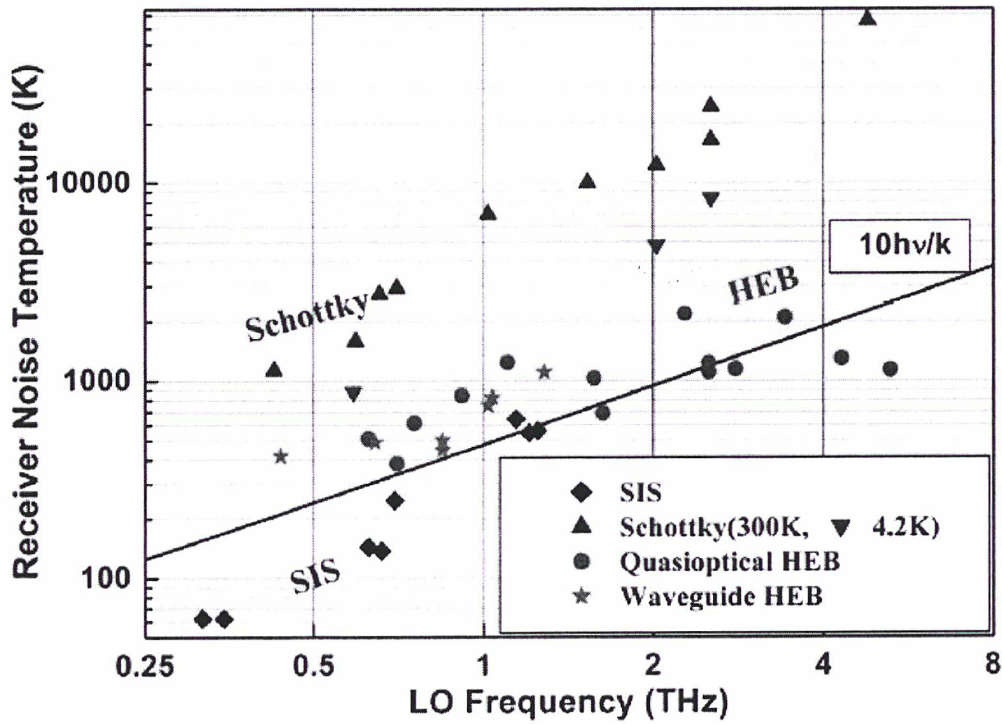


Figure 1.8: Receiver noise temperature as a function of frequency for three types of devices widely used in THz frequency range [21].

1.3 Background and future of superconducting HEB mixers

Bolometer is a device for measuring the power of incident electromagnetic radiation via the heating of a material with a temperature-dependent electrical resistance. In 1959, Boyle

put a bolometer based on carbon into practice for the first time, opening the door of applications of bolometer in many fields. More recently, a lot of attention has been attracted by superconducting hot electron bolometers [22, 23], which consist of a very thin superconducting film. In recent years, the superconducting HEB mixer has achieved a working frequency of 5.25 THz [24], and been selected for many ground based [25, 26] and space telescopes [27].

Despite the undeniable advantages of the HEB mixers compared with other receivers operated at frequencies higher than 1 THz, further work is carried out to optimize the basic characteristics of mixer such as the noise temperature and conversion band. At present, the conversion band of practical HEB receivers does not exceed 4 GHz since the electron response time is limited to 50 ps [28]. The lowest noise temperature of superconducting HEB mixer is only 10 times of quantum limit and can be further optimized.

Higher frequency and larger scale (multi-pixel) are also the research direction of HEB mixers. Progress towards much higher working frequency of superconductor HEB mixers is possible by decreasing the contact loss of the mixers with integrated antenna or by a direct-absorption design [29]. Large arrays of heterodyne detectors at submillimeter wavelengths are important for higher sensitivity, greater mapping speed, large scale mapping ability, and video rate imaging capability. Passive and/or active heterodyne large focal plane imaging arrays would have profound impact on medical diagnostics, explosive detections, and astrophysical imaging applications [30].

1.4 Thesis overview

In this thesis, we mainly focus on the development of high-sensitivity superconducting HEB mixers for astronomical observation in THz band. China is now building an astronomical observatory including a THz telescope at Dome A on the Antarctic plateau. Therefore the development of superconducting HEB mixers, the most sensitive for coherent detection at frequencies beyond 1 THz, becomes increasingly crucial. The main works of this

study include: 1) dielectric constant measurements of commonly used materials in THz band; 2) measurements and simulations of far field beam patterns of a quasi-optical superconducting HEB mixer; 3) development and characterization of a high-sensitivity superconducting HEB mixer at 1.4 THz; 4) design and characterization of a 0.1-1.5 THz spiral antenna coupled superconducting HEB mixer. The content of each chapter is as follows:

Chapter 1 gives an introduction about the characteristics, scientific significance and application prospect of THz band and THz detecting technology. Then the background and development tendency of superconducting HEB mixers and the motivation of this thesis are discussed.

Chapter 2 describes the operation principle and main characteristics of superconducting hot electron bolometer mixers.

In chapter 3 we first describe the structure of quasi-optical HEB mixer using a dielectric lens integrated with a planar antenna. Then we explain two simulation methods of far-field beam pattern of the quasi-optical configuration and compare their advantages.

Chapter 4 presents the measurements performed with a vector measurement system for material permittivity and analyzes the influence of different dielectric constants on the far-field beam pattern of our quasi-optical structure using the dielectric lens. Two measurement systems using either near-field heterodyne and far-field direct detection are developed to measure the far-field beam pattern of a superconducting HEB mixer. The measurement results are presented and analyzed.

Chapter 5 details the design, the fabrication and the characterizations of a 1.4 THz twin slot antenna coupled superconducting HEB mixer. The heterodyne performances, RF and DC characteristics as well as the methods of characterization of this mixer are presented. Furthermore, the influence of lens' parameters on the performance of this mixer is discussed.

In chapter 6, we report on the DC characteristic, noise temperature and IF noise bandwidth of a 0.1-1.5 THz spiral antenna coupled superconducting HEB mixer, and compare the spectral responses measured in both direct detection mode and heterodyne mode.

Chapter 7: we conclude the thesis with a summary about what is achieved in this work and a short outlook.

This work is carried out at LERMA of Observatoire de Paris in France and at Millimeter

and Sub-Millimeter Lab of Purple Mountain Observatory in China. This work is supported by the Eiffel Excellence Scholarship and the China-France Joint Doctoral Promotion Programme.

Bibliography

1. D. Leisawitz *et al.*, “Scientific motivation and technology requirements for the SPIRIT and SPECS far-infrared/submillimeter space interferometers,” in *Proc. SPIE*, vol. 4013, Munich, Germany, Mar. 29–31, 2000, pp. 36–46.
2. F.C.De Lucia, “Science and Technology in the submillimeter region,” *Optics & Photonic News*, 2003, pp. 44-50.
3. <http://map.gsfc.nasa.gov/media/121238/index.html>
4. T. G. Phillips and J. Keene, “Submillimeter astronomy,” *Proc. IEEE*, vol. 80, pp. 1662–1678, Nov. 1992.
5. <http://www.sofia.usra.edu/>
6. <http://www.spitzer.caltech.edu/index.shtml>
7. Herschel project, <http://sci.esa.int/science-e/www/area/index.cfm?fareaid=16>
8. E.M. Gershenzon, G.N. Gol’tsman, I.G. Gogidze, Y.P. Gusev, A.I. Elant’ev, B.S. Karasik, and A.D. Semenov, “Millimeter and submillimeter range mixer based on electronic heating of superconducting films in the resistive state,” *Sov. Phys.-Supercond.*, 1990 (3), pp. 1582–1597.
9. <http://www.alma.nrao.edu/>
10. <http://pole.uchicago.edu/>
11. <http://www.submm.org/>
12. X. Gong *et al.*, “Dome A site testing and future plans,” *EAS Publications Series*, Vol. 40, pp. 65-72, 2010.
13. P. Siegel, “Terahertz technology,” *IEEE Trans. Microwave Theory Tech.*, 2002 (50), pp. 210-228.
14. P. Richards, “Bolometers for infrared and millimeter waves,” *J. Appl. Phys.*, 1994 (76), pp.

1-24.

15. C.L. Hunt, J.J. Bock, P.K. Day, A. Goldin, A.E. Lange, H.G. LeDuc, A. Vayonakis and J. Zmuidzinas, "Transition-edge superconducting antenna-coupled bolometer," *Proceedings of the SPIE*, Vol. 4855, pp. 318-321, 2003.
16. Matthew Owen Reese, "Superconducting Hot Electron Bolometers for Terahertz Sensing," *PhD thesis*, Yale University.
17. B.N. Ellison, B.J. Maddison, C.M. Mann, D.N. Matheson, M.L. Oldfield, S. Marazita, T.W. Crowe, P. Maaskant, and W.M. Kelly, "First results for a 2.5 THz Schottky diode waveguide mixer," in *Proc. of 7th International Symposium on Space Terahertz Technology*, Charlottesville, USA, pp. 494-502, 1996.
18. Wenlei Shan, Shengcai Shi, Yutaro Sekimoto and Takashi Noguchi, "Effect of Magnetic Field on Performance of SIS Mixers Measured at 385-500GHz," *IEEE Microwave and Wireless Components Letters*, 2007 (17), pp. 268-270.
19. A. Karpov, D. Miller, F. Rice, J.A. Stern, B. Bumble, H.G. LeDuc, J. Zmuidzinas, "Low noise 1THz–1.4THz mixers using Nb/Al-AlN/NbTiN SIS junctions," *IEEE Trans. Appl. Supercond.*, 2007 (17), pp. 343-346.
20. M. Hajenius, J.J.A. Baselmans, A. Baryshev, J.R. Gao, T.M. Klapwijk, J.W. Kooi, W. Jellema, and Z.Q. Yang, "Full characterization and analysis of a THz heterodyne receiver based on a NbN hot electron bolometer," *Journal of Applied Physics*, Vol. 100, No. 7, pp. 074507, 2006.
21. Wei Miao, "Investigation of Hot Electron Bolometer Mixer for Submillimeter Multi-pixel Receiver Application," *PhD thesis*, I'UNIVERSITE PARIS VI, 2010.
22. Prober D, "Superconducting terahertz mixer using a transition-edge microbolometer." *Appl Phys Lett*, 1993, 62: 2119 – 2121.
23. W. R. McGrath, "Hot-electron bolometer mixers for submillimeter wavelengths: An overview of recent developments," in *6th Int. Space Terahertz Technol. Symp.*, Pasadena, CA, Mar. 21–23, 1995, pp. 216–228.
24. W. Zhang, P. Khosropanah, J. R. Gao, T. Bansal, T. M. Klapwijk, W. Miao, and S. C. Shi, "Noise temperature and beam pattern of an NbN hot electron bolometer mixer at 5.25 THz " *J. Appl. Phys.* 108, 093102 (2010).

25. J. Kawamura, T.R. Hunter, C.E. Tong, R. Blundell, D.C. Papa, F. Patt, W. Peters, T.L. Wilson, C. Henkel, G.N. Gol'tsman, and E.M. Gershenzon, "Ground-based terahertz CO spectroscopy towards Orion," *Astronomy and Astrophysics*, Vol. 394, pp. 271-274, 2002.
26. E. Gerecht, S. Yngvesson, J. Nicholson, Y. Zhuang, F. Rodriguez, X. Zhao, D.Z. Gu, R. Zannoni, M.J. Coulombe, J.C. Dickinson, T.M. Goyette, J. Waldman, C.E. Groppi, A.S. Hedden, D. Golish, C.K. Walker, A.A. Antony, C. Martin, and A. Lane, "TREND: a low noise terahertz receiver user instrument for AST/RO at the south pole," *Proceedings of the SPIE*, Vol. 4855, pp. 574-582, 2003.
27. S. Cherednichenko, M. Kroug, H. Merkel, P. Khosropanah, A. Adam, E. Kollberg, D. Loudkov, G. Gol'tsman, B. Voronov, H. Richter, and H.W. Hubbers, "1.6 THz heterodyne receiver for the far infrared space telescope," *Physica C: Superconductivity*, Vol. 372, pp. 427-431, 2002.
28. S. Cherednichenko, V. Drakinskiy, T. Berg, P. Khosropanah, and E.L. Kollberg, "Hot-electron bolometer terahertz mixers for the Herschel space observatory," *Rev. Sci. Instrum.* 79, 034501 (2008).
29. A. V. Smirnov, A.M. Baryshev, P. de Bernardis, V. F. Vdovin, G. N. Gol'tsman, N. S.Kardashev, L. S.Kuz'min, V.P. Koshelets, A.N. Vystavkin, Yu.V. Lobanov, S.A.Ryabchun, M. I. Finkel, and D. R. Khokhlov, "The current stage of development of the receiving complex of the millimetron space observatory," *Radiophysics and quantum electronics*, 54(8-9), 557-568, 2012.
30. C. Groppi, C. Walker, C. Kulesa, G. Narayanan, K. Jacobs, U. Graf, R. Schieder, and J. Kooi, "Heterodyne Array Development at the University of Arizona," *In Proc. 14th. Intl. Symp. Space THz Tech.*, Tucson, AZ, April 2003, pp. 189-203.

Chapter 2

Theory of Superconducting HEB Mixers

2.1 Basic principle of bolometer

Bolometer is a device for measuring the power of incident electromagnetic radiation via the heating of a material with a temperature-dependent electrical resistance. The first bolometer, consisted of two platinum strips covered with lampblack, was developed by Samuel Pierpont Langley in 1878 as a tool to measure the infrared spectrum of the sun [1]. Today, most bolometers use semiconductor or superconductor absorptive elements. These devices can be operated at cryogenic temperatures, enabling significantly greater sensitivity. Since bolometers have no limit to working frequency, they are widely used in remote sensing satellites and astronomical observations.

In this chapter, we first describe the basic operation principle of a bolometer. The most important figures of merit like sensitivity and response time of the bolometer are derived and explained. The special case of the superconducting hot-electron bolometer is introduced and explained. In the second part, we present the theory and mixing characterization of superconducting hot-electron bolometer in detail. In the last part of the chapter the theoretical models of superconducting HEB mixer are presented.

2.1.1 Basics of operation

A bolometer consists of an absorptive element, such as a thin layer of metal, connected to a thermal reservoir (a body of constant temperature) through a thermal link. Any radiation impinging on the absorptive element raises its temperature above that of the reservoir. The temperature change can be measured directly with an attached resistive thermometer, or the resistance of the absorptive element itself can be used as a thermometer. A schematic view of the basic components of a bolometer is shown in Figure 2.1.

When radiation power P from an incident signal is absorbed by the absorber, the produced heat is transferred to the thermal mass. Then the thermal mass will be heated up to a temperature T depending on the amount of power absorbed by its heat capacity C . The temperature difference between the non-irradiated state and the irradiated state is proportional to the power of the absorbed radiation. To relax back into its initial state the bolometer body is coupled to a thermal bath. The thermal coupling is described by the thermal conductance G , which governs the time that the heat can be removed from the thermal mass.

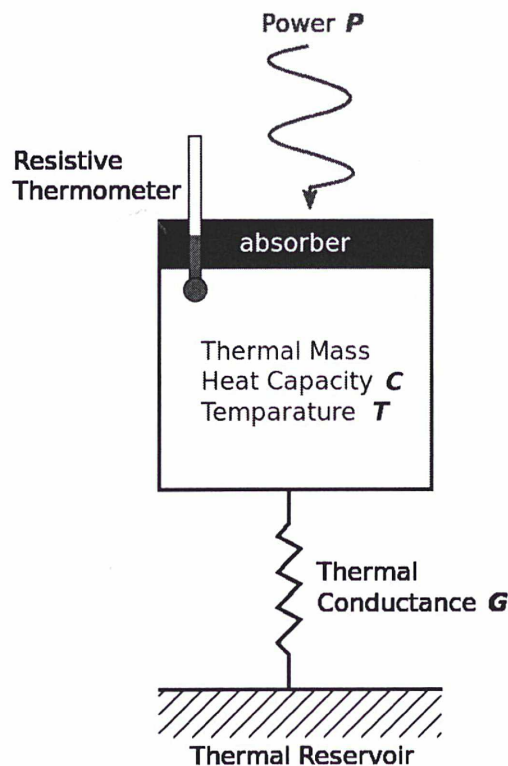


Figure 2.1: Conceptual schematic of a bolometer [2].

There are three key figure-of-merits of bolometers: response time, noise equivalent power (NEP) and voltage responsivity.

The time dependent behavior of a bolometer that absorbs all incoming radiation can be described according to [3] using the thermal balance equation of the system:

$$P_s = G\Delta T + C \frac{dT}{dt} \quad (2.1)$$

here P_s is the absorbed incoming radiation power, $\Delta T = T - T_b$, T is the temperature of bolometer after absorbing the incoming radiation, T_b is the temperature of the thermal reservoir.

The speed of this temperature change or its inverse, the response time τ in which the bolometer can relax to its equilibrium state is defined by the ratio between the conductance G and heat capacity C of the bolometer body as : $\tau = \frac{C}{G}$.

When a bolometer is irradiated by a radiation source with a modulated amplitude, the temperature change of bolometer will also be modulated. Assume the power of the incoming radiation consists of a constant part and a variation part, it can be written as $P_s = P_0 + \Delta P(\omega t)$. Using this equation and Eq. 2.1, the temperature response of the bolometer ΔT to the incoming radiation power ΔP can be calculated:

$$\frac{\Delta T}{\Delta P} = \frac{1}{G\sqrt{1 + \omega^2 \tau^2}} \quad (2.2)$$

where ω is the modulation frequency of the output power. Eq. 2.2 also describes the thermal sensitivity S_{th} of the bolometer to incoming radiation.

The signal-to-noise ratio (SNR) of a direct detector can be defined as:

$$SNR = \frac{P_s}{NEP} \sqrt{2T_{int}} \quad (2.3)$$

where T_{int} is the effective integration time, the factor 2 is chopping efficiency (50%).

The noise equivalent power (NEP) is defined as the signal power that gives a signal-to-noise ratio of one in a one hertz output bandwidth. Using this definition, Eq. 2.3 and $P_s = 2k_B T_s \Delta \nu$ (Rayleigh-Jeans approximation, factor 2 represents two polarizations), we can get the expression of NEP :

$$NEP = 2k_B T_S \Delta\nu \sqrt{2T_{\text{int}}} (W / \sqrt{H_Z}) \quad (2.4)$$

where $\Delta\nu$ is bandwidth and is proportional to NEP .

The voltage responsivity (electrical sensitivity) S_V of a resistive bolometer is defined as the ratio of the change of the detector voltage ΔV to the change of radiation power ΔP . Taking Eq. 2.2, the sensitivity can be written as:

$$S_V = \frac{\Delta V}{\Delta P} = \frac{I_{\text{bias}} \Delta R}{\Delta P} = I_{\text{bias}} \frac{\Delta R}{\Delta T} \frac{1}{G \sqrt{1 + \omega^2 \tau^2}} \quad (2.5)$$

The voltage responsivity S_V and noise equivalent power (NEP) can be related by equation

$$NEP = \frac{V_n}{S_V}, \text{ where } V_n \text{ is the measured noise voltage.}$$

Bolometer can work in both direct and heterodyne detection mode. When it operates as a direct detector, the voltage responsivity needs to be optimized to maximum. According to Eq. 2.5, thermal conductance G should be reduced. But the decrease of G will also increase the response time τ , and then decrease the voltage responsivity. Therefore, we normally reduce the area of detector to decrease its heat capacity C and keep response time τ as small as possible. When bolometer operates as a mixer, the thermal response time determines the IF instantaneous bandwidth of the mixer. In order to have shorter response time τ , the thermal conductance G should be increased.

2.1.2 Superconducting Hot-Electron Bolometers

The signal power of many interesting applications in the THz frequency range is very small which makes it difficult to be detected. So there is a need for very sensitive detectors. One kind of detector that can satisfy this need is the superconducting Hot-Electron Bolometer (HEB) [4].

Figure 2.2 illustrates a two dimensional cross-section of a typical superconducting Hot-Electron Bolometer. The HEB device is indeed made of a superconductor thin film

(micro-bridge) and a planar antenna integrated on a dielectric highly resistive substrate. The superconducting thin film is usually connected with two metal pads and is coupled to the input radiation via an on chip antenna or a mechanical waveguide.

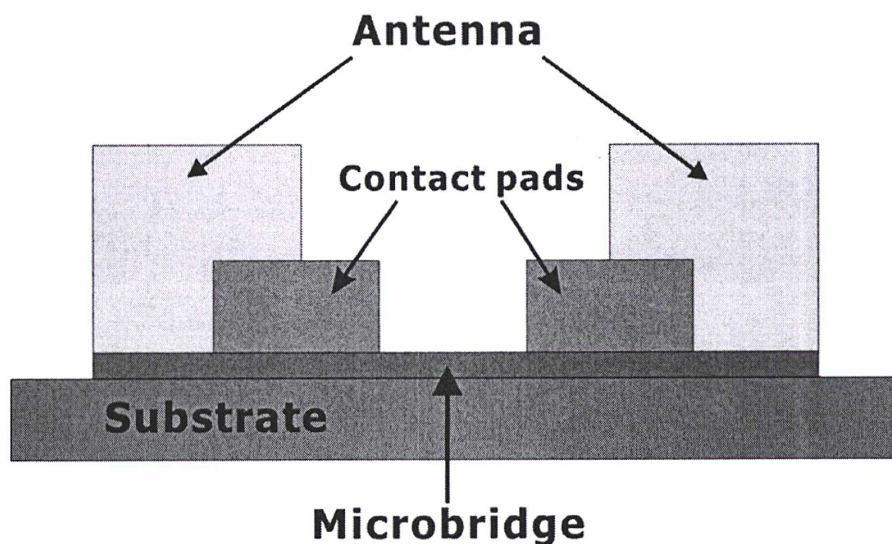


Figure 2.2: Schematic of a superconducting Hot-Electron Bolometer

Figure 2.3 illustrates a thermal transfer model in a superconducting thin film [5]. The film is assumed to consist of two separate systems, one is electron system and the other is phonon system. Each system has a temperature of T_{ph} and T_e . The substrate has a temperature of T_s . The thermal transfer between electron system and phonon system can be represented by the thermal resistance R_{e-ph} , and the thermal transfer between phonon system and substrate can be represented by the thermal resistance R_{ph-s} . For traditional bolometer (operating at room temperature), the thermal resistance R_{e-ph} between electrons and phonons is extremely small due to the large phonon density. This means the interaction time between electrons and phonons is very short, and results a very fast thermal transfer between electron system and phonon system. Therefore, the induced temperature difference between electrons and phonons can be negligible. However, it is completely different for bolometer based on superconducting material. When the bolometer is refrigerated to temperature lower than the critical temperature of superconductor, the phonon density will decrease greatly,

resulting in a much longer interaction time and a larger thermal resistance R_{e-ph} . When the bolometer absorbs the incoming power, the thermal energy can break the Cooper-pair and form quasi-particles first and then can excite these quasi-particles to create "hot electrons". In this case, the temperature of electrons is substantially higher than that of phonons, which is referred to as hot electron effect.

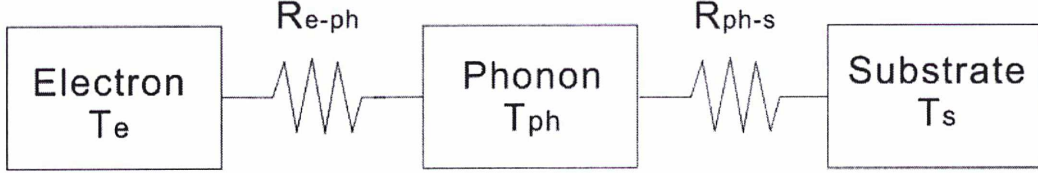


Figure 2.3: Schematic depiction of the thermal transfer in a hot-electron bolometer.

2.1.3 Phonon-cooled & diffusion-cooled HEB

According to the cooling mechanism, there are two types of superconducting hot-electron bolometer: phonon-cooled HEB [4] and diffusion-cooled HEB [7].

This thesis is focused on the phonon-cooled HEB, in which the hot electrons are cooled down by the interactions between electrons and phonons in the superconductor and then the energy is transferred to the substrate. The thermal time constant τ_{th} for a phonon-cooled HEB mixer is determined by the electron-phonon interaction time τ_{e-ph} and the escape time τ_{esc} of phonons into the substrate:

$$\tau_{th} = \tau_{e-ph} + \frac{C_e}{C_{ph}} \tau_{esc} \quad (2.6)$$

where C_e and C_{ph} is the specific heat of electron and phonon respectively. τ_{th} and τ_{e-ph} mainly depend on the materials and the structure of the microbridge. For a NbN microbridge, the electron-phonon interaction time τ_{e-ph} is commonly estimated to be less than 15 ps, corresponding to an instantaneous bandwidth of 10 GHz. Nevertheless, the relatively long

escape time of phonons τ_{esc} will limit the bandwidth to 4-5 GHz.

The diffusion-cooled HEB was proposed by Prober in 1993 for the first time. For this kind of HEB, the absorbed energy will diffuse into the contact pads rapidly before the phonon scattering event takes place. Therefore, the length of the microbridge L is much shorter than the electron-phonon scattering length λ_{th} , which is defined as:

$$\lambda_{th} = \sqrt{D\tau_{e-ph}} \quad (2.7)$$

here D is the electronic diffusion constant.

The thermal time constant for a diffusion-cooled HEB is determined by length of the microbridge L and the electronic diffusion constant D :

$$\tau_{diff} = \frac{L^2}{\pi^2 D} \quad (2.8)$$

In conclusion, the heat has two different paths (indicated by the red arrows in Figure 2.4) to leave the system. Both of these cooling mechanisms are present in every bolometer, but depending on the size and the material one of the two is dominant.

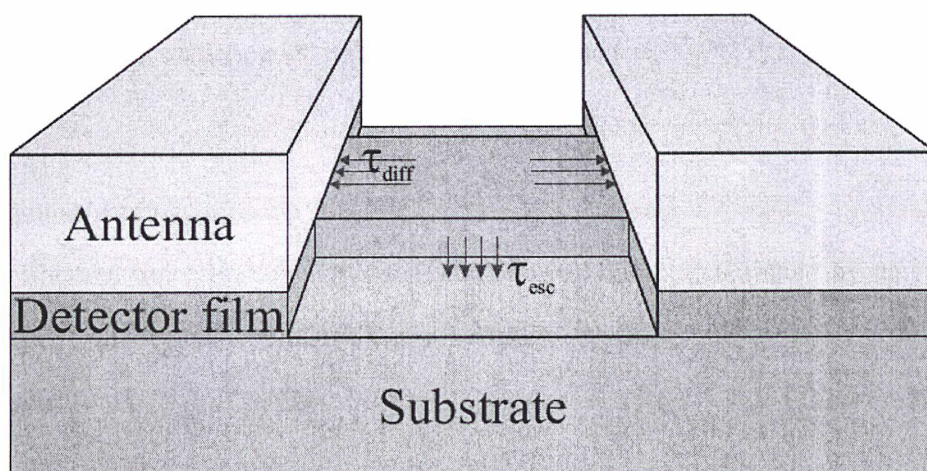
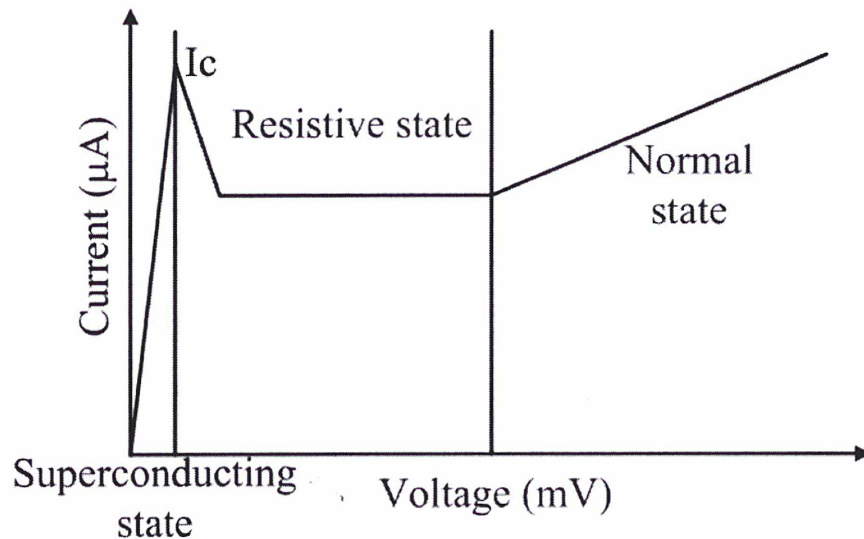


Figure 2.4: Sketch of the detector area of a typical Hot-Electron Bolometer and the thermal transfer direction of two kind of HEB [8].

2.2 Mixing characteristics of HEB mixers

The superconducting HEB mixer always operates at a cryogenic temperature (cooling to its superconducting state) to achieve high performance mixing. Usually, it is also electrically biased for adjusting its working state [9]. There are three states in a superconducting HEB device at a cryogenic temperature: superconducting state, resistive state and normal state. These states can be distinguished from both current-voltage (I - V) curve and resistance-temperature (R - T) curve, as shown in Figure 2.5. In the typical I - V curve, the HEB device is in superconducting state at the lower voltages, the current increases rapidly with the increasing voltage until it reaches a maximum value (critical current I_c). Then the current decreases due to the absorption of DC power by the microbridge, which results in a dynamic negative resistance and an instable region in the I - V curve. This region is corresponding to the resistive state of the HEB device and is where HEB device normally operates. When the bias voltage increases highly enough, the HEB device becomes normal conducting (normal state) and the superconducting properties disappear.



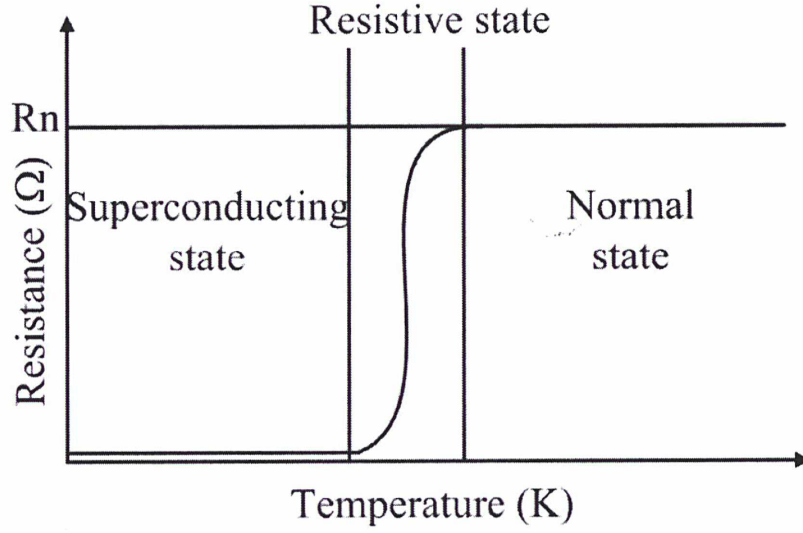


Figure 2.5: Typical current versus voltage (I - V) curve (upper) and resistance versus temperature (R - T) curve (lower) of a superconducting HEB mixer [6].

2.2.1 Mixing theory in bolometers

When a bolometer is fed by two signals with very close frequencies, it can operate in heterodyne mode. If we assume the local oscillator (LO) frequency is ω_{LO} , RF signal frequency is ω_{RF} , then the voltage across the bolometer is:

$$V_B(t) = V_{LO} \cos(\omega_{LO}t) + V_{RF} \cos(\omega_{RF}t) \quad (2.9)$$

where V_{LO} and V_{RF} are the voltage components of the LO and RF signal. If the resistance of bolometer is R_0 , the total instantaneous power dissipated by the bolometer can be expressed as [11]:

$$P(t) = \frac{V_B^2}{2R_0} \quad (2.10)$$

Substituting Eq. 2.9 into Eq. 2.10, the equation can be rewritten as:

$$P(t) = \frac{1}{R_0} \left[\frac{V_{LO}^2 + V_{RF}^2}{2} + \frac{V_{LO}^2}{2} \cos(2\omega_{LO}t) + \frac{V_{RF}^2}{2} \cos(2\omega_{RF}t) + 2V_{LO}V_{RF} \frac{\cos(\omega_{LO} + \omega_{RF})t + \cos(\omega_{LO} - \omega_{RF})t}{2} \right]$$

(2.11)

Here $P_{LO} = \frac{V_{LO}^2}{R_0}$ and $P_{RF} = \frac{V_{RF}^2}{R_0}$ are the average absorbed LO power and RF signal power respectively. In practice, RF signal power is usually much smaller than the LO power, i.e. $P_{RF} \ll P_{LO}$. Therefore, each P_{RF} component in Eq. 2.11 can be neglected. Since the response time τ is small, bolometer can't follow the temperature change at frequencies: $2\omega_{RF}$, $2\omega_{LO}$ and $\omega_{LO} + \omega_{RF}$. It can only response the change of electron temperature at the intermediate frequency $\omega_{IF} = |\omega_{LO} - \omega_{RF}|$. Therefore, Eq. 2.11 can be written as:

$$P(t) = P_{LO} + 2\sqrt{P_{LO}P_{RF}} \cos(\omega_{IF}t) \quad (2.12)$$

2.2.2 Conversion efficiency

The conversion efficiency is an important parameter for characterizing the mixing performance of superconducting HEB mixers. It is defined as the ratio of intermediate frequency power to input signal power [12]:

$$\eta = \frac{P_{IF}}{P_S} \quad (2.13)$$

where P_{IF} is the IF output power delivered to the load and P_S is the signal power absorbed at the mixer input.

Eq. 2.13 only illustrates the intrinsic conversion gain of a superconducting HEB device, while the total gain of a mixer system includes RF optical loss and IF gain too. The intrinsic conversion gain of a HEB device can be derived from the equivalent circuit in Figure 2.6 [13]. The main idea of the derivation is that the HEB device is assumed to be a resistance changing with the total power (including bias, RF signal and local oscillator power) and determined by the time constant of the device.

In this equivalent circuit, the DC component in Eq. 2.12 is blocked out by the capacitance C . Therefore, active radiation power can be rewritten as:

$$\Delta P_{RF} = 2\sqrt{P_{LO}P_S}e^{j\omega_{IF}t} \quad (2.14)$$

we also assume there is an initial bias current I_0 and voltage V_0 on the HEB device, then the DC resistance of the device is $R_0 = V_0 / I_0$.

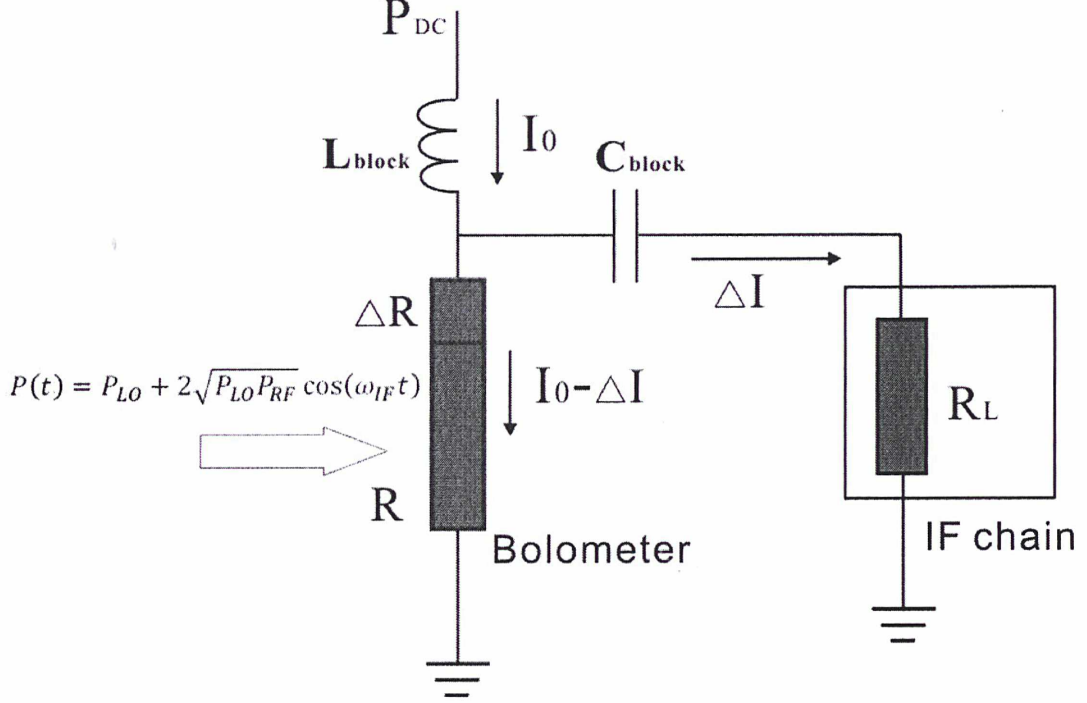


Figure 2.6: Equivalent circuit of a superconducting HEB mixer.

When the HEB device absorbs the LO and RF signal power, its resistance increases by ΔR . This small resistance results a current change ΔI across the HEB device. The current change also flows through the IF load resistance R_L and is modulated by IF frequency. Therefore, the DC power change can be written as:

$$\Delta P_{dc} = (V_0 + \Delta V)(I_0 - \Delta I) = I_0 \Delta V - V_0 \Delta I \quad (2.15)$$

Since the load resistance $R_L = \Delta V / \Delta I$, Eq. 2.15 can be rewritten as:

$$\Delta P_{dc} = I_0 R_L \Delta I - V_0 \Delta I \quad (2.16)$$

The change of the device resistance ΔR due to the change in incident radiation power ΔP_{RF} and in DC power ΔP_{dc} can be written in terms of the heating capacities as:

$$\Delta R = C_{RF} \Delta P_{RF} + C_{dc} \Delta P_{dc} \quad (2.17)$$

here $C_{RF} = \left. \frac{\Delta R}{\Delta P_{RF}} \right|_{\Delta P_{dc}=0}$ and $C_{dc} = \left. \frac{\Delta R}{\Delta P_{dc}} \right|_{\Delta P_{RF}=0}$.

What's more, the voltage change on HEB device should be the same with that on IF load resistance, then we have $\Delta V = R_L \Delta I = I_0 \Delta R - R_0 \Delta I$ (neglect the minimal term $\Delta I \Delta R$).

Substituting Eq. 2.17 into this formula, we can have:

$$R_L \Delta I = I_0 (C_{RF} \Delta P_{RF} + C_{dc} \Delta P_{dc}) - R_0 \Delta I \quad (2.18)$$

Substituting Eq. 2.18 into Eq. 2.16, the current change ΔI can be expressed as:

$$\Delta I = \frac{I_0 C_{RF} \Delta P_{RF}}{(R_0 + R_L) \left(1 + C_{dc} I_0^2 \frac{R_0 - R_L}{R_0 + R_L} \right)} \quad (2.19)$$

Combining Eq. 2.19, Eq. 2.13 and the formula $P_{IF} = R_L \Delta I^2 / 2$, the conversion gain can be expressed as:

$$\eta = \frac{P_{IF}}{P_S} = \frac{2 I_0^2 C_{RF}^2 R_L P_{LO}}{(R_0 + R_L)^2} \left(1 + C_{dc} I_0^2 \frac{R_0 - R_L}{R_0 + R_L} \right)^{-2} \quad (2.20)$$

Note that the heating capacities C_{RF} and C_{dc} have a frequency dependence determined by the electron relaxation time τ_θ , and can be given by:

$$C_{RF}(\omega) = \frac{C_{RF}(\omega=0)}{1 + j\omega\tau_\theta}$$

$$C_{dc}(\omega) = \frac{C_{dc}(\omega=0)}{1 + j\omega\tau_\theta} \quad (2.21)$$

Therefore, the final expression of conversion gain including frequency dependence can be given by:

$$\eta = \frac{2 I_0^2 C_{RF}^2 R_L P_{LO}}{(R_0 + R_L)^2} \left(1 + C_{dc} I_0^2 \frac{R_0 - R_L}{R_0 + R_L} \right)^{-2} \left(\frac{1}{1 + \omega_{IF}^2 \tau_{mix}^2} \right) \quad (2.22)$$

where τ_{mix} is the mixing time constant and can be written as

$$\tau_{mix} = \frac{\tau_\theta}{1 + C_{dc} I_0^2 \frac{R_0 - R_L}{R_0 + R_L}} \quad (2.23)$$

When a superconducting hot-electron bolometer operates as a heterodyne mixer, three factors can affect its sensitivity: bath temperature T , absorbed LO power P_{LO} and DC bias V_{HEB}^{dc} . To better understand the complex physical interactions that govern the HEB mixer, we depict in Figure 2.7 a graphical representation of the HEB device physics. DC bias is in the horizontal direction and applied LO bias in the vertical direction. At the lower left corner is the intrinsic device resistance $R(T)$ at temperature T . At the lower right is $R(T, I_{HEB}^{dc})$, the resistance as a function of temperature T and HEB's dc current I_{HEB}^{dc} . At the top is $I(V_{HEB}^{dc}, P_{LO})$, which is the current voltage characteristic as a function of bias voltage V_{HEB}^{dc} and local oscillator power P_{LO} . The dashed curve follows the HEB mixer conversion gain. It is easy to find from Figure 2.7 that the conversion gain of the mixer is strongly dependent on these three factors..

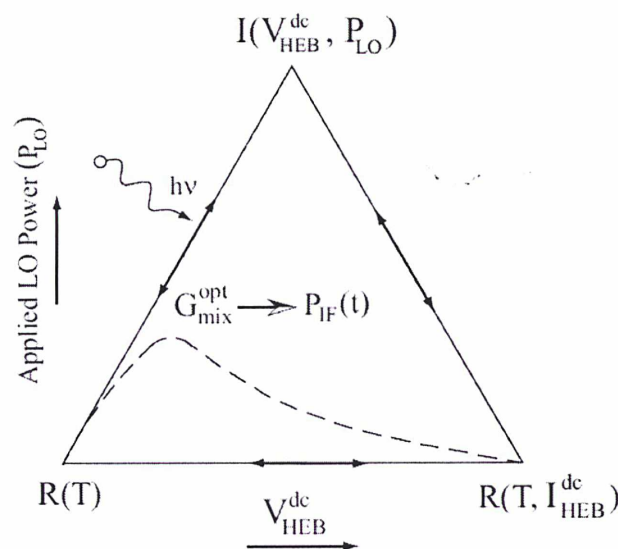


Figure 2.7: Diagram of various processes in superconducting HEB mixer, the dashed curve in the middle of the triangle indicates the condition for optimal mixer gain [10].

Figure 2.8 shows four I-V curves under various LO pump conditions and the optimal bias region of a superconducting HEB device. The optimal bias region normally locates where the negative resistance region disappears. The optimal bias voltage is normally set to about 0.5-1 mV.

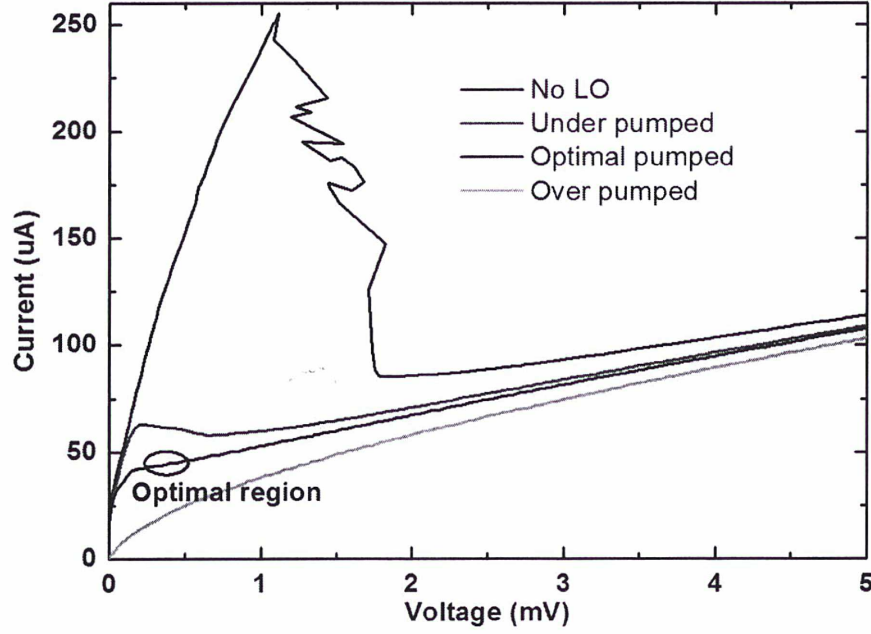


Figure 2.8: Four I-V curves as a function of LO power.

2.2.3 Noise in HEB mixer

Hot-electron bolometers are used for measurement of very weak energy signals. The ultimate limiting factor in signal measurement is the noise generated by the receiver system and the background noise of the incoming radiation. When the noise signal is larger than the incoming radiation, no measurements are possible. Thus for the measurement of small signals the reduction of the noise is of great importance.

According to the noise mechanism, there are several kinds of noise in a receiver system: Johnson-Nyquist noise, thermal fluctuation noise, quantum noise, shot noise and Flicker noise ($1/f$ noise).

Among these noises, the $1/f$ noise can be neglected at THz frequencies since it is inversely proportional to frequency and mainly impacts at low frequencies.

The shot noise comes from the random motion of electric charge. It is a type of electronic noise which can be modeled by a Poisson process. In electronics, shot noise originates from the discrete nature of electric charge. Shot noise is a static white noise which is independent with frequency and temperature. The power of shot noise can be expressed as:

$$(P_n)_{shot} = \frac{1}{4} \overline{i^2} R = \frac{1}{2} e I_{dc} B R \quad (2.24)$$

where e is the charge, I_{dc} is dc current, B is noise bandwidth, $\overline{i^2} = 2eI_{dc}B$ is the root-mean-square current of shot noise [15]. In a superconducting HEB device, the shot noise is mainly caused by the discontinuity of barriers between HEB device and two electrodes. The equivalent noise temperature of shot noise can be expressed as [16]:

$$T_{shot} = \frac{(P_n)_{shot}}{k_B B} = \frac{e I_{dc} R}{2 k_B} \quad (2.25)$$

In a superconducting HEB device, the barrier resistance R is only several ohms, so the shot noise can be neglected too.

Besides $1/f$ noise and shot noise, Johnson-Nyquist noise and thermal fluctuation noise are two major noise sources in a superconducting HEB mixer. In the optimum operation region, the latter one is usually dominant. At THz frequencies, the quantum fluctuation of the input signal, regarded as quantum noise, also becomes increasingly important as the frequency rises.

Johnson-Nyquist noise:

Johnson-Nyquist noise was first measured by John B. Johnson at Bell Labs in 1926. It is the electronic noise generated by the thermal agitation of the charge carriers (usually the electrons) inside an electrical conductor at equilibrium, which happens regardless of any applied voltage. The Johnson-Nyquist noise in an ideal resistor is approximately white, meaning that the power spectral density is nearly constant throughout the frequency spectrum. When limited to a finite bandwidth, Johnson-Nyquist noise has a nearly Gaussian amplitude distribution.

Johnson-Nyquist noise is distinct from shot noise. The equivalent voltage source of the noise of a resistance R with a temperature of T can be expressed as [17]:

$$\langle v_n^2 \rangle = 4k_B T B R \quad (2.26)$$

Where k_B is Boltzmann's constant, B is bandwidth.

Figure 2.9 shows the equivalent circuit of the HEB mixer for modeling Johnson noise

[12]. If HEB device has a temperature of T_e and a resistance of R_0 , the equivalent voltage source of the noise on HEB device can be given by:

$$\langle v_n^2 \rangle = 4k_B T_e B R_0 \quad (2.27)$$

Then the total dissipated power in the HEB mixer can be given by:

$$P_0 + \Delta P = (R_0 + \Delta R)(I_0 - \Delta I)^2 + v_n(I_0 - \Delta I) \quad (2.28)$$

The second item on the right side of Eq. 2.28 represents the power of thermal noise, which is shown in Figure 2.9 by voltage source of the noise v_n . Expanding Eq. 2.28 and ignoring the second order of small signal terms, we can get:

$$P_0 + \Delta P = R_0 I_0^2 - 2I_0 R_0 \Delta I + \Delta R I_0^2 + v_n I_0 \quad (2.29)$$

Separating the small signal and large signal parts yields:

$$\Delta P = \Delta R I_0^2 - 2I_0 R_0 \Delta I + v_n I_0 \quad (2.30)$$

Substituting $\Delta P = \frac{\Delta R}{C_{dc}}$ into Eq. 2.30 and solving for ΔR :

$$\Delta R = \frac{v_n I_0 C_{dc} - 2I_0 R_0 \Delta I C_{dc}}{1 - C_{dc} I_0^2} \quad (2.31)$$

The voltage across the HEB device for a small signal can be expressed as:

$$V_0 + \Delta V = (R_0 + \Delta R)(I_0 - \Delta I) + v_n \quad (2.32)$$

Solving for ΔV :

$$\Delta V = -\Delta I R_0 + I_0 \Delta R + v_n = \Delta I R_L \quad (2.33)$$

Substituting Eq. 2.33 into Eq. 2.31 for solving ΔI :

$$\Delta I = \frac{v_n}{(R_L + R_0)(1 - C_{dc} I_0^2 \frac{R_L - R_0}{R_L + R_0})} \quad (2.34)$$

With this expression, the output Johnson-Nyquist noise power can be simply expressed as:

$$P_{Jn}^{out} = R_L \langle \Delta I^2 \rangle = \frac{R_L \langle \Delta v_n^2 \rangle}{(R_0 + R_L)^2 (1 - C_{dc} I_0^2 \frac{R_L - R_0}{R_L + R_0})^2} \quad (2.35)$$

Substituting Eq. 2.27 into Eq. 2.35:

$$P_{J_n}^{out} = R_L \langle \Delta I^2 \rangle = \frac{R_L * 4k_B T_e B R_0}{(R_0 + R_L)^2 (1 - C_0 I_0^2 \frac{R_L - R_0}{R_L + R_0})^2} = k_B B T_{J_n}^{out} \quad (2.36)$$

where $T_{J_n}^{out}$ is the Johnson-Nyquist output noise temperature and can be expressed as:

$$T_{J_n}^{out} = \frac{4R_L R_0 T_e}{(R_0 + R_L)^2 (1 - C_0 I_0^2 \frac{R_L - R_0}{R_L + R_0})^2} \quad (2.37)$$

It is obvious that the Johnson-Nyquist output noise of superconducting HEB mixer is white noise and independent on the intermediate frequency. Nevertheless, the Johnson-Nyquist noise at the input of the HEB mixer is different. It is dependent on the IF frequency since the conversion efficiency decreases when the IF frequency increases. The double side band (DSB) input Johnson-Nyquist noise can be expressed as:

$$T_{J_n}^{in} = \frac{T_{J_n}^{out}}{2\eta} = \frac{R_0 T_e}{C_{RF}^2 I_0^2 P_{LO}} (1 + \omega_{IF}^2 \tau_{mix}^2) \quad (2.38)$$

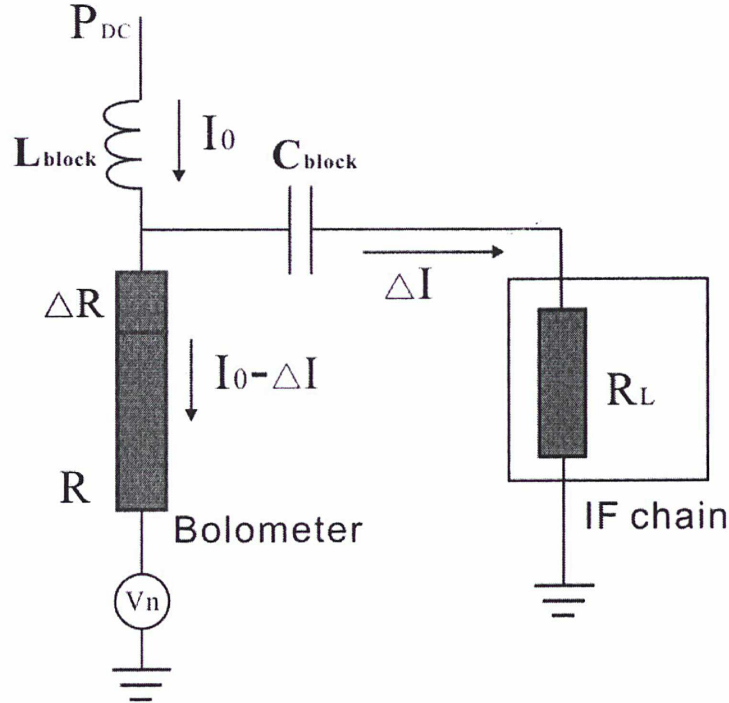


Figure 2.9: Equivalent circuit of the HEB mixer for modeling Johnson noise.

Thermal Fluctuation Noise:

The noise contributed by thermal fluctuations is a result of energy randomly flowing between the thermal reservoir and the bolometer. It is caused by the transfer of energy in

quantized units via quasiparticles, phonons or photons, and should clearly depend on the thermal conductance between the reservoir and bolometer. In a phonon-cooled superconducting HEB mixer, the device is cooled by the heat transfer between electron-phonon system and reservoir. During this process, the whole system generates random thermal fluctuation that behaves as the fluctuation of electron temperature.

In a general system with a temperature T , a heat capacity C and a thermal conductance G , the spectral density of temperature fluctuations is expressed as [18]:

$$\langle (\Delta T_{FL})^2 \rangle_f = \frac{k_B T^2}{G} \quad (2.39)$$

In the superconducting HEB mixer, the thermal fluctuation noise is limited in frequency range which is determined by the mixing time τ_θ . Therefore, Eq. 2.39 can be rewritten as:

$$\langle \Delta T_{FL}^2 \rangle_f = \int_0^\infty \langle (\Delta T_{FL})^2 \rangle_f \times \frac{1}{1 + (\omega \tau_\theta)^2} df = \frac{4k_B T_e^2}{G} \frac{1}{1 + \omega_{IF}^2 \tau_\theta^2} \quad (2.40)$$

When the LO power remains unchanged, the dissipated power in superconducting HEB mixer including the change of DC power and the thermal fluctuation noise power is:

$$\begin{aligned} \Delta P &= \Delta P_{DC} + P_{FL} = (V_0 + \Delta V)(I_0 - \Delta I) - V_0 I_0 + \frac{\Delta R}{C_0} \\ &= I_0 \Delta V - V_0 \Delta I + \frac{1}{C_0} \left(\frac{\partial R}{\partial T_e} \right) \times \Delta T_{FL} \\ &= I_0 \Delta I (R_L - R_0) + \frac{1}{C_0} \left(\frac{\partial R}{\partial T_e} \right) \times \Delta T_{FL} \end{aligned} \quad (2.41)$$

Substituting $\Delta P = \frac{\Delta R}{C_0}$ and $\Delta V = R_L \Delta I = I_0 \Delta R - R_0 \Delta I$ into Eq. 2.41, the small change of

current can be expressed as:

$$\Delta I = \frac{I_0 \frac{\partial R}{\partial T_e} \Delta T_{FL}}{(R_L + R_0) \left(1 - C_0 I_0^2 \frac{R_L - R_0}{R_L + R_0} \right)} \quad (2.42)$$

Therefore, the total output power at the load R_L due to the thermal fluctuation is:

$$\langle P_n \rangle_f^{out} = \frac{1}{2} \Delta I^2 R_L = \frac{R_L I_0^2 \left(\frac{\partial R}{\partial T_e} \right)^2 \langle (\Delta T_{FL})^2 \rangle_f}{(R_L + R_0)^2 (1 - C_0 I_0^2 \frac{R_L - R_0}{R_L + R_0})^2} \quad (2.43)$$

Substituting Eq. 2.39 into Eq. 2.43, the noise temperature due to thermal fluctuation at the output of the mixer can be given by:

$$T_{FL}^{out} = \frac{\langle P_n \rangle_f^{out}}{k_B} = \frac{R_L I_0^2 \left(\frac{\partial R}{\partial T_e} \right)^2 \frac{4T_e^2 \tau_\theta}{C_e}}{(R_L + R_0)^2 (1 - C_0 I_0^2 \frac{R_L - R_0}{R_L + R_0})^2} \quad (2.44)$$

Substituting $C_0 = \frac{\partial R}{\partial T_e} \frac{\partial T_e}{\partial P} = \frac{\partial R}{\partial T_e} \frac{1}{G} = \frac{\partial R}{\partial T_e} \frac{\tau_\theta}{C_e}$ into Eq. 2.44, T_{FL}^{out} can be rewritten as:

$$T_{FL}^{out} = \frac{4R_L T_e^2 \frac{\partial R}{\partial T_e} C_0 I_0^2}{(R_L + R_0)^2 (1 - C_0 I_0^2 \frac{R_L - R_0}{R_L + R_0})^2} \quad (2.45)$$

The double side band (DSB) noise temperature caused by thermal fluctuation at the input of the mixer can be obtained by dividing the output noise by the conversion gain (refer to Eq. 2.20):

$$T_{FL}^{in} = \frac{T_{FL}^{out}}{2\eta} = \frac{1}{C_{RF}^2 P_{LO}} \left(\frac{\partial R}{\partial T_e} \right)^2 \frac{T_e^2 \tau_\theta}{C_e} \quad (2.46)$$

Apparently, the thermal fluctuation noise does not depend on the intermediate frequency. In addition, the thermal fluctuation noise is proportional to the square of electron temperature, while the Johnson-Nyquist noise is only proportional to electron temperature. Therefore, the thermal fluctuation noise is dominant in HEB mixers [19], typically one order in magnitude higher than the Johnson-Nyquist noise, when HEB mixer is operating close to the critical temperature in resistive state.

Quantum noise

Quantum noise is the ultimate noise limit of a receiver system on simultaneous measurement of the amplitude and phase of the electromagnetic field. The essence of quantum noise is the wave-particle dualism. According to Heisenberg uncertainty principle,

the quantum noise can be expressed as [20]:

$$T_{rx} = \frac{h\nu}{k_B} \quad (2.47)$$

Where h is Planck constant, ν is frequency and k_B is Boltzmann's constant. The quantum noise is referred to the input of HEB mixer.

From Eq. 2.47 we can find that when the frequency is low, the quantum noise can be neglected. However, it becomes increasingly important as the frequency rises. Recent experimental results [21] indicate that quantum noise contributes to roughly 30% of the total measured receiver noise temperature at frequencies beyond 4 THz for a NbN HEB mixer.

2.2.4 Gain bandwidth and noise bandwidth

In a phonon-cooled HEB mixer, the IF gain bandwidth is mainly determined by the mixing time constant. It is defined as the frequency at which the conversion efficiency drops to half of its maximum value:

$$f_{gain} = \frac{1}{2\pi\tau_{mix}} \quad (2.48)$$

where τ_{mix} is the mixing time constant of HEB mixer and can be determined by the electron relaxation time τ_θ :

$$\tau_{mix} = \frac{\tau_\theta}{1 - C_0 I_0^2 \frac{R_L - R_0}{R_L + R_0}} \quad (2.49)$$

Normally, τ_θ is close to τ_{mix} , $\tau_{mix} = 1.1\tau_\theta$.

The electron relaxation time τ_θ in a phonon-cooled HEB mixer is related to five processes, as shown in Figure 2.10. The processes and their time constants are described below:

1. The electron-electron interaction time τ_{e-e} . When the radiation is absorbed by the HEB

device, the energy will be distributed quickly throughout the electron subsystem by inelastic electron-electron interactions with time constant τ_{e-e} . Since the electron-electron interaction time is very short, the whole electron system will achieve an equivalent electron temperature T_e quickly. In the superconducting thin film, τ_{e-e} can be obtained by [22]:

$$\tau_{e-e} \approx \frac{1}{10^8 R_{sq} T_e} \quad (2.50)$$

Here R_{sq} is the sheet resistance of the film (typically 500 ohm for NbN). When the electron temperature is 10 K, τ_{e-e} is about 2 ps.

2. The electron-phonon interaction time τ_{e-ph} . It has been shown in experiments that the electron-phonon interaction time is a function of the electron temperature T_e and for NbN it can be written as[23]:

$$\tau_{e-ph} = \frac{5}{10^{10} T_e^{1.6}} \quad (2.51)$$

For NbN film, when the electron temperature is 10 K, τ_{e-ph} is about 10 ps.

3. The phonon-electron interaction time τ_{ph-e} . It is the time constant that energy flows from the phonon subsystem to the electron subsystem, and is related to τ_{e-ph} by:

$$\frac{C_e}{\tau_{e-ph}} = \frac{C_{ph}}{\tau_{ph-e}} \quad (2.52)$$

Here C_e and C_{ph} are electron and phonon specific heat respectively. Since C_{ph} / C_e is proportional to electron temperature T_e [24], the phonon-electron interaction time τ_{ph-e} is longer than the electron-phonon interaction time τ_{e-ph} .

4. The phonon escape time τ_{esc} , this time constant represents the relaxation time of heat from phonon subsystem to the substrate. It relates to the film thickness d , acoustic transparency factor α , and the sound velocity v in the film [25]:

$$\tau_{esc} \approx \frac{4d}{\alpha v} \quad (2.53)$$

5. The phonon backscattering time τ_{s-ph} , the time constant of the reverse energy flow from the substrate back to the phonon subsystem. When the width of superconducting film is less than the mean free path of the phonons, τ_{s-ph} can be neglected.

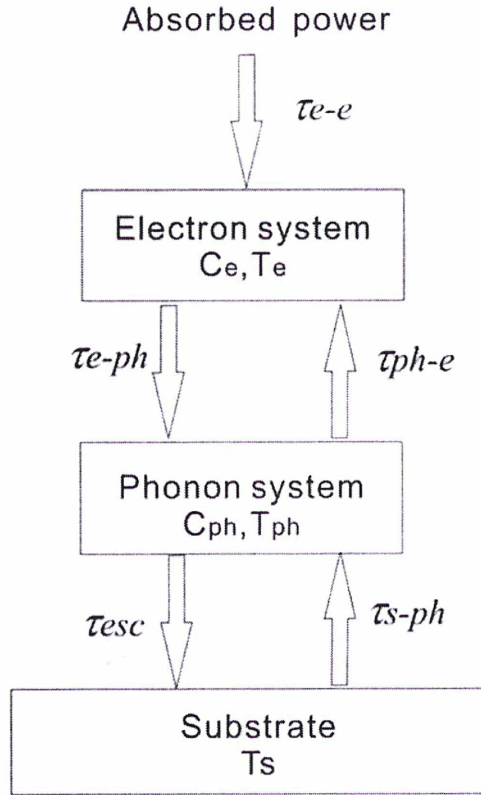


Figure 2.10: Heat relaxation processes in a superconducting phonon-cooled HEB mixer.

The electron relaxation time τ_θ is mainly determined by the electron-phonon interaction time τ_{e-ph} and phonon-escape time τ_{esc} . It can be written as:

$$\tau_\theta = \tau_{e-ph} + \frac{C_e}{C_{ph}} \tau_{esc} \quad (2.54)$$

According to Eq. 2.48, the IF gain bandwidth can be improved by reducing the electron relaxation time τ_θ . Adopting materials with high critical temperature to reduce the electron-phonon interaction time τ_{e-ph} , and reducing the thickness of superconducting film

are the common way to achieve shorter electron relaxation time. Note that when the thickness of superconducting film is thin enough, its critical temperature will decrease quickly. Therefore, an appropriate material and thickness is needed.

The noise bandwidth of a HEB mixer is defined as the IF frequency at which the mixer noise temperature increases by a factor of two. It can be obtained by [12]:

$$f_{noise} \approx f_{gain} \sqrt{\frac{T_{FL}^{out} + T_{Jn}^{out} + T_{IF}}{T_{Jn}^{out} + T_{IF}}} \quad (2.55)$$

Obviously, the noise bandwidth is always larger than the gain bandwidth.

2.2.5 Small signal impedance

The understanding of RF and IF impedance of the superconducting HEB mixer is helpful for achieving optimum matching at the input and output of the receiver. Here we will deduce the expression of small signal impedance. For simplicity, only DC power change is considered and LO power is kept unchanged.

As shown in Figure 2.11, if there is a small DC power change near HEB's bias point (V_0 , I_0), the corresponding resistance and power change ΔR and ΔP can be expressed as:

$$\Delta R = \frac{V_0 + \Delta V}{I_0 + \Delta I} - \frac{V_0}{I_0} \approx \frac{\Delta V I_0 - V_0 \Delta I}{I_0^2} \quad (2.56)$$

$$\Delta P = (V_0 + \Delta V)(I_0 + \Delta I) - V_0 I_0 \approx \Delta V I_0 + V_0 \Delta I \quad (2.57)$$

Then the DC capacitor becomes:

$$C_{DC} = \frac{\Delta R}{\Delta P} = \frac{1}{I_0^2} \frac{\Delta V I_0 - V_0 \Delta I}{\Delta V I_0 + V_0 \Delta I} = \frac{1}{I_0^2} \frac{(\frac{dV}{dI})_{DC} - R_0}{(\frac{dV}{dI})_{DC} + R_0} \quad (2.58)$$

Where $(\frac{dV}{dI})_{DC}$ is differential resistance and R_0 is the DC resistance of the HEB mixer.

Then the differential resistance can be expressed as:

$$Z(0) = R_d = \frac{dV}{dI} = R_0 \frac{1 + C_{DC} I_0^2}{1 - C_{DC} I_0^2} \quad (2.59)$$

According to Eq. 2.21, C_{DC} is frequency dependent, so the frequency dependent impedance $Z(\omega)$ can be expressed as:

$$Z(\omega) = Z(0) \frac{1 + \frac{j\omega\tau_\theta}{1 + C_{DC}I_0^2}}{1 + \frac{j\omega\tau_\theta}{1 - C_{DC}I_0^2}} = Z(0) \frac{1 + j\omega\tau_{imp} \frac{R_0}{Z(0)}}{1 + j\omega\tau_{imp}} \quad (2.60)$$

$$= R_0 \left(1 + \frac{2C_{DC}I_0^2}{1 - C_{DC}I_0^2} \frac{1}{1 + j\omega\tau_{imp}} \right)$$

Where $\tau_{imp} = \tau_\theta / (1 - C_{DC}I_0^2)$ is the time constant of the impedance.

Eq. 2.60 illustrates the frequency dependent impedance of a superconducting HEB mixer under a small signal, as shown in Figure 2.12. For frequency $f \ll 1/(2\pi\tau_{imp})$, the impedance can be given by $Z(0) = \frac{dV}{dI}$ and only has a real part. When the frequency increases to $1/(2\pi\tau_{imp}) \ll f \ll 2\Delta/h$, the frequency dependence can be neglected. The impedance almost equates to the DC resistance R_0 of the HEB mixer. For frequencies higher than $2\Delta/h$, the full length of the superconducting film will be seen as a normal conductor with a normal resistance R_n .

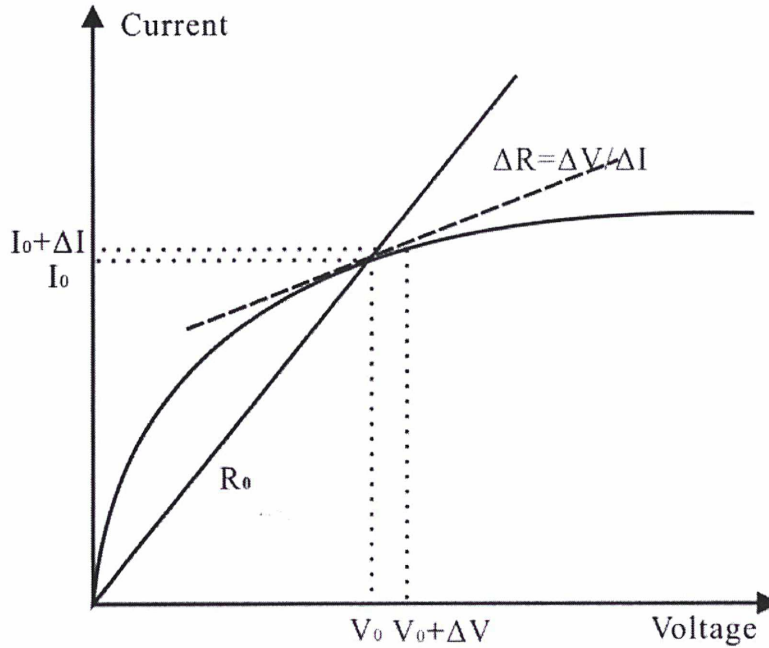


Figure 2.11: Schematic illustration of small signal impedance

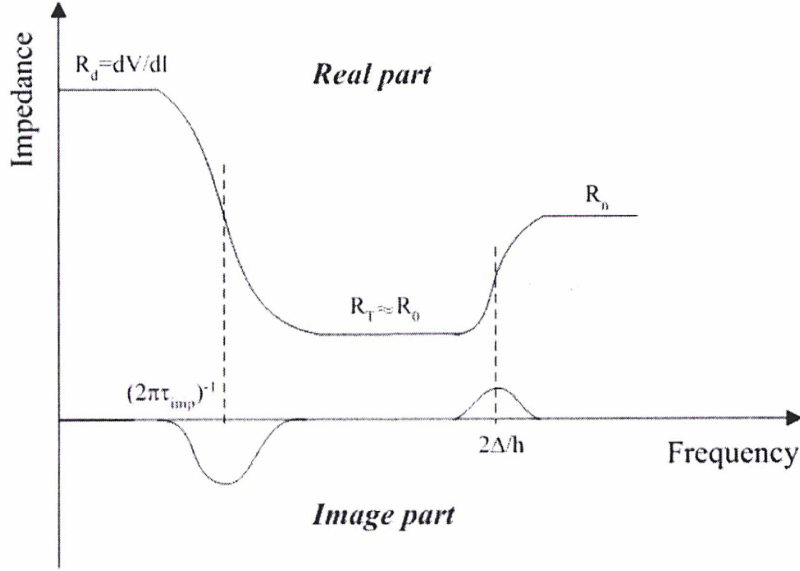


Figure 2.12: Frequency dependence of small signal impedance for superconducting HEB mixers [13].

2.3 Hot spot model

2.3.1 Standard model

The first theory to explain the physics of heterodyne mixing in a superconducting HEB is the standard model (point HEB model) proposed by Arams *et al* [3]. This model assumes that the bolometer is treated as a lumped element and the electron temperature along the bolometer bridge is uniform. In addition, equal amounts of DC and RF power are assumed to produce the same change in the resistance of the bolometer. This means they can be replaced with each other if the total absorbed power is the same. Based on these assumptions, the heat balance equation for the superconducting HEB device can be expressed as:

$$c_e V = \frac{\partial T_e}{\partial t} + P_{e \rightarrow s}(T_e, T_s) = I_0 V_0 + P(t) \quad (2.61)$$

Here c_e is electron specific heat, V is the volume of the bolometer, $c_e V = C_e$ is the heat capacity, T_e is the electron temperature, T_s is the bath temperature, $P_{e \rightarrow s}(T_e, T_s)$ is the

transferred power from electrons to the bath via the interaction with phonons. I_0 and V_0 are the bias current and voltage across the bolometer, and $P(t)$ is the absorbed radiation power. Since DC and RF power have the same effect on electron temperature, they also have the same effect on the heat capacity C_0 of HEB mixer:

$$C_0 = C_{DC} = C_{RF} = \frac{\partial R}{\partial P} \quad (2.62)$$

Where $C_{DC} = \left. \frac{\delta R}{\delta P_{DC}} \right|_{\delta P_{RF}=0}$, $C_{RF} = \left. \frac{\delta R}{\delta P_{RF}} \right|_{\delta P_{DC}=0}$.

Based on these assumptions, the absorbed RF power by the HEB mixer can be calculated from I - V curves by isothermal method. Meanwhile, the mixer conversion gain and equivalent noise temperature can also be estimated with an acceptable accuracy when the HEB mixer is operating close to its optimum point. However, the standard model is only suitable for frequency below the gap frequency. While the frequency is higher than the gap frequency, the standard model fails to predict the performance of the HEB mixer. The reason is the RF power can be absorbed uniformly by the entire bolometer microbridge while the DC power can only be absorbed in the region where the electron temperature is higher than the critical temperature of the superconductor. Also due to the basic assumption that the bolometer is a lumped element, the standard model can not explain the conversion gain and equivalent noise temperature of the HEB mixer in magnitude with respect to their voltage dependence.

2.3.2 One dimensional hot spot model

Since the standard model can't explain the mixing characteristic of the superconducting HEB mixer well, Skocpol *et al* [27] proposed the concept of hot spot based on the research of Bremer and Newhouse [26]. They found that the critical temperature of the thin superconducting film under the contact is lower than that of the microbridge due to the superconducting proximity effect. If a DC current is sent through the microbridge in combining with a strong RF signal, a resistive state will develop as soon as the critical current density of the microbridge is exceeded. But the thin superconducting film under the contact

will remain superconducting due to the cooling by the contact. The hot spot model can predict both DC characteristics and mixing performances of HEB mixers with an improved accuracy than standard model.

In hot spot model, the electronic hot spot is formed by the heating of the absorbed DC and LO power. The application of a second small signal with a frequency slightly different from the LO signal will modulate the dissipated power and consequently the length of the hot spot in the microbridge. So the resistance of the microbridge is modulated too. In other words, the mixing process in the HEB mixer is provided by the hot spot with its length oscillating at the intermediate frequency. This is the so-called hot spot mixing.

The heat balance equation for a small volume element of the microbridge can be given by:

$$K_e S \frac{dT_e}{dx} \Big|_x - K_e S \frac{dT_e}{dx} \Big|_{x+dx} + c_e S dx \frac{dT_e}{dt} = dp_{heating} - dp_{cooling} \quad (2.63)$$

Where K_e is the thermal conductivity of electrons, S is the cross section area of the bolometer, dx is the length of the element, T_e is the electron temperature, $c_e S dx = C_e$ is the heat capacity, $dp_{heating}$ and $dp_{cooling}$ are the input heating power and the power flowing out of the element respectively.

Substituting $dp_{heating} - dp_{cooling} = dp$ into Eq. 2.63 and dividing the both sides by dx yields:

$$\frac{d}{dx} (K_e S \frac{dT_e}{dx}) + \frac{dp}{dx} = c_e S \frac{dT_e}{dt} \quad (2.64)$$

Assuming the absorbed power is zero and the heat transfers from the electron subsystem to substrate is zero too, we can obtain from Eq. 2.64:

$$K_e \frac{d^2 T_e}{dx^2} = c_e \frac{dT_e}{dt} \quad (2.65)$$

Solving Eq. 2.65 yields:

$$T_e(x, t) \propto e^{-t/\tau_\theta} e^{-x/l_e} \quad (2.66)$$

Here τ_θ is the electron relaxation time, l_e is the thermal healing length. Substituting Eq. 2.66 into Eq. 2.65, we can get:

$$\frac{K_e}{l_e^2} = \frac{c_e}{\tau_\theta} \quad (2.67)$$

Here $l_e = \sqrt{D\tau_\theta}$, D is the diffusion constant [12]. Then the thermal conductivity of electrons related to the specific heat can be written as:

$$K_e = c_e D \quad (2.68)$$

For simplicity, we let $K_e S = \lambda_e$, $c_e S = C_e$, $dp/dx = P$ and substitute them into Eq. 2.64:

$$-\frac{d}{dx}(\lambda_e \frac{dT_e}{dx}) + C_e \frac{dT_e}{dt} = P \quad (2.69)$$

Since the temperature of phonon and electron in the microbridge is different, the heat balance equations in a small volume element of the microbridge can be written separately as:

$$-\frac{d}{dx}(\lambda_e \frac{dT_e}{dx}) + C_e \frac{dT_e}{dt} + P_{e-p} = P_{heating} + P_{p-e} \quad (2.70)$$

$$-\frac{d}{dx}(\lambda_p \frac{dT_p}{dx}) + C_p \frac{dT_p}{dt} + P_{p-e} + P_{p-s} = P_{e-p} \quad (2.71)$$

Here T_e is the electron temperature, T_p is the phonon temperature, P_{e-p} is the heat power transferred from electron subsystem to phonon subsystem, P_{p-e} is the heat power flown from the phonon subsystem to the electron subsystem, P_{p-s} is the heat power transferred from phonon subsystem to the substrate, C_e and C_p are the heat capacity of electron and phonon respectively, λ_e and λ_p are the thermal conductivity of electron and phonon respectively. The heat flow for electrons and phonons in a small volume element of the microbridge is schematically shown in Figure 2.13.

Since the full numerical solutions of Eq. 2.70 and Eq. 2.71 are quite intricate, different approximations have been made in hot spot model. The common simplification is to neglect the thermal conduction of phonons, which is small compared to the losses caused by the phonon escapes to the substrate. Meanwhile the electron temperature does not vary with time in steady state, so Eq. 2.70 and Eq. 2.71 can be rewritten as:

$$-\frac{d}{dx}(\lambda_e \frac{dT_e}{dx}) + P_{e-p} - P_{p-e} = P_{heating} \quad (2.72)$$

$$P_{p-s} = P_{e-p} - P_{p-e} \quad (2.73)$$

$P_{heating}$ is the sum of LO power, signal power and DC power. Assuming that P_{RF} and P_{LO} are

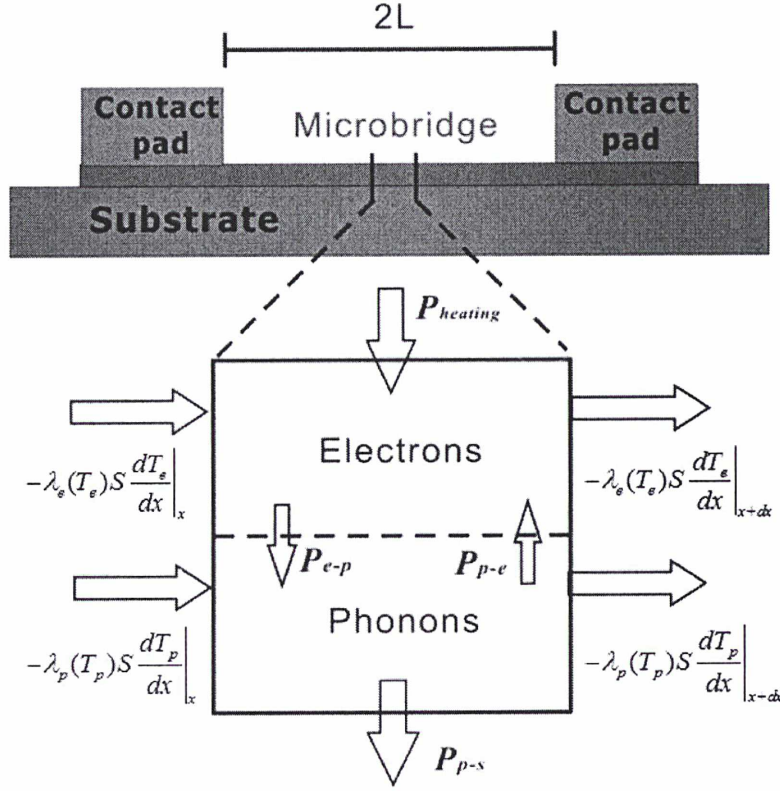


Figure 2.13: Heat flow for electrons and phonons in a small volume element of the microbridge.

uniformly absorbed in the bridge, $P_{heating}$ can be expressed as:

$$P_{heating} = \frac{P_{LO} + P_{RF}}{2L} + \frac{I_0^2 \rho(T_e)}{S} \quad (2.74)$$

Here L and S are the length and cross section area of the bolometer microbridge respectively.

$\rho(T_e)$ is the local resistivity of the bolometer microbridge.

Because coupling efficiency between electron and phonon is proportional to $\theta^n - T_{ph}^n$,

and $n=3.6$ for NbN [28], we can get:

$$P_{e-p} - P_{p-e} = A_e S (T_e^{3.6} - T_p^{3.6}) = \sigma_e (T_e^{3.6} - T_p^{3.6}) \quad (2.75)$$

Where σ_e is the electron phonon coupling efficiency and determined by:

$$\sigma_e = \frac{c_e S}{3.6 T_e^{2.6} \tau_{e-p}} \quad (2.76)$$

Since c_e is proportional to T_e , and $\tau_{e-p} = \frac{5}{10^{10} T_e^{1.6}}$, the electron phonon coupling

efficiency σ_e is temperature independent.

In the same way, the power transferred from phonons to substrate in phonon subsystem can be expressed as:

$$P_{p-s} = A_p S (T_p^4 - T_s^4) = \sigma_p (T_p^4 - T_s^4) \quad (2.77)$$

σ_p is the phonon substrate coupling efficiency and can be given by:

$$\sigma_p = A_p S = \frac{c_p}{4T_p^3 \tau_{p-s}} S \quad (2.78)$$

Substituting Eq. 2.74, Eq. 2.75, Eq. 2.78 into Eq. 2.72 and Eq. 2.73, and neglecting the signal power P_S :

$$\frac{d}{dx} (\lambda_e \frac{dT_e}{dx}) - \sigma_e (T_e^{3.6} - T_p^{3.6}) + \frac{P_{LO}}{2L} + \frac{I_0^2 \rho(T_e)}{S} = 0 \quad (2.79)$$

$$\sigma_e (T_e^{3.6} - T_p^{3.6}) - \sigma_p (T_p^4 - T_s^4) = 0 \quad (2.80)$$

Solving the phonon temperature T_p from Eq. 2.80 approximately and then substituting the expression of T_p into Eq. 2.79 yields:

$$\frac{d}{dx} (\lambda_e \frac{dT_e}{dx}) - \sigma_{eff} (T_e^{3.6} - T_s^{3.6}) + \frac{P_{LO}}{2L} + \frac{I_0^2 \rho(T_e)}{S} = 0 \quad (2.81)$$

Where σ_{eff} is the effective electron phonon coupling efficiency and is defined as:

$$\sigma_{eff} = \frac{8\sigma_e \sigma_p \sqrt{T_s}}{8\sigma_p \sqrt{T_s} + 7\sigma_e} \quad (2.82)$$

Eq. 2.81 is the core of hot spot model. It gives the electron temperature distribution along the superconducting microbridge. According to this equation, the electron temperature profile can be calculated, and therefore the resistance and consequently the I-V characteristics of the device can be calculated in terms of a certain electron temperature dependence of the resistivity. Based on small signal model, the calculation of the conversion gain and equivalent noise temperature of the HEB mixer can also be done.

In earlier hot spot model, the electron temperature dependence of the resistivity is

assumed to be a step function, which implies that it can not give any information about the performance of the device before the hot spot is formed. The resistive hot spot model [29] solves this problem by assuming a simple exponential distribution of the electron temperature dependence of the resistivity:

$$\rho(T_e) = \frac{\rho_N}{1 + e^{\frac{T_c - T_e}{\Delta T}}} \quad (2.83)$$

Here ρ_N is the normal resistivity of the device, ΔT is the width of the transition temperature when the resistivity changing from ρ_N to zero.

Substituting Eq. 2.83 into Eq. 2.81, the heat balance equation for any electron temperature can be given by:

$$\frac{d}{dx}(\lambda_e \frac{dT_e}{dx}) - \sigma_{eff}(T_e^{3.6} - T_s^{3.6}) + \frac{P_{LO}}{2L} + \frac{I_0^2 \rho_N}{S(1 + e^{\frac{T_c - T_e}{\Delta T}})} = 0 \quad (2.84)$$

However, the conversion gain calculated by this equation is slightly higher and the equivalent noise temperature is slightly lower than the measurement. The calculated results are then fitted to the measurements by adjusting the heat efficiency for RF power to a smaller empirical value [29].

2.3.3 Andreev reflection and critical current

The described models above can't calculate accurate conversion gain and noise temperature of the superconducting HEB mixer simultaneously. Therefore, two additional effects are taken into account recently for improving the resistive hot spot model: Andreev reflection at the hot spot boundaries and critical current variations along the microbridge [30].

At the interfaces between the normal conductor and the superconductor, the single electron from normal conductor with energies less than the superconductor band gap has probability to be reflected into the normal conductor when it tries to pass through the interface, this is so-called Andreev reflection. Therefore, at the interfaces between the hot spot region and the superconductor, only part of electrons with energies larger than the superconductor

band gap can carry heat across the interface, some heat energy will flow back to the hot spot. In order to evaluate the effect of Andreev reflection, we commonly assume that the quasiparticle band gap doesn't change with thermal healing length (refer to Eq. 2.67), then the heat transfer across the hot spot boundary can be estimated using a Fermi-Dirac distribution function:

$$\alpha = \frac{\int_{-\infty}^{\infty} n_E(E) dE}{\int_0^{\infty} n_E(E) dE} = \frac{kT \ln(1 + e^{\frac{\Delta(T)}{kT}}) - \Delta(T)}{kT \ln 2} \quad (2.85)$$

Where the temperature dependent superconductor band gap $\Delta(T)$ is given by:

$$\Delta(T) = \Delta_0 (1 - \frac{T}{T_c})^\gamma \quad (2.86)$$

According to BCS theory [31], γ is the exponent of the temperature dependence of the superconductor band gap and is commonly in the range from 0.5 to 1.5. According to Eq. 2.85, the Andreev transmission coefficient α can be numerically calculated. For a superconductor with a critical temperature of 10 K and a substrate temperature of 4 K, its typical value is close to 0.1. Figure 2.14 illustrates the process of Andreev reflection at the hot spot boundary of a HEB microbridge.

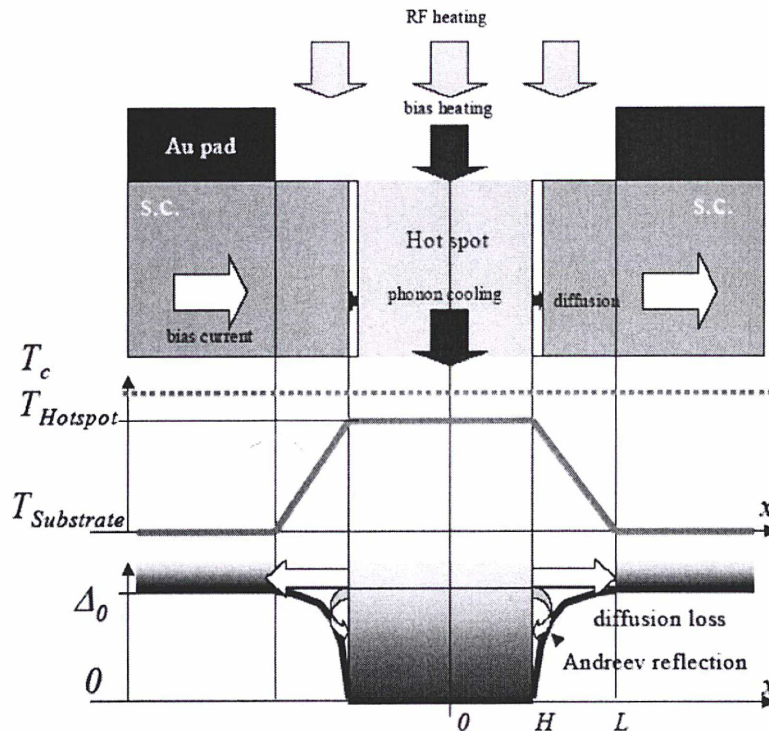


Figure 2.14: Schematic of Andreev reflection at the hot spot boundary of a HEB microbridge [30].

Another crucial parameter for improving hot spot model is the critical current. According to Ginzburg-Landau theory [32], the critical current in the microbridge of a superconducting HEB device is related to the critical temperature by:

$$j_c(T_e) = j_c(0) \left(1 - \frac{T_e}{T_c}\right)^\gamma \quad (2.87)$$

Here $j_c(T_e)$ is the critical current density at temperature T_e and $j_c(0)$ stands for the maximum value of the critical current density at $T=0$ K. Solving this equation for temperature gives the critical temperature as a function of current:

$$T_c(I_0) = \left(1 - \left(\frac{I_0}{I_c}\right)^\gamma\right)^{\frac{1}{\gamma}} T_c(0) \quad (2.88)$$

Where I_0 and I_c are the bias current and the critical current of the device at $T=0$ K, respectively.

2.4 Resume

In this chapter, we presented the operation principle and the mixing theory of the superconducting hot electron bolometer. The main parameters determining the heterodyne performances of a HEB mixer, including conversion efficiency, noise bandwidth and gain bandwidth, have been discussed and their calculation formulas have been explained and developed. We also presented the evolution of the Hot Spot model, a theoretical model describing the heat exchange mechanism inside the HEB in order to better understand the physics of the mixing process in a HEB mixer.

Bibliography

1. <https://en.wikipedia.org/wiki/Bolometer>.
2. Conceptual schematic of a bolometer. By D.F. Santavica.
3. P. L. Richards, "Bolometers for infrared and millimeter waves," *Journal of Applied Physics*, Vol. 76, No. 1, pp. 1-24, July, 1994.
4. E.M. Gershenzon, G.N. Gol'tsman, I.G. Gogidze, Y.P. Gusev, A.I. Elant'ev, B.S. Karasik, and A.D. Semenov, "Millimeter and submillimeter range mixer based on electronic heating of superconducting films in the resistive state," *Sov. Phys.-Supercond.*, 1990 (3), pp. 1582–1597.
5. Danny Wilms Floet, "Hotspot Mixing in THz Niobium Superconducting Hot Electron Bolometer Mixers," *PhD thesis*, Delft University of Technology, 2001.
6. Wei Miao, "Investigation of Hot Electron Bolometer Mixer for Submillimeter Multi-pixel Receiver Application," *PhD thesis*, I'UNIVERSITE PARIS VI, 2010
7. D.E. Prober, "Superconducting terahertz mixer using a transition-edge micro bolometer," *Applied Physics Letters*, Vol. 62, No. 17, pp. 2119-2121, 1993.
8. Stockhausen. Axel, "Optimization of hot-electron bolometers for THz radiation." *Vol. 8. KIT Scientific Publishing*, 2013.
9. S.H. Bedorf, "Development of ultrathin niobium nitride and niobium titanium nitride films for THz hot-electron bolometers," *Ph.D. thesis*, Universitat zu Koln, 2005.
10. Jacob. Willem. Kooi, "Advanced Receivers for Submillimeter and Far Infrared Astronomy", *PhD thesis*, Rijkuniversiteit Groningen, 2008.
11. Y. Zhuang, "Linear and nonlinear characteristics of NbN hot electron bolometer devices," *Ph.D. thesis*, Universitu of Massachusetts Amherst, 2002.
12. P. Khosropanah, "NbN and NbTiN hot electron bolometer THz mixers," *Ph.D. thesis*, Chalmers University of Technology, 2003.
13. H. Ekstrom, "Antenna Integrated Superconducting Mixers," *Ph. D thesis*, Chalmers University of Technology, 1995.
14. H. Ekstrom, B.S. Karasik, E.L. Kollberg, and K.S. Yngvesson, "Conversion gain and noise of niobium superconducting hot-electron-mixers," *IEEE Transactions on Microwave Theory and Techniques*, Vol. 43, No. 4, pp. 938-947, 1995.
15. Aldert van der Ziel, "Noise," 1955.

16. J.C. Mather, "Bolometer Noise: Nonequilibrium Theory," *Applied Optics*, vol. 21, pp. 1125-1129, 1982.
17. M.R. Arai, "A fundamental noise limit for biased resistors at low temperatures," *Applied Physics Letters*, Vol. 42, No. 10, pp. 906-908, 1983.
18. C. Kittel and H. Kroemer, "Thermal physics," *2ed edition*, W.H. Freeman, 1980.
19. H. Ekstrom, and B.S. Karasik, "Electron temperature fluctuation noise in hot-electron superconducting mixers," *Applied Physics Letters*, Vol. 66, No. 23, pp. 3212-3214, 1995.
20. K. Rohlf's and T.L. Wilson, "Tools of radio astronomy," *3rd edition*, Springer.
21. P. Khosropanah, W. Zhang, E.L. Kollberg, K.S. Yngvesson, J.R. Gao, T. Bansal, and M. Hajenius, "Analysis of NbN hot electron bolometer receiver noise temperatures above 2 THz with a quantum noise model," *IEEE Transactions on Applied Superconductivity*, Vol. 19, No. 3, pp. 274-277, 2009.
22. P. Santhanam, and D.E. Prober, "Inelastic electron scattering mechanisms in clean aluminum films," *Physical Review B*, Vol. 29, No. 6, pp. 3733-3736, 1984.
23. P.Y. Gousev, G.N. Gol'tsman, A.D. Semenov, E.M. Gershenzon, R.S. Nebosis, M.A. Heusinger, and K.F. Renk, "Broadband ultrafast superconducting NbN detector for electromagnetic radiation," *Journal of Applied Physics*, Vol. 75, No. 7, pp. 3695-3697, 1994.
24. T. Van Duzer, and C.W. Turner, "Principles of Superconductive devices and circuits," Elsevier, New York, 1981.
25. A.V. Sergeev, and M.Y. Reizer, "Photoresponse mechanisms of thin superconducting films and superconducting detectors," *International Journal of Modern Physics B*, Vol. 10, No. 6, pp. 635-667, 1996.
26. J.W. Bremer, and V.L. Newhouse, "Thermal propagation effect in thin superconducting films," *Physics Review Letters*, Vol. 1, No. 8, pp. 282-284, 1958.
27. W.J. Skocpol, M.R. Beasley, and T.M. Klapwijk, "Self-heating hotspots in superconducting thin-film microbridges," *Journal of Applied Physics*, Vol. 45, No. 9, pp. 4054-4066, 1974.
28. A.D. Semenov, R.S. Nebosis, Y.P. Gousev, M.A. Heusinger, and K.F. Renk, "Analysis of the nonequilibrium photo response of superconducting films to pulsed radiation by use of

- a two temperature model,” *Physical Review B (Condensed Matter)*, Vol. 52, No. 1, pp.581-590,1995.
29. P. Khosropanah, H.F. Merkel, K.S. Yngvesson, A. Adam, S. Cherednichenko, and E.L. Kollberg, “A distributed device model for phonon-cooled HEB mixers predicting IV characteristics, gain, noise and IF bandwidth,” in *Proc. of 11th International Symposium on Space Terahertz Technology*, Ann Arbor, Michigan, pp. 474-488, 2000.
 30. H.F. Merkel, “A hot spot model for HEB mixers including Andreev reflection,” in *Proc. of 16th International Symposium on Space Terahertz Technology*, Gothenburg, Sweden, pp. 404-415, 2005.
 31. J. Bardeen, L.N. Cooper, and J.R. Schrieffer, “Theory of superconductivity,” *Physical Review*, Vol. 108, No. 5, pp. 1175-1204, 1957.
 32. C.P. Poole, H.A. Farach, and R.J. Creswick, “Superconductivity,” Academic Press, San. Diego, 1995.

Chapter 3

Design and Simulation of Integrated Lens Antenna of Quasi-optical HEB Mixers

Coupling the RF radiation from the telescope into the detector with more efficiency is crucial to improve the receiver sensitivity. At microwave and millimeter wavelengths, microstrip line and coplanar line are commonly used for the coupling of RF radiation. However, at THz frequency, these transmission lines become too small to fabricate and have large insertion loss. Therefore, quasi-optical [1-3] technology becomes the first choice for the efficient coupling of RF radiation at THz frequency. The quasi-optical technology uses focus elements to realize the signal transmission. The advantages of this technology are low transmission loss and easy fabrication.

In this chapter, we first introduce the structure of a quasi-optical superconducting HEB mixer. Then we compare two methods for the simulation of far-field beam pattern of the mixer since the far-field beam pattern is of prime importance for achieving optimal coupling between any receiver and telescope.

3.1 Quasi-optical HEB mixers

A quasi-optical superconducting HEB mixer usually consists of three parts: dielectric lens, planar antenna and superconducting HEB device. The superconducting HEB device and planar antenna are integrated on a same substrate which is glued onto the flat side of a dielectric lens, as shown in Figure 3.1. The RF radiation is first focused by the dielectric lens

and then transmitted to the superconducting HEB device by the planar antenna.

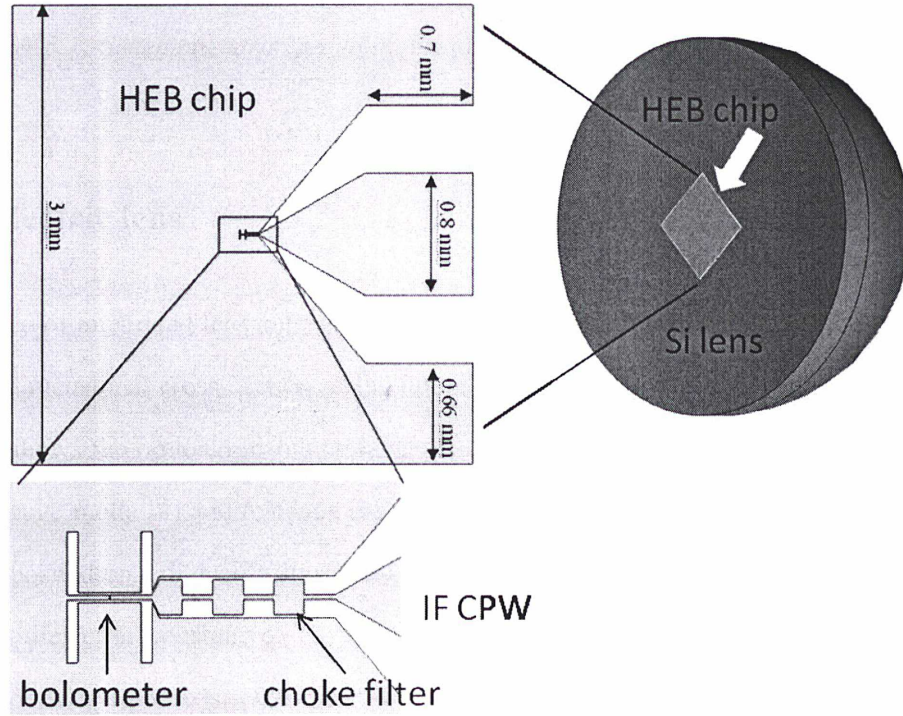


Figure 3.1: Schematic structure of a quasi-optical superconducting HEB mixer.

3.1.1 Dielectric lens

The idea of integrated lens antennas was first introduced by Rutledge and Muha in 1981 [4]. A two-dimensional cross-section of the integrated lens antenna is depicted in Figure 3.2, which also shows the optional matching layer. The lens is necessary to prevent the excitation of surface-wave mode [4] and to focus the incoming radiation to the planar feed. The planar antenna (deposited on a dielectric substrate) is placed directly on the flat side of the dielectric lens. If the dielectric constant of the lens is close to that of the antenna substrate, then substrate modes will not exist. The ratio of the power inside the dielectric to that radiated to the air is approximately $\varepsilon_r^{3/2}$ [5], where ε_r is the relative dielectric constant of the lens. For high resistive silicon, this means that only 2% of the power is radiated into the air-side. In addition, dielectric lenses can produce high quality Gaussian-beams, which is important for efficient coupling in a quasi-optical system.

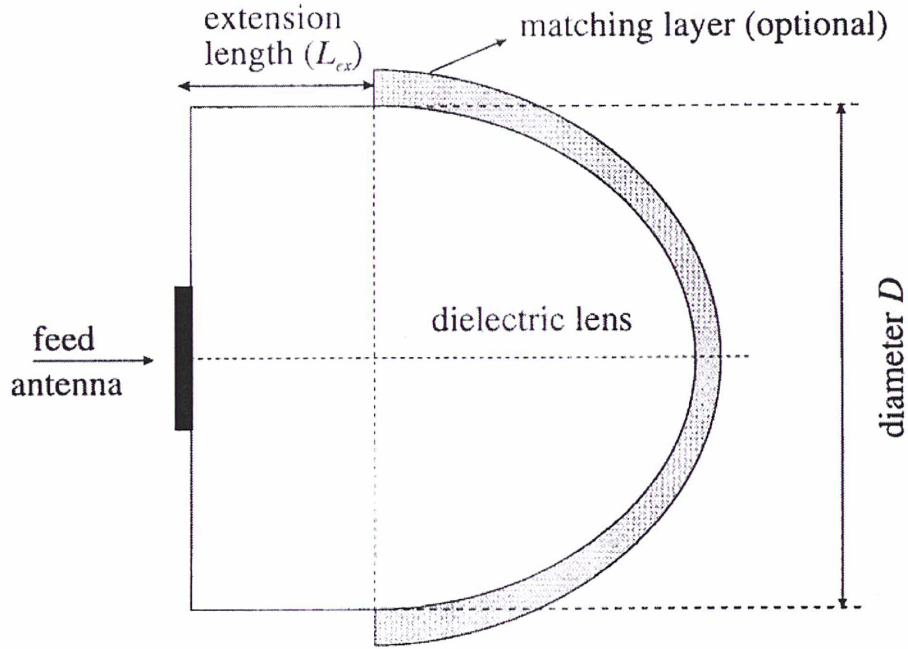


Figure 3.2: Schematic of an integrated lens antenna.

The commonly used dielectric lenses in superconducting HEB mixer are elliptical lens and extended hemispherical lens, as shown in Figure 3.3.

The elliptical lens is an ellipsoid cut off at a plane perpendicular to its major axis. It can focus all the rays to its foci. The defining equation for an ellipse is:

$$\left(\frac{x}{a}\right)^2 + \left(\frac{y}{b}\right)^2 = 1 \quad (3.1)$$

where the foci are at $\pm c$ and $c = \sqrt{b^2 - a^2}$. It is also known from optics that for a given index of refraction n , the eccentricity of the ellipse such that the geometric focus becomes the optical focus is:

$$e = \frac{\sqrt{b^2 - a^2}}{b} = \frac{1}{n} \quad (3.2)$$

From this one can derive that:

$$b = \frac{a}{\sqrt{1 - \frac{1}{n^2}}} \quad (3.3)$$

$$c = \frac{b}{n} \quad (3.4)$$

The elliptical lens can achieve high Gaussicity and directivity, but is difficult to fabricate and costs high.

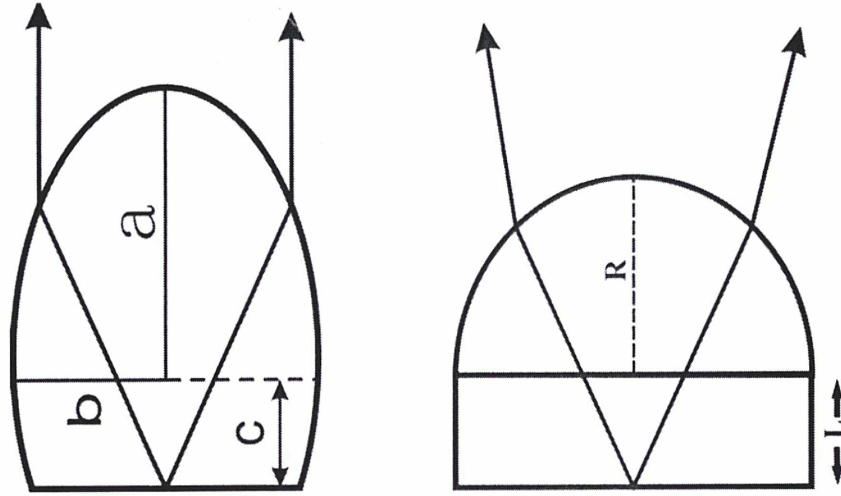


Figure 3.3: Schematic of an elliptical lens (left) and an extended hemispherical lens (right)

The extended hemispherical lens is an approximation of elliptical lens and is easy to fabricate. It is a hemisphere lens with an extension length of L . There are two special cases for extended hemispherical lens: hyperhemispherical lens and synthesized elliptical lens.

The hyperhemispherical lens has an extension length:

$$L = \frac{R}{n} \quad (3.5)$$

where n is the index of refraction. The virtual focus of the resulting spherical wave is at a distance of L_{ex} behind the center of the lens:

$$L_{ex} = \frac{n-1}{n} R \quad (3.6)$$

The f -number, defined as the ratio of the effective focal length to the diameter of the lens, can also be given by:

$$f = \frac{1}{2 \sin \theta} \quad (3.7)$$

A hyperhemispherical lens can reduce the f -number. In antenna terms, a hyperhemispherical lens bends most of the power radiated by the planar antenna towards the lens side, thereby effectively sharpening the radiation pattern and increasing the gain of the integrated antenna

by n^2 .

The synthesized elliptical lens is an approximation to a true elliptical lens, which is capable of converting a spherical wave into a plane wave. Figure 3.4 shows a schematic of a synthesized elliptical lens. According to Snell's laws, the index of refraction of the lens can be expressed as:

$$n = \frac{\sin \beta}{\sin \alpha} = \frac{\sin \beta}{\frac{L}{R} \sin \gamma} \quad (3.8)$$

Substituting $\sin \beta = \frac{y}{R}$, $\sin \gamma = \frac{y}{S}$ into Eq. 3.8 yields:

$$n = \frac{\frac{y}{R}}{\frac{L}{R} \times \frac{y}{S}} \approx \frac{\frac{y}{R}}{\frac{L}{R} \times \frac{y}{L+R}} = \frac{L+R}{L} \quad (3.9)$$

Solving from Eq. 3.9, we can get the value of extension length: $L=R/(n-1)$. Note that we assume $S \approx L+R$ when the angle is small.

The extended hemispherical lens can provide beam patterns with good Gaussicity and is easy to fabricate. These advantages make it widely used in THz superconducting receiver system. The influence of extension length on far-field beam-pattern, Gaussicity and directivity has been well studied by Buttgenbach and D.F. Filipovic in last twenty years [6-9].

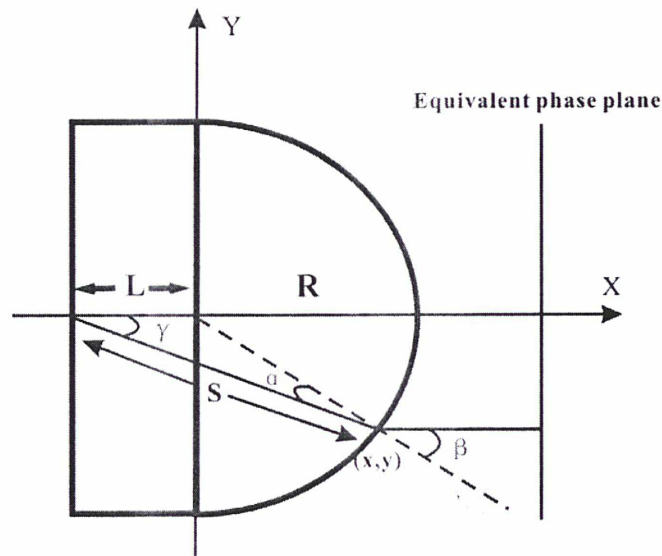


Figure 3.4: Schematic of synthesized elliptical.

3.1.2 Planar antenna

The planar antenna can be simply classified as broadband antenna and narrowband antenna according to its working bandwidth. The narrowband antenna normally has fixed resonant frequency, its working bandwidth is relatively narrow. The common narrowband antennas are double dipole antenna [10], double slot antenna [8], and annular slot antenna [11]. The broadband antenna is normally non-resonant antenna which has wide working bandwidth. The common broadband antennas are bow ties antenna [12], log spiral antenna [13] and log periodic antenna [14]. In following sections, we introduce three widely used antennas in superconducting HEB mixer.

1) Double slot antenna

Double slot antenna is a narrowband and linear polarized antenna which has good beam pattern characteristic. Figure 3.5 is the Schematic of a typical double slot antenna integrated with a HEB device in the center of the antenna. The RF radiation is received by two slots and coupled to the HEB device by a coplanar waveguide (CPW) transmission line. The slot length L and the slot width W , determining the resonant

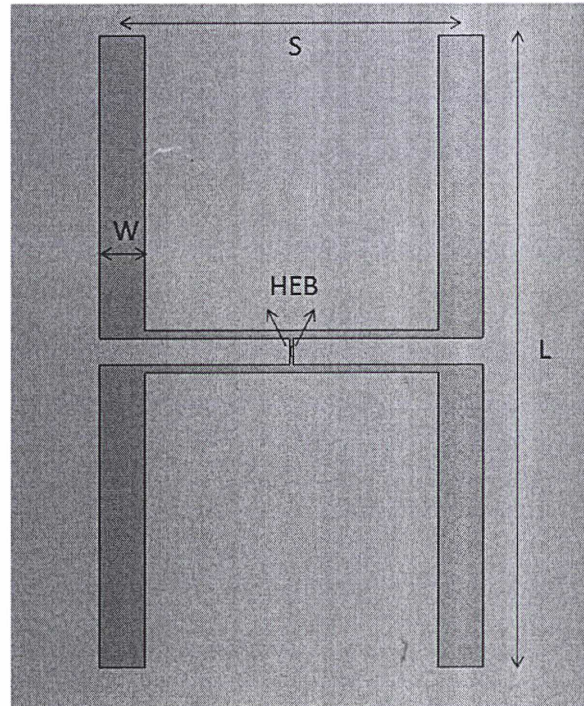


Figure 3.5: Schematic of a double slot antenna.

frequency and the input impedance of twin slot antennas, are usually taken as $0.3\lambda_0$ and $0.02\sim 0.07L$ respectively. The slot distance S controls the mutual coupling between two slots and is normally chosen as $0.17\lambda_0$.

2) Log spiral antenna

The structure of a log spiral antenna is completely determined by several angles and is not affected by linear length. Therefore, its characteristics are independent of frequency. For frequencies where the antenna arms are very short in terms of wavelength, the radiated field is linearly polarized. As the frequency increases, the field on the axis perpendicular to the plane of the antenna becomes elliptically and then circularly polarized [13].

Figure 3.6 depicts the structure of a log spiral antenna which consists of two winding conductors with the edges defined by the following equations:

$$\begin{aligned} r_1 &= r_0 e^{\alpha\varphi}, \quad r_2 = r_0 e^{\alpha(\varphi-\delta)} \\ r_3 &= r_0 e^{\alpha(\varphi-\pi)}, \quad r_4 = r_0 e^{\alpha(\varphi-\pi-\delta)} \end{aligned} \quad (3.10)$$

where δ determines the arm width, r_0 is the inner radius ($d/2$ in Figure 3.6) and α is the growth rate. The upper and lower cut off frequencies of log spiral antenna are normally determined by the inner and outer diameter, the relation between them is:

$$\frac{f_{low}}{f_{up}} = \frac{\lambda_{max}}{\lambda_{min}} \approx \frac{D}{d} \quad (3.11)$$

An empirical criterion [15] used to estimate the lower cut off frequency is $\lambda_{max} = 4D$, where λ_{max} is the wavelength of lower cut off frequency in the substrate.

The impedance of log spiral antenna is determined by α and δ , and is normally between $50\sim 100 \Omega$.

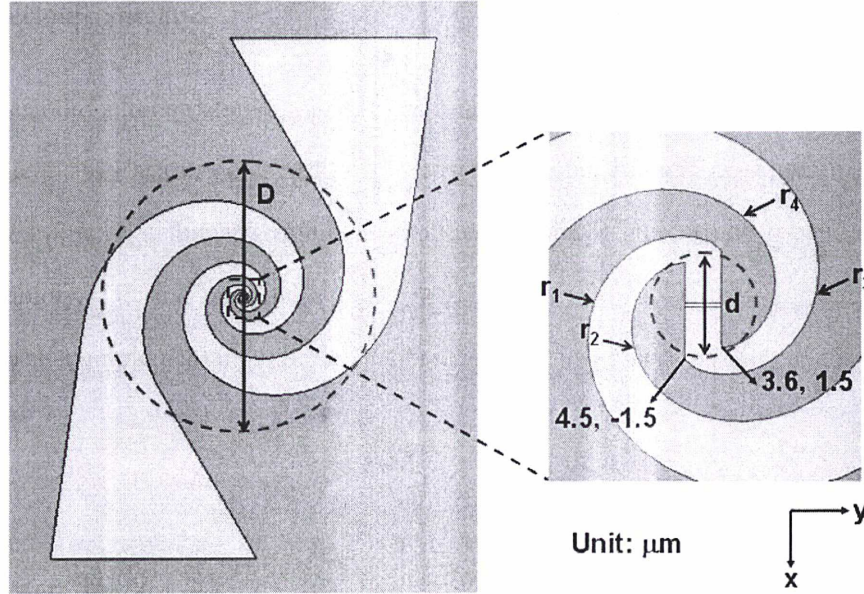


Figure 3.6: Schematic of a log spiral antenna.

3) Log periodic antenna

Log periodic antenna is also a broadband antenna like log spiral antenna. However, log periodic antenna is linearly polarized [14]. The log periodic antenna, as shown in Figure 3.7, is a modified bow tie antenna with notches and teeth to force the current to bend and change direction rapidly. The log periodic antenna should satisfy the relation $\alpha + \beta = \pi/4$ in order to keep itself self-complementary. The input impedance of a log periodic antenna can be given by:

$$Z_{ant} = \frac{Z_0}{\sqrt{2(1 + \epsilon_r)}} \quad (3.12)$$

where Z_0 is the impedance of free space ($120\pi \Omega$), ϵ_r is the dielectric constant.

The structure of the n th tooth of the log periodic antenna can be determined by parameters α and τ (as shown in Figure 3.7). τ is defined as:

$$\tau = \frac{R_n}{R_{n+1}} > 1 \quad (3.13)$$

and the width of the tooth is defined as:

$$\sqrt{\tau} = \frac{R_n}{r_n} > 1 \quad (3.14)$$

For the n th tooth, the length of center radian can be obtained by [16]:

$$l_n = \frac{R_n + r_n}{2} (\alpha + \beta) \quad (3.15)$$

Since at the designed center frequency f_n we have $l_n = \frac{\lambda_g}{2}$, λ_g is the wavelength of center frequency, Eq. 3.15 can be rewritten as:

$$\frac{\lambda_g}{2} = \frac{R_n + r_n}{2} (\alpha + \beta) \quad (3.16)$$

Therefore, the designed center frequency f_n can be expressed as:

$$f_n = \frac{4c}{\pi(R_n + r_n)\sqrt{2(1 + \epsilon_r)}} \quad (3.17)$$

From the structure of log periodic antenna, it is obvious that the electrical characteristics at a frequency f will be repeated at other frequencies given by $\tau^n f$, where n may take on any integral value. This is because when two antennas have same geometry but both of their dimensions and working frequencies differ τ times, their electrical characteristics should be the same according to antenna similarity principle. Figure 3.8 illustrates this phenomenon by simulating the input impedance of a log periodic antenna in a wide frequency range. In practice, the log periodic antenna is of finite size, and its upper and lower cutoff frequencies are determined by the shortest tooth and the longest tooth respectively.

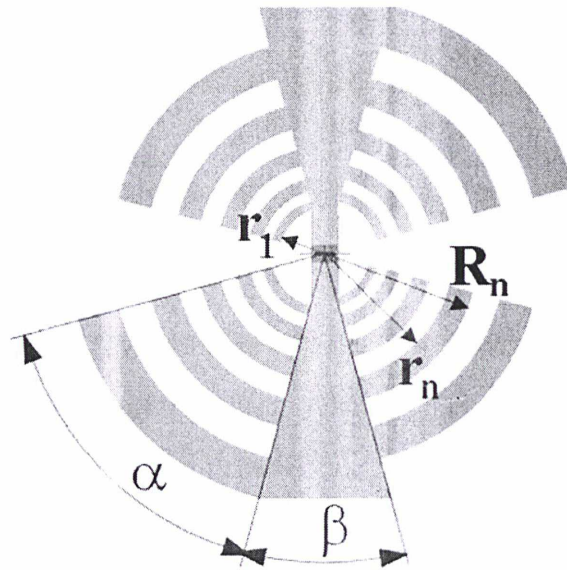


Figure 3.7: Schematic of a log periodic antenna.

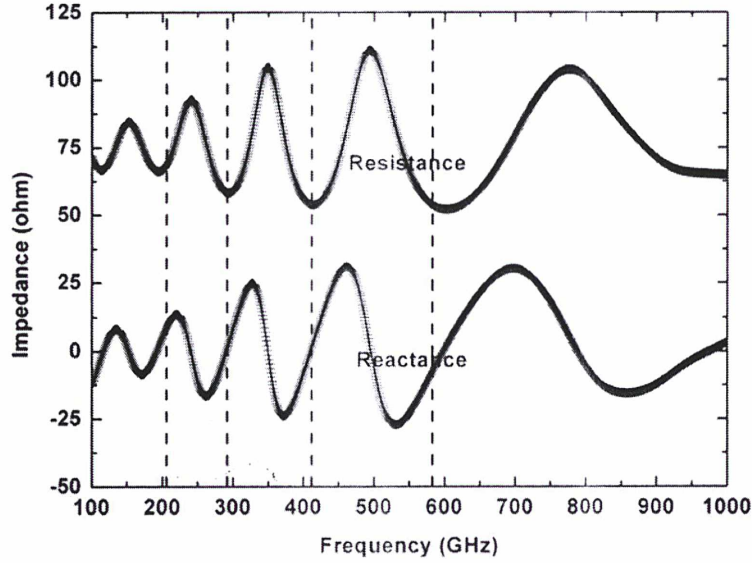


Figure 3.8: Input impedance of a log periodic antenna [17].

3.2 Far-field beam pattern simulation of integrated lens antenna

Far-field beam pattern is of prime importance for any practical application since it allows achieving optimal coupling of the receiver to a telescope as well as accurate retrieval of atmospheric data. Therefore, it is a crucial parameter in the design of a superconducting HEB mixer.

3.2.1 GO/PO hybrid calculation

The GO/PO hybrid approach of the integrated lens antenna, as described by Filipovic *et al.* [8] in 1992, applies Geometrical optics (GO) for fields inside the lens and Physical optics (PO) to obtain the near-field and far-field beam patterns outside the lens antenna. For the GO fields calculation inside the lens, the current distribution or the far-field pattern of the planar

feed needs to be calculated first. The lens-air interface is assumed to be located in the far field regime of the planar antenna, so that the planar antenna can be treated as a point source. Then the electric and magnetic fields at the lens surface can be computed using a ray-analysis technique. Once these electric and magnetic fields are known, they have to be decomposed into parallel and perpendicular component to obtain the fields just outside the dielectric lens (the interface of air/lens). Then, each component must be multiplied by the appropriate Fresnel transmission coefficient, which can be calculated by:

$$\begin{aligned}\tau_{\perp} &= \frac{2 \cos \theta^i}{\cos \theta^i + \sqrt{\left(\frac{n_2}{n_1}\right)^2 - \sin^2 \theta^i}} \\ \tau_{\parallel} &= \frac{2\left(\frac{n_2}{n_1}\right) \cos \theta^i}{\left(\frac{n_2}{n_1}\right)^2 \cos \theta^i + \sqrt{\left(\frac{n_2}{n_1}\right)^2 - \sin^2 \theta^i}}\end{aligned}\quad (3.18)$$

where n is the index of refraction and θ^i is the angle of incidence measured from the normal outwards the lens surface. The indices 1 and 2 refer to the dielectric and air side respectively, as shown in Figure 3.9.

After the fields have been multiplied by the appropriate transmission coefficient, the equivalent electric and magnetic current densities are determined just outside the dielectric surface. For these current densities, it can be written as:

$$\begin{aligned}J_s &= \hat{n} \times H_s \\ M_s &= -\hat{n} \times E_s\end{aligned}\quad (3.19)$$

where \hat{n} is the normal to the lens surface. According to diffraction theory, the electric field in observation point with a distance r_p from the hemispherical lens can be written as [18]:

$$\begin{aligned}E_{\theta} &= \frac{-jke^{-jkr_p}(L_{\phi} + \eta N_{\theta})}{4\pi r_p} \\ E_{\phi} &= \frac{jke^{-jkr_p}(L_{\theta} - \eta N_{\phi})}{4\pi r_p}\end{aligned}\quad (3.20)$$

where N and L are defined as:

$$\begin{aligned}
N(\theta, \phi) &= \iint_S J_s(r) e^{jkR \cos \psi} ds \\
L(\theta, \phi) &= \iint_S M_s(r) e^{jkR \cos \psi} ds
\end{aligned} \tag{3.21}$$

where k is the propagation constant in the free space, R the radius of the hemispherical lens and the integration is done on the whole surface S of the lens.

The GO/PO hybrid calculation can be used to calculate the radiation patterns of the integrated lens antenna with any feed antenna when its radiation properties into a dielectric half space are known. The advantages of this approach are that the calculation time is very short and the requirement of computer memory is few, which means that this approach can obtain the far-field beam pattern very quickly. However, the GO/PO hybrid calculation is not accurate enough. The origin of the inaccuracies in GO/PO is well known. It is related to neglecting the lens and the field wavefront curvatures and thus results in a failure to characterize internal resonances in dielectric objects [19].

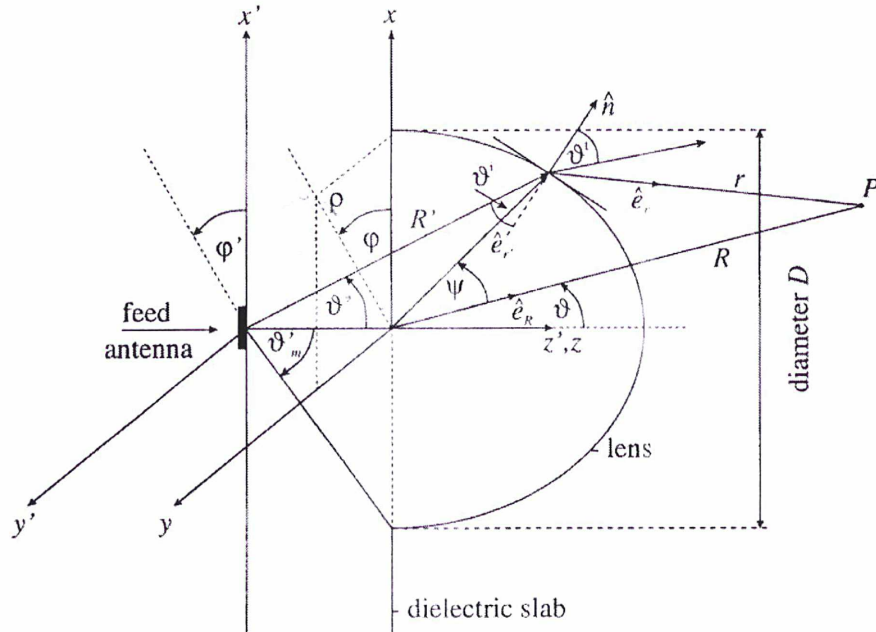


Figure 3.9: Two-dimensional cross-section of the integrated lens antenna [20]

3.2.2 MoM/PO calculation

The MoM/PO calculation is different from GO/PO calculation, it applies method of

moments (MoM) to obtain the electric and magnetic fields at the lens surface. The MoM, first proposed by Harrington in 1958 [21], is a numerical computation method for solving the electromagnetic problems. It solves the integral equation and differential equation by discretizing continuity equation to algebraic equations. The principle is transforming an integral or differential equation into an equation with integral or differential operator first, then rewriting the functions into the linear combination of a set of basic functions and substituting them into the operator equation, finally applying two chosen weight functions to the operator equation to obtain the matrix equation or algebraic equations.

The MoM is an accurate numerical simulation method. Its accuracy is only limited by the accuracy of calculation and model, so it can achieve arbitrary precision of calculation and solution. Meanwhile, it is a stable calculation method which means there is no pseudo solution. Since it is based on the integral equation, it can calculate the electromagnetic field distribution of an object with any shape, especially suitable to simulate the object with complex structure.

The disadvantages of MoM are that it needs a great many of computer memory and takes a much longer time to calculate. This is because there are a great number of matrixes produced by discrete equations, which need a large number of numerical solutions.

In this work, we use an electromagnetic simulation software "FEKO" to achieve the simulations applying the method of moments [22].

3.2.3 Comparison of two simulation methods

In far-field beam pattern simulation of a quasi-optical superconducting HEB mixer, the MoM/PO calculation can simulate the real structure of the HEB mixer in contrast to GO/PO calculation. The GO/PO calculation does not take the shape of HEB chip into account and assumes the whole mixer structure as a dielectric lens, as shown in the left of Figure 3.10. In a quasi-optical superconducting HEB mixer, the superconducting HEB device and planar antenna is fabricated on a dielectric substrate chip which is glued to the dielectric lens. The

dielectric substrate chip is normally a cube with a thickness of a few hundred microns, as shown in the right of Figure 3.10. In order to see the effect of this structure difference, we simulate the far-field beam patterns of two structures by using MoM/PO calculation since it is more accurate and can simulate an object of complex structure. The results are shown in Figure 3.11, it is obvious that the difference in mixer structure results difference in far-field beam pattern. In addition, we simulated the beam pattern of the same superconducting HEB mixer by using both MoM/PO and GO/PO method, as shown in Figure 3.12. The result shows that the simulated far-field beam patterns are also different, which can be attributed to the difference of the calculation accuracy and the simulated structure of HEB mixer.

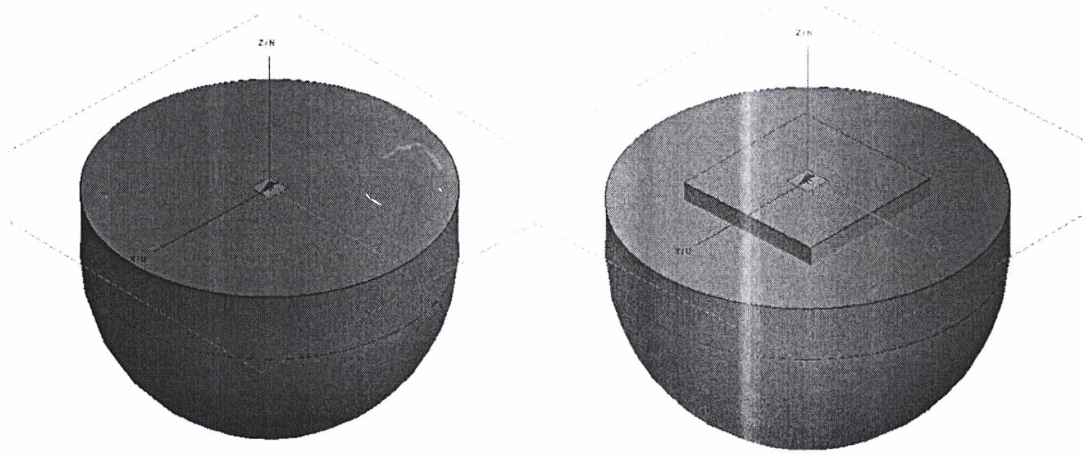


Figure 3.10: Approximate structure in GO/PO hybrid calculation (left) and the real structure (right) of a quasi-optical superconducting HEB mixer.

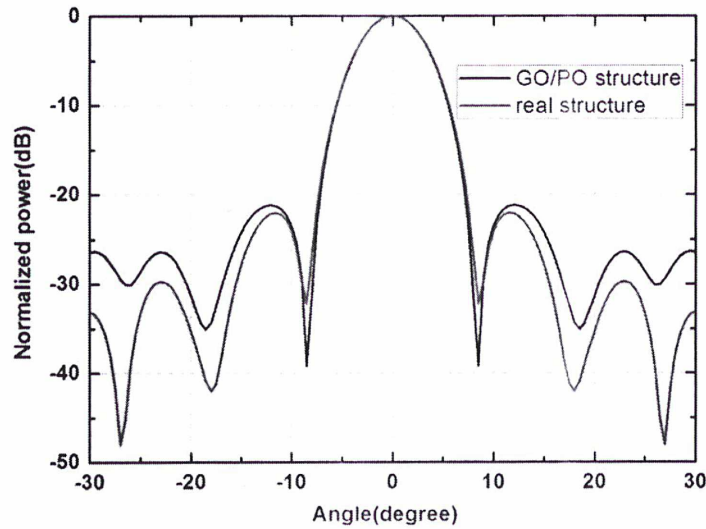


Figure 3.11: Simulated far-field beam pattern with two different mixer structures.

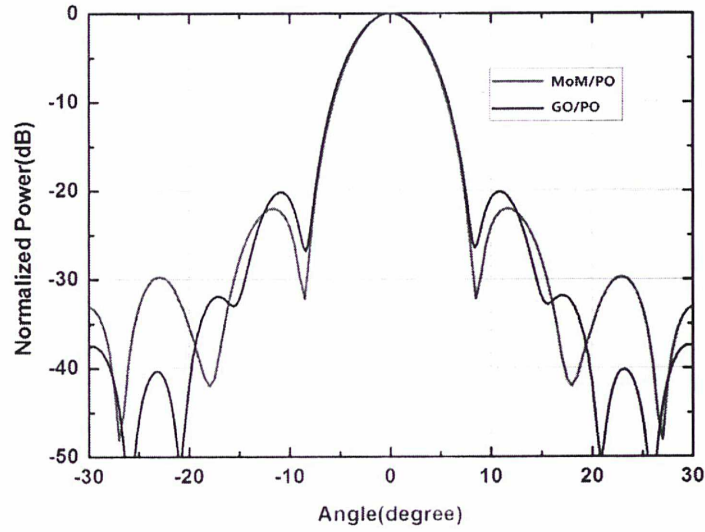


Figure 3.12: Simulated beam pattern by two calculation methods of the same HEB mixer.

Although the MoM/PO method is more accurate, it takes a long time for calculation and requires a large amount of computer memory. For simulating the beam pattern of a hemispherical lens with a radius of 3.5 mm at 600 GHz, the MoM/PO method needs 16 GB memory and 6 hours of computing time with a 8-core CPU @ 3.4 GHz. However, the GO/PO method only needs very little memory and takes less than one minute to calculate the beam pattern of the same integrated lens antenna. Figure 3.12 also shows that the main lobes of two simulations accord well, and only the side lobes are slightly different. Furthermore, the difference between two methods will be smaller when the lens size increases. Therefore, we conclude that the MoM/PO method can give a more precise beam pattern than GO/PO method. However, the GO/PO method is still suitable for simulations of electrically large objects which are difficult to be calculated by MoM/PO method.

3.3 Gaussian beam and Gaussian coupling efficiency

The propagation of electromagnetic wave at THz frequency can be described by Gaussian beam propagation. The mathematical expression of Gaussian beam is the paraxial approximation solution of Helmholtz equation which is normally expressed as [23]:

$$\nabla^2 \hat{\psi} + k^2 \hat{\psi} = 0 \quad (3.22)$$

assuming the propagation is along z axis, $\hat{\psi}$ represents electric or magnetic field and its change in x, y axis is much lower than in z axis, then we can assume that:

$$\hat{\psi} = \psi(x, y, z)e^{-jkz} \quad (3.23)$$

so the paraxial wave equation can be expressed by:

$$\nabla_t^2 \psi - 2jk \frac{\partial \psi}{\partial z} = 0 \quad (3.24)$$

where in cylindrical coordinates: $\nabla_t^2 = \frac{\partial^2}{\partial r^2} + \frac{1}{r} \frac{\partial}{\partial r} + \frac{1}{r^2} \frac{\partial^2}{\partial \theta^2}$

The fundamental solution of Eq. 3.24 is the first order Gaussian beam. If $\hat{\psi}$ represents electric field, the solution of Eq. 3.24 can be expressed as the normalized electric field distribution:

$$E(r, z) = \sqrt{\frac{2}{\pi w^2}} \exp\left(-\frac{r^2}{w^2} - jkz - \frac{j\pi r^2}{\lambda R} + j\phi_0\right) \quad (3.25)$$

where r is the vertical distance to propagation axis, z the propagation direction, w the beam radius, λ the wavelength, R the radius of curvature and ϕ_0 the phase shift of Gaussian beam.

The far field of a Gaussian beam is the Fourier transform of its near field on an aperture and the normalized electric field distribution is of the form [24]:

$$E(\theta, z) = \exp\left(-\frac{\theta^2}{\theta_0^2} - jkz - \frac{j\pi\theta^2}{\theta_1^2} + j\phi_0\right) \quad (3.26)$$

where θ is the direction in the far field from boresight. The value θ_0 controls the amplitude term and θ_1 controls the phasing term of the Gaussian beam respectively.

An important parameter in quasi-optical system is the coupling efficiency between an antenna and a Gaussian beam. The Gaussian beam efficiency is calculated using a normalized inner product between the antenna radiation pattern and the Gaussian beam pattern in the angular domain. It can be defined as:

$$\eta = \left| \langle \psi_{\text{antenna}} | \psi_{\text{Gauss}} \rangle \right|^2 \quad (3.27)$$

Then with substitution of the appropriate field representations, the Gaussian beam coupling

efficiency can be written as:

$$\eta_{Gauss} = \frac{\left| \int_0^{2\pi} \int_0^{\pi/2} [n_{co, far} E(\theta, \varphi)] \exp[-(\frac{\sin \theta}{\theta_0})^2] \exp[\pm j\pi(\frac{\theta}{\theta_1})^2] \sin \theta \cos \theta d\theta d\varphi \right|^2}{\int_0^{2\pi} \int_0^{\pi/2} |E(\theta, \varphi)|^2 \sin \theta d\theta d\varphi \int_0^{2\pi} \int_0^{\pi/2} |n_{co, far}|^2 \exp[-2(\frac{\sin \theta}{\theta_0})^2] \sin \theta \cos \theta d\theta d\varphi} \quad (3.28)$$

where $n_{co, far}$ is the polarization of the Gaussian beam.

3.4 Conclusion

In this chapter, we studied in detail the structure of a quasi-optical superconducting HEB mixer with integrated lens antenna. In particular, we have focused the discussion on the design of dielectric lens and planar antenna since they are crucial for determining the far-field beam pattern of the mixer. In order to get an efficient and reliable design, we applied two methods for the simulation of the quasi-optical structure: MoM/PO and the GO/PO approximation. The comparison between two simulation ways has been performed and the advantages and disadvantages of each method have been discussed.

Bibliography

1. P. Yagoubov, M. Kroug, H. Merkel, E. Kollberg, J. Schubert, and H. W. Hubers, G. Schwaab, G. Gol'tsman and E. Gershenzon, "NbN hotelectron bolometric mixers at frequencies between 0.7 and 3.1 THz," *Superconductor Science and Tech.*, vol 12 (11), pp 989–991, Nov. 1999.
2. J. Zmuidzinas and P. L. Richards, "Superconducting detectors and mixers for millimeter and submillimeter astrophysics," *Proc. IEEE*, vol. 92, no. 10, pp. 1597–1616, Oct. 2004.
3. E. Gerecht, C. F. Musante, Y. Zhuang, K. S. Yngevesson, T. Goyetter, J. C. Dickinson, J. Waldman, P. A. Yagoubov, G. Gol'tsman, B. M. Voronov, and E. M. Gershenzon, "NbN hot-electron bolometric mixers---a new technology for low-noise THz receivers," *IEEE*

- Trans. Microwave Theory Tech.*, vol. 47, pp. 2519–2527, 1999
4. D.B. Rutledge and M.S. Muha, “Imaging antenna arrays,” *IEEE Transactions on Antennas and Propagation*, Vol. 30, pp. 535-540, 1982.
 5. D.B. Rutledge, D.P. Neikirk, and D.P. Kasilingam, “Integrated circuit antennas,” *Journal of Infrared and Millimeter Waves*, Vol. 10, pp. 1-90, K.J. Button, Ed. New York, Academic Press, 1983.
 6. D.F. Filipovic, “Analysis and design of dielectric-lens and planar multiplier circuits for millimetre-wave applications,” PhD thesis, 1995.
 7. T. Buttgenbach, “An Improved Solution for Integrated Array Optics in Quasi-Optical mm and Submm Receivers: the Hybrid Antenna,” *IEEE Transactions on Microwave Theory and Techniques*, Vol. 41, No. 10, pp. 1750-1761, 1993.
 8. D.F. Filipovic, S.S. Gearhart, G.M. Rebeiz, “Double-Slot Antennas on Extended Hemispherical and Elliptical Silicon Dielectric Lenses,” *IEEE Transactions on Microwave Theory and Techniques*, Vol. 41, No. 10, pp. 1738-1749, 1993.
 9. D.F. Filipovic, G.M. Rebeiz, “Double-Slot Antennas on Extended Hemispherical and Elliptical Quartz Dielectric Lenses,” *International Journal of Infrared and Millimeter Waves*, Vol. 14, No. 10, pp. 1905-1924, 1993.
 10. A. Skalare, H. Vandestadt, T. Degraauw, R.A. Panhuyzen, and M.M.T.M. Dierichs, “Double dipole antenna SIS receivers at 100 and 400 GHz,” in *Proc. of 3th International Symposium on Space Terahertz Technology*, Michigan, USA, pp. 222-233, 1992.
 11. S. Raman and G.M. Rebeiz, “Single- and dual-polarized millimeter-wave slot-ring antennas,” *IEEE Transactions on Antennas and Propagation*, Vol. 44, No. 11, pp. 1438-1444, 1996.
 12. F. Ronnung, S. Cherednichenko, D. Winkler, and G.N. Gol’tsman, “A nanoscale YBCO mixer optically coupled with a bow tie antenna,” *Superconductor Science and Technology*, Vol. 12, No. 11, pp. 853-855, 1999.
 13. J.D. Dyson, “The equiangular spiral antenna,” *IEEE Transactions on Antennas and Propagation*, Vol. 7, No. 2, pp. 181-187, 1959.
 14. R.H. Duhamel and F.R. Ore, “Logarithmically periodic antenna designs,” *IRE International Convention Record*, Vol. 6, pp. 139-151, 1958.

15. J. Zmuidzinas, and H.G. LeDuc, "Quasi-optical slot antenna SIS mixers," *IEEE Transaction on Microwave Theory and Techniques*, Vol. 40, No. 9, pp. 1797-1804, 1992.
16. G.V. Eleftheriades and G.M. Rebeiz, "Self and mutual admittance of slot antennas on a dielectric half space," *International Journal of Infrared and Millimeter waves*, Vol. 14, No. 10, pp. 1925-1946, 1993.
17. W. Miao, "Investigation of Hot Electron Bolometer mixers for Submillimeter Multi-pixel Receiver Applications," *Ph.D. thesis*, Universite Paris VI, 2010.
18. M. H. Chung and M. Salez, "Design and analysis of a hybrid feed antenna for a flux-flow oscillator integrated 460 GHz SIS receiver," in *Proc. of 11th International Symposium on Space Terahertz Technology*, Michigan, USA, pp. 626-638, 2000.
19. Boriskin, A. V., Godi, G., Sauleau, R., & Nosich, A. I, "Small hemielliptic dielectric lens antenna analysis in 2-D: boundary integral equations versus geometrical and physical optics," *Antennas and Propagation, IEEE Transactions on*, 56(2), 485-492, 2008.
20. M.J.M. van der Vorst, "Integrated lens antennas for submillimeter-wave applications," *Ph.D. thesis*, Technische Universiteit Eindhoven, 1999.
21. R. H. Harrington, "Field computation by moment methods," New York: McMillan, 1968
22. FEKO: A computer code for the analysis of electromagnetic problems. EM Software & Systems-S.A. (Pty) Ltd., Stellenbosch, South Africa.
23. Goldsmith, P.F., "Quasi-optical techniques at millimeter and submillimeter wavelengths," *Chapman & Hall*, 1998.
24. G. M. Rebeiz, "Millimeter-wave and terahertz integrated circuit antenna," in *Proc. of IEEE*, Vol. 80, No. 11, pp. 1748-1770, Nov. 1992.

Chapter 4

Investigation of Far-field Beam Patterns of Quasi-optical HEB Mixers

For the quasi-optical superconducting HEB mixer studied in this work, its far-field beam pattern is mainly determined by the material (normally silicon) permittivity and the shape of the focus lens. Therefore, in order to optimize the far-field beam pattern and the design of superconducting HEB mixer, we need to know the accurate value of silicon dielectric constant.

In this chapter, we first present a quasi-optical vector measurement system for obtaining material permittivity. Then we measure the far-field beam patterns of a superconducting HEB mixer using a direct far-field and a vector near-field measurement system. We also investigate the effect of HEB bias voltage and bath temperature on measured far-field beam patterns.

4.1 Measurement of Si dielectric constant

High resistivity silicon is a commonly used material at THz wavelength. It is widely used in THz receiver system [1, 2] and integrated circuit [3, 4] since it is relatively cheap and easy to fabricate. High resistivity silicon is normally chosen to be the material of focus lens for HEB mixers and the substrate of HEB device because of its high permittivity and low absorption loss at THz frequency. However, it is difficult to find out its accurate complex permittivity (especially at low temperature and THz frequency) in the literature or from manufacturers' measurement data.

4.1.1 Measurement setup

Broadband methods such as FTS and TDS can measure the permittivity of a dielectric slab in a large bandwidth, but the SNR is limited at millimeter and even part of submillimeter wavelengths. On the other hand, the cylindrical resonant cavity method is limited to microwave frequencies [5]. Here we adopt a broadband frequency-domain method using a vector network analyzer (VNA) [6] combined with a quasi-optical transmissometer of a dynamic range as high as 110 dB to ensure high measurement precision of permittivity.

The quasi-optical transmissometer used in our measurement is shown in Figure 4.1. Two biconvex focus lenses are employed as quasi-optical collimators. Their sizes and positions are designed to have a Gaussian beam-waist at the sample location and a beam width smaller than the radius of the sample [7]. The quasi-optical circuit is driven by a vector-network-analyzer (MVNA 8-350GHz) which uses Schottky diode devices as source and detector. The VNA is employed to measure the complex transmission coefficient over an extended frequency range of 8-350 GHz through harmonic multiplication of a sweepable centimeter source (S_1) which provides a nominally flat output power in the frequency range $F_1=8\sim 18$ GHz. The millimeter wave signal used in our measurement is produced by a Schottky-diode multiplier optimized for a desired harmonic N . Detection is then achieved by mixing the millimeter wave signal ($F_{mm} = N \times F_1$) with the signal from a second centimeter source (S_2) at a second Schottky diode (harmonic mixer). The detection LO (S_2) is PLL-controlled by the source LO (S_1) with a frequency offset f in the MHz range, and the harmonic ranks N of both LO are the same.

For measurements at cryogenic temperature, the sample is placed in a cryogenic dewar and is surrounded by blackbody absorber to reduce reflections, as is shown in Figure 4.2.

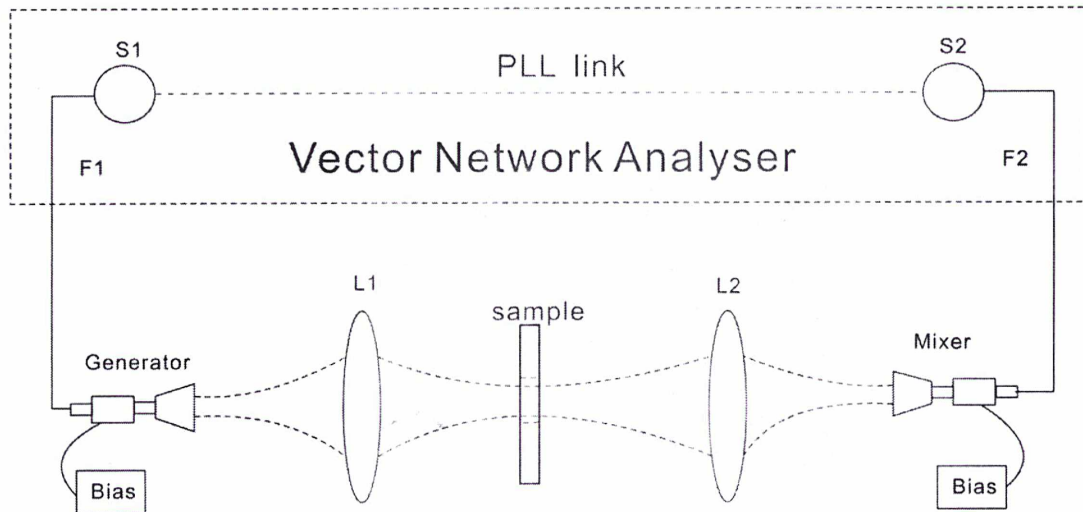


Figure 4.1: Schematic of the quasi-optical transmissometer. $L1$ and $L2$ denote two focus lenses. $S1$ and $S2$ are 8-18GHz centimeter sweepers. The Schottky multiplier (at left) and harmonic mixer (at right) work with harmonics up to 12.

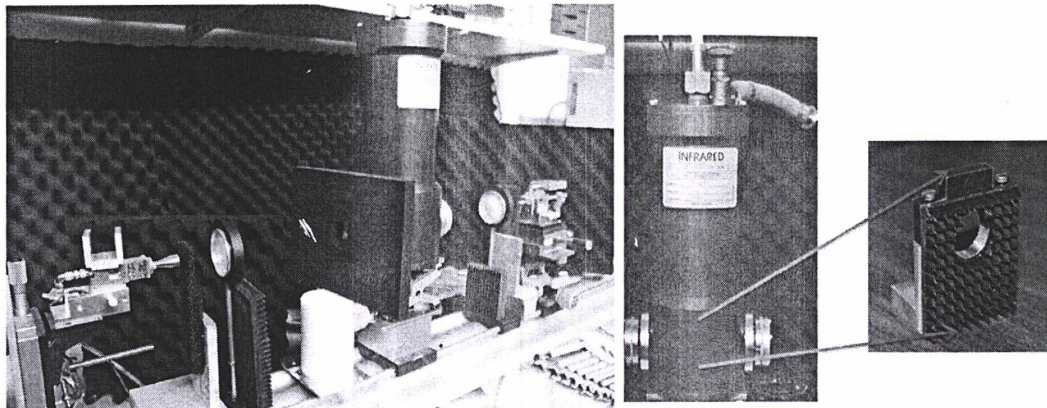


Figure 4.2: Picture of the low temperature measurement system (left), the cryogenic dewar and the holder of sample (right).

4.1.2 Calculation of permittivity

The procedure to determine the complex permittivity of a plate-sample is as follows. The transmittance spectra of a sample is measured by the VNA by recording the ratio of the complex amplitudes of the transmitted (with the sample in place) and incident (with the sample removed) signals. The transmitted signal is the sum of an absorption behavior and a resonant behavior - the dielectric slab behaving as a Fabry-Pérot resonator.

The permittivity ε , or the refractive index n , can be deduced from the measured transmittance spectra data by the observed period ΔF between two successive transmission maxima. The relationship between the periodicity of the transmission maxima ΔF and the refractive index n is as following:

$$\Delta F = \frac{C}{2nd} \quad (4.1)$$

where d is the sample thickness, c the speed of light in vacuum, and Δf the frequency interval between two successive maxima of the measured transmission spectra. Eq. 4.1 is for broadband estimation, namely an averaged refractive index over the whole measured frequency range. The refractive index at a single frequency can be determined by the observed phase variation $\Delta\Phi$:

$$\frac{(n-1)*d*f}{C} = \frac{\Delta\psi}{360^\circ} + k \quad (4.2)$$

where f is the frequency, k an integer number of turns, and $\Delta\Phi$ the phase rotation corresponding to less than one turn.

The loss tangent is obtained from the damping of the transmitted signal and is given by:

$$\tan \delta = \frac{1.1\alpha}{nF} \quad (4.3)$$

where α is the attenuation with unit of dB/cm and the resonance frequency F with unit of GHz. The parameter α is determined by measuring the loss at the transmission maxima.

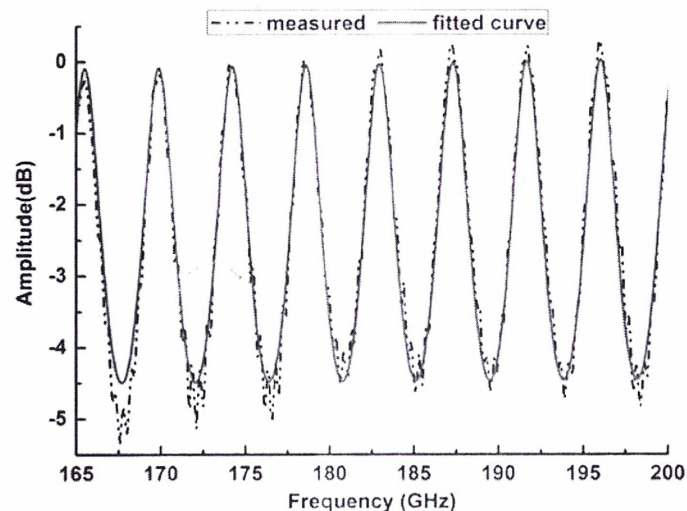
4.1.3 Si permittivity at 77 K and 295 K

We have measured the permittivity of high resistivity silicon at 77 K and 295 K. The silicon sample under study has a thickness of 10.05 mm and a diameter of 20 mm, the resistance is larger than 10 k Ω cm. For measurements at 77 K, the sample is placed in a cryogenic dewar which is filled with liquid Nitrogen to keep the temperature at 77K.

Figure 4.3 illustrates the measured and fitted complex transmittance spectrum of the silicon sample from 165 GHz to 200 GHz at 295 K. High peak values in the amplitude spectrum indicates low loss of this material. A least mean squares fitting was used in calculating the permittivity in order to obtain accurate results. The measured complex

transmittance spectrums were firstly fitted and then used to calculate the permittivity by Eq. 4.1 and Eq. 4.2. Obviously, the fitted curves coincide well with the measured results, indicating fairly high accuracy of measurement. The obtained average value of refractive index is 3.42, i.e., 11.71 for permittivity, which is very close to previously reported results in this frequency range [8, 9]. The calculated loss tangent by Eq. 4.3 is 5.8×10^{-5} . This value is not accurate since high-resistivity silicon is a low-loss material and the attenuation in amplitude spectrum is too small to be observed. Other techniques such as dielectric-resonator and composite dielectric-resonator are needed for the measurement of low-loss material [5]. What's more, the refractive index is crucial but the accurate value of loss tangent isn't important for the design and simulation of superconducting HEB mixers.

The fluctuations in measured transmittance spectrums will result in errors in the determination of sample's refractive index. These fluctuations are mainly caused by standing waves. Any reflections caused by impedance discontinuities and imperfect alignment within the measurement system would give rise to standing waves. Experimental and computational methods have been used to reduce them. In the measurement, wide-band in-wave-guide isolators and additional attenuators have been added to the VNA head-units; both of them are effective in suppressing standing waves. Meanwhile, a computational time-gating function and numerical FFT have been applied to filter out any short-period standing waves in transmittance spectrum. Care had been taken when these functions are employed since the total effective path-length for multiple reflections within a low loss sample could approach the path length between the components of the transmissometer.



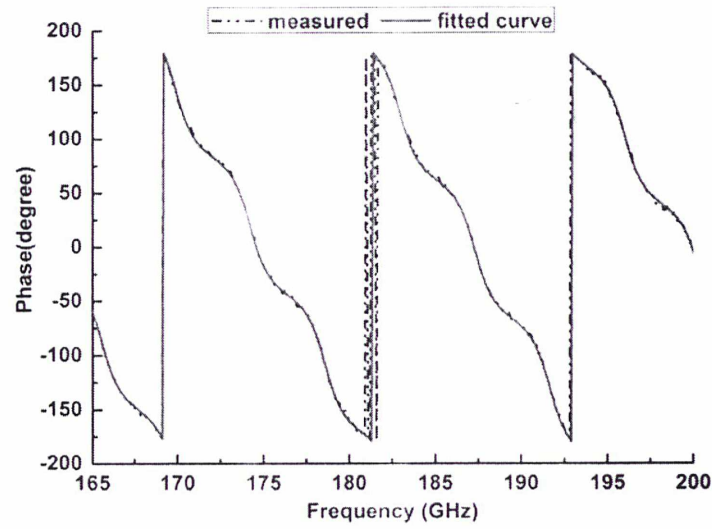
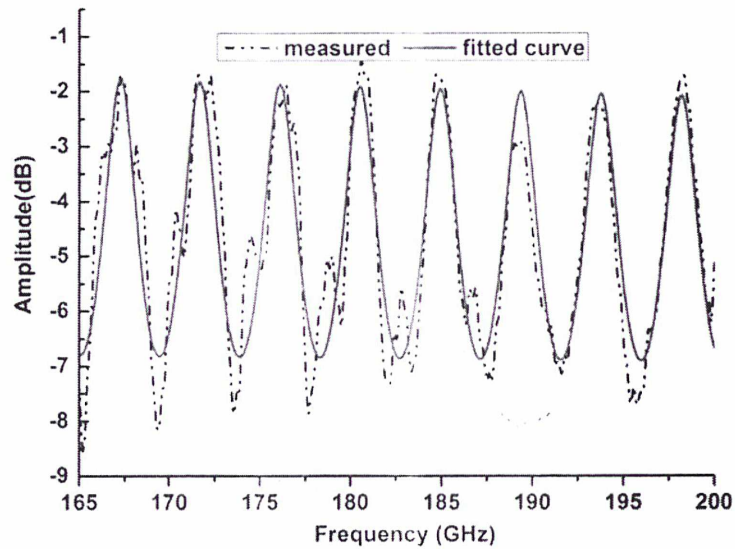


Figure 4.3: Measured and fitted complex transmittance spectrum of silicon at 295K. The upper plot is amplitude spectrum and the lower plot is phase spectrum. The dotted line is measured transmittance and the solid line is fitted curve.

Figure 4.4 illustrates the measured complex transmittance spectrums of the silicon sample at 77 K. Some fluctuations caused by the multi-reflections inside the cryostat can be observed both in amplitude and in phase spectrum. In spite of that, fitted phase curve is in good agreement with measured result. The obtained average value of refractive index is 3.38, which is 11.43 for permittivity.



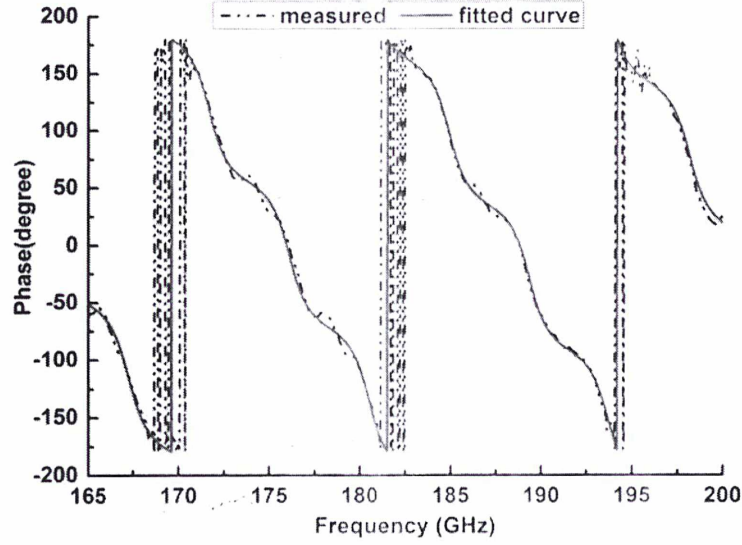


Figure 4.4: Measured and fitted complex transmittance spectrum of silicon at 77K. The upper plot is amplitude spectrum and the lower plot is phase spectrum. The dotted line is measured transmittance and the solid line is fitted curve.

4.2 Far-field Beam pattern simulation with measured Si permittivity

The prime application of our permittivity measurement is for optimizing the far-field beam pattern of the superconducting HEB mixer and improving its sensitivity. Most people adopt silicon's room-temperature permittivity (normally 11.7) in designing quasi-optical superconducting HEB mixers [10-12]. One often observes, however, the difference in the beam pattern between the simulation and the measurement. Different permittivity at low temperatures might be one of the reasons. In order to illustrate this standpoint, we simulated far-field beam patterns of a quasi-optical HEB mixer at 200 GHz with previously measured silicon's permittivity at 77 K and 295 K.

Figure 4.5 illustrates the difference in beam patterns caused by adopting two silicon's permittivity in simulation: the main-lobe has a width difference of 1.2° at -10 dB and the side-lobe has an amplitude difference of 2.5 dB. These simulations were done with an

extended hemispherical lens with a radius of 6.35 mm and an extension length of 2.45 mm. The integrated two-slot planar antenna has a slot length L of $0.28 \lambda_0$, slot separation S of $0.155 \lambda_0$ and slot width W of $0.0133 \lambda_0$, where λ_0 is the free space wavelength.

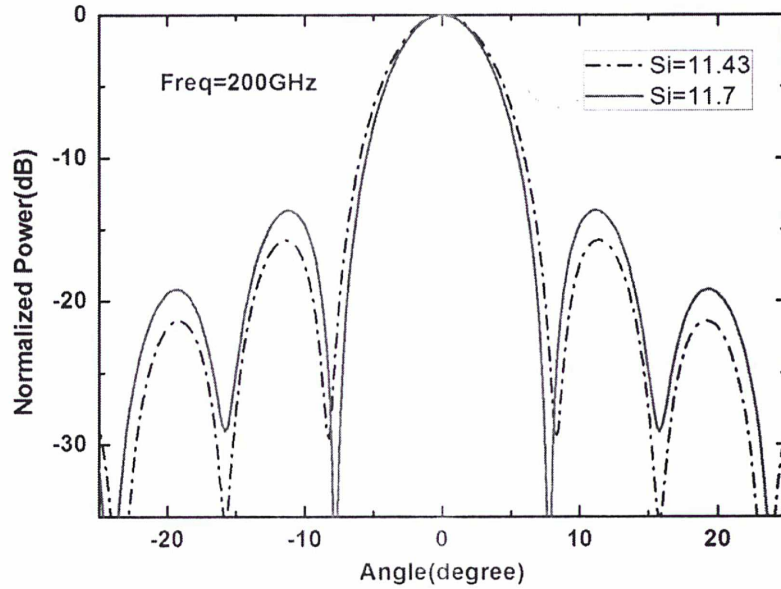


Figure 4.5: Simulated far-field beam-patterns with silicon's permittivity measured at 77 K and 295 K

What's more, we simulated far-field beam patterns by adopting two silicon's permittivity at different frequencies: 100 GHz, 150 GHz, 200 GHz, 250 GHz, 300 GHz and 400 GHz. As shown in Figure 4.6, the difference between two beam patterns increases from 100 GHz to 200 GHz and then decreases from 200 GHz to 400 GHz. This phenomenon could be explained as follow: when the frequency increases from 100 GHz to 200 GHz, the optical path inside the lens increases; but when the frequency increases higher, the hemispherical lens becomes diffraction limited and makes the beam pattern mainly determined by the shape of the lens. Hence the influence of the dielectric constant becomes less important.

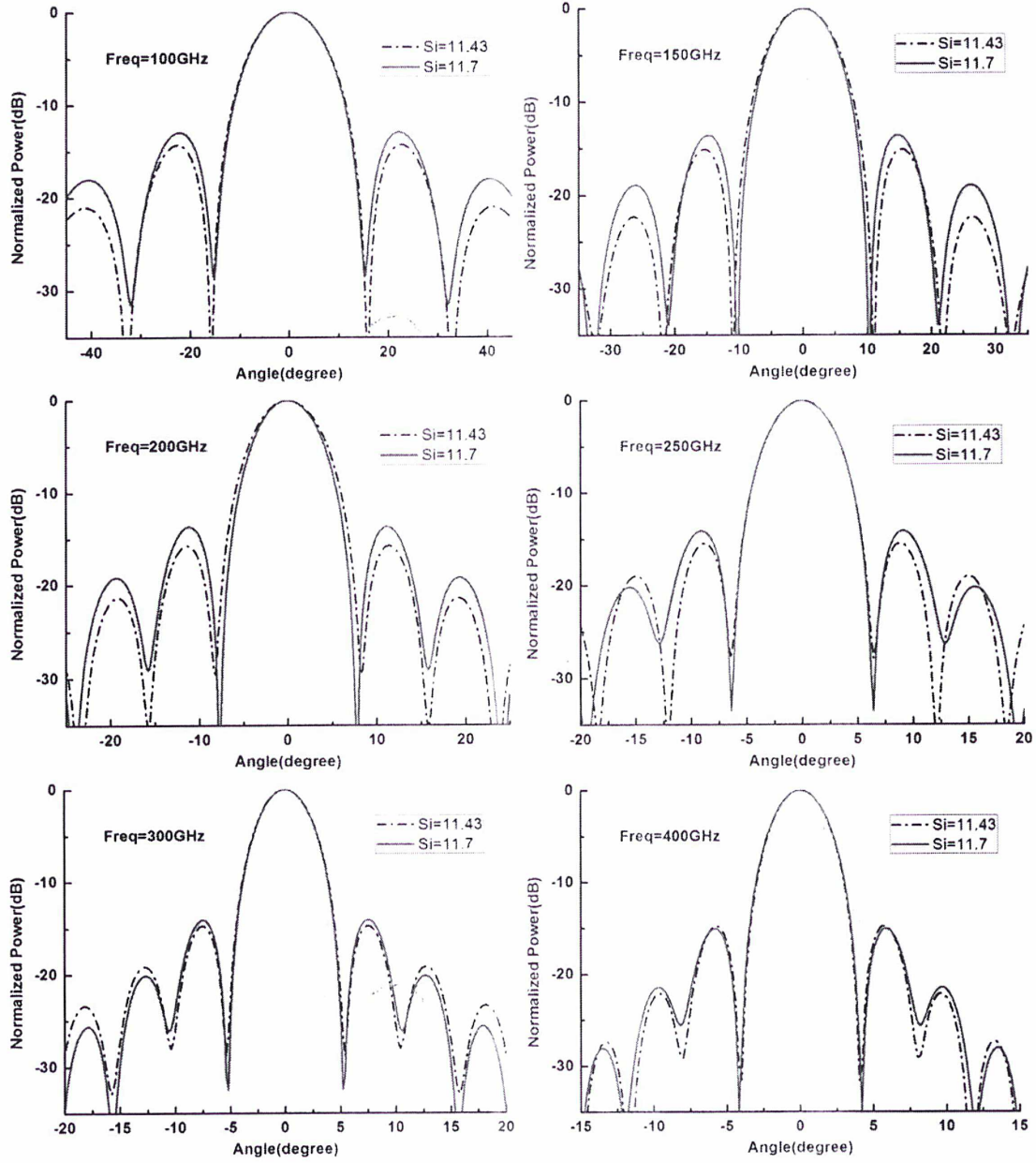


Figure 4.6: Simulated beam patterns of a big lens ($r=6.35$ mm) adopting two silicon permittivities at 100, 150, 200, 250, 300 and 400 GHz.

To demonstrate this conclusion we changed the size of hemispherical lens and simulated again. The radius of hemispherical lens is reduced to 3.175 mm and the extension length is reduced to 1.225 mm. The twin-slot planar antenna keeps the same. The simulated beam patterns are shown in Figure 4.7, and same phenomenon can be observed. The difference between two beam patterns increases from 200 GHz to 400 GHz and then decreases from 400 GHz to 800 GHz. From Figure 4.6 and Figure 4.7 we can also find that this difference is mainly dependent on the ratio (η) of lens's diameter D to free space wavelength λ , it reaches

maximum around $\eta=8.5$ and then reduces to minimum at $\eta=13$.

Finally, we come to the conclusion that the difference of the silicon permittivity at two temperature (77 K and 295 K) does affect the simulated far-field beam pattern of a quasi-optical superconducting HEB mixer. It's desirable to use silicon's permittivity at low temperature in the beam pattern simulation of cryogenic mixers, especially when the ratio of lens's diameter to wavelength (D/λ) is less than 13.

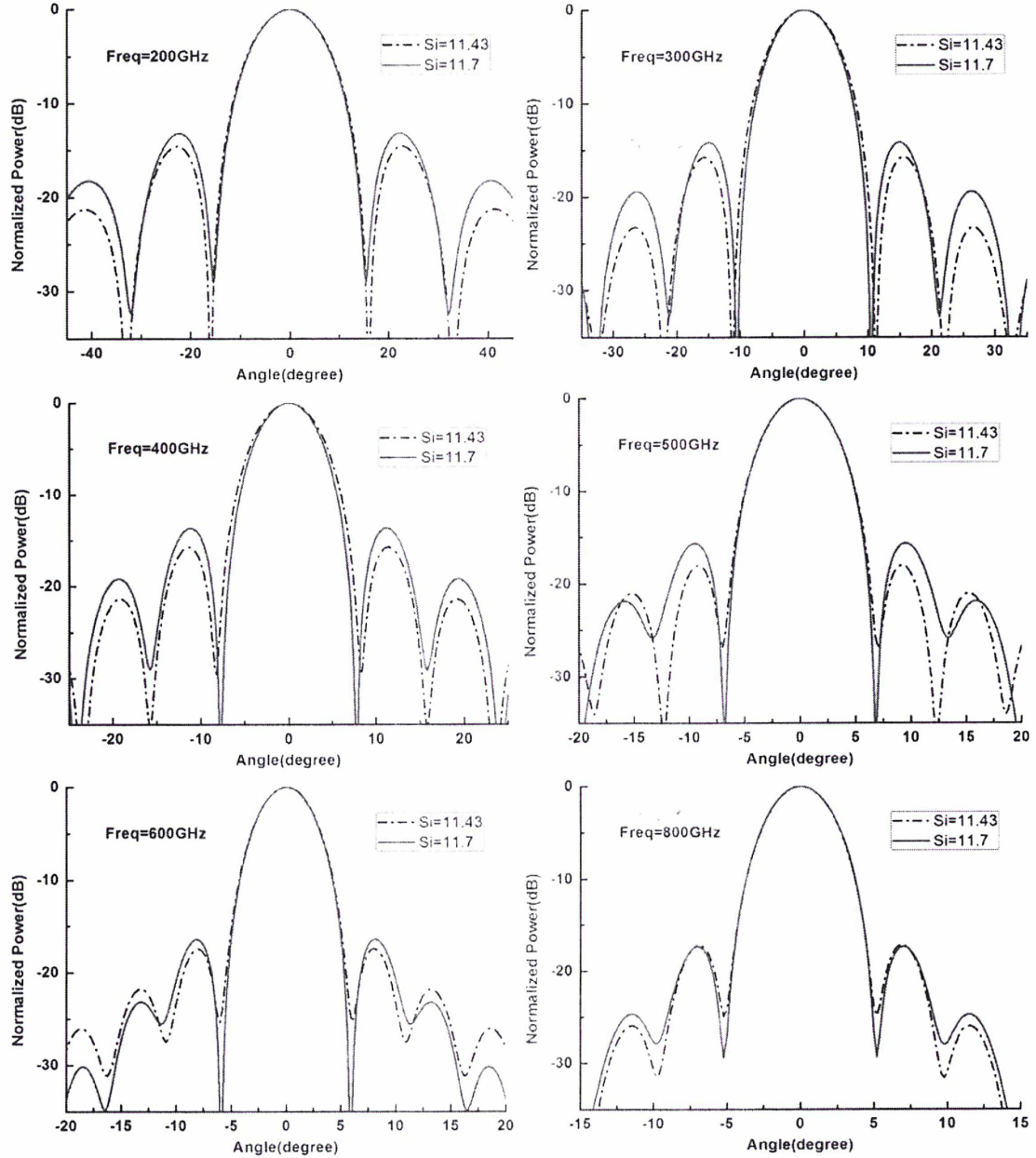


Figure 4.7: Simulated beam patterns of a small lens ($r=3.175$ mm) adopting two silicon permittivities at 200, 300, 400, 500, 600 and 800 GHz.

4.3 Beam pattern measurements of a HEB mixer at 600 GHz

In order to compare with simulations, we measured the beam patterns of a double slot antenna coupled superconducting HEB mixer. Two different measurement systems are employed: the far-field beam pattern by measuring the direct detection behavior of the HEB device; the near-field beam pattern by measuring the mixing behavior of the HEB device, which is then translated to far-field beam pattern by Fourier transformation. Finally, we compared the advantages and disadvantages of two measurement techniques. It should be noted that the operating frequency was chosen at 600 GHz due to the requirement of computer memory in MoM/PO simulation and the RF source number in vector near-field measurement.

4.3.1 Direct far-field beam pattern measurement

4.3.1.1 Measurement system

The experimental setup is shown in the Figure 4.8. A solid state multiplier chain operating at 0.6 THz is applied as a signal source. The superconducting HEB mixer is mounted in a copper block, as shown in Figure 4.9, and then fixed on the 4 K cooling plate of the dewar. The cryostat is placed on a rotation table for angular measurements. The angle resolution of the system is 0.01° . The center of twin-slot antenna is located in the center of the rotation. The distance between the signal source and the detector is 70 cm, which is far enough for far-field measurement. The measured beam pattern of the antenna is therefore expected to be independent of the beam pattern of the signal source. A Labview [13] program is used to control the movement of the rotation motor and the data acquisition. A lock-in amplifier is used to record the current changes due to the modulated incident signal as a function of rotation angle of the cryostat. The dynamic range of this measurement system is about 30 dB.

The 600 GHz double slot antenna coupled superconducting HEB mixer consists of a NbN micro-bridge, a double slot planar antenna and an extended hemispherical lens. The micro-bridge and planar antenna are fabricated on a highly resistive and natively oxidized Si substrate chip with a thickness of 0.4 mm. The twin-slot antenna designed at 0.6 THz has a slot length L of $0.297 \lambda_0$, a slot separation S of $0.158 \lambda_0$ and a slot width W of $0.021 \lambda_0$, with λ_0 the free space wavelength. The extended hemispherical lens has a diameter of 12.7 mm and the extension part of the lens together with the HEB chip substrate yields a total extension length of 2.45mm.

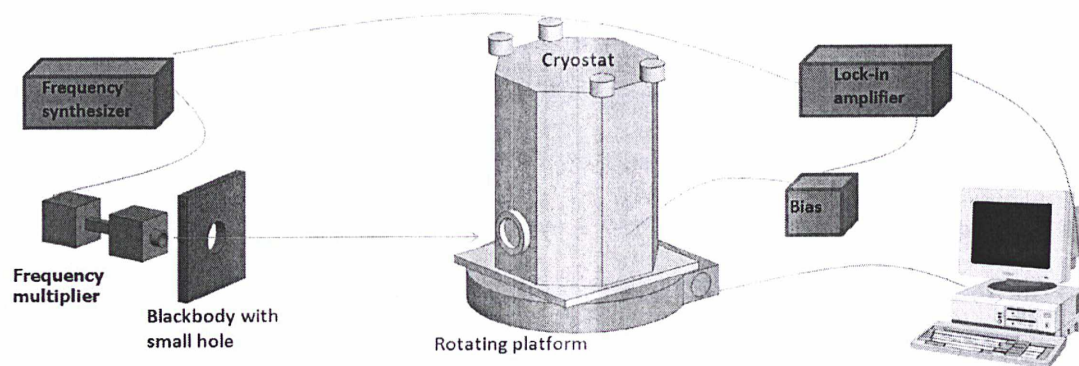


Figure 4.8: Schematic drawing of the measurement setup. The HEB mixer is mounted in a liquid helium cryostat which is placed on a rotation table. The rotation table is controlled by a computer and is synchronous with data acquisition.

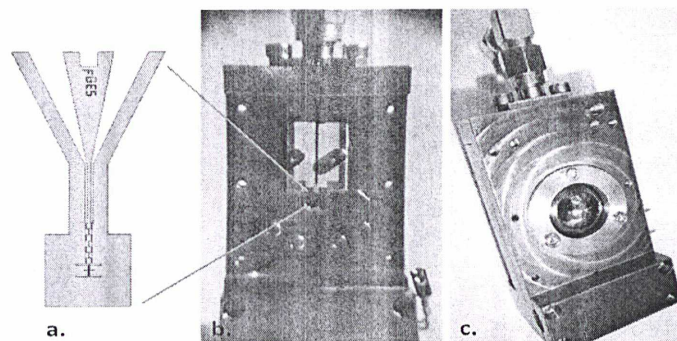


Figure 4.9: Pictures of the,superconducting HEB mixer block.

4.3.1.2 Measurement result

The measured far-field beam-patterns at 600 GHz are shown in Fig. 4.10. The beam-pattern is only measured in H-plane. The measured beam-pattern is symmetric and the full width at half maximum (FWHM) is 2.7° , implying that the beam is well collimated. The side lobes are nearly 18 dB below the main lobe.

For comparison, two simulated beam patterns with different numerical methods (MoM/PO and GO/PO) are also plotted in Fig. 4.10. The result illustrates that the simulation given by MoM/PO method accords better with the measured result than the GO/PO method. It should be noted that the dielectric constant of silicon is set to be 11.43 instead of 11.71 in the simulations and the real structure of the mixer is adopted, as mentioned in Chapter 3.

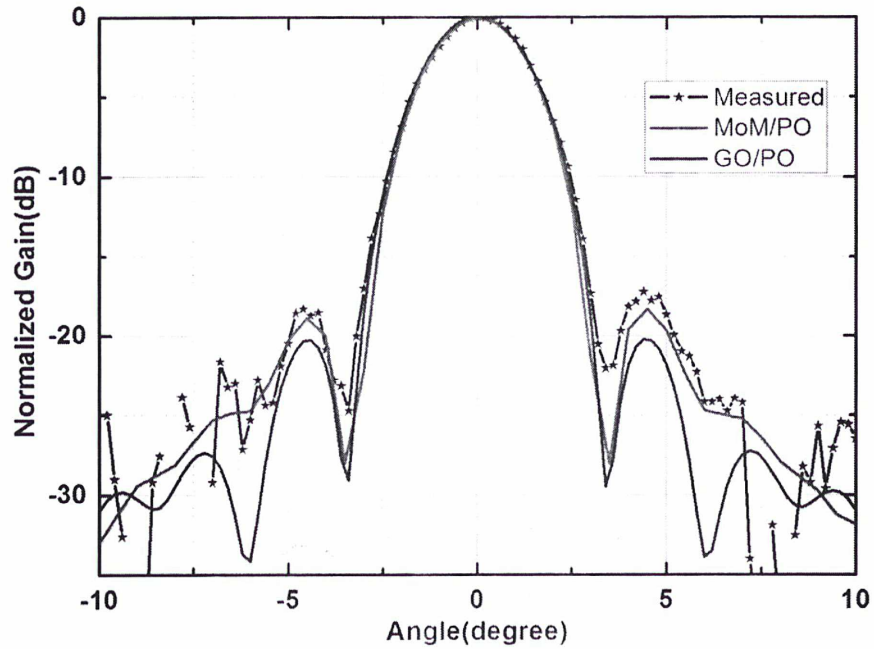


Figure 4.10: Measured and simulated far-field beam-patterns of a superconducting HEB mixer at 600 GHz. Two simulation methods (MoM/PO and PO/GO) have been used.

4.3.2 Vector near-field measurement

Vector near-field measurement is an important technique to characterize electromagnetic radiation properties of antennas and quasi-optical systems. Moreover, a two-dimensional planar map of the vector near field can be utilized to generate the near-field distributions at any other locations in the three-dimensional space, and by means of near-to-far (NTF) transformation [14] the far-field radiation pattern can be obtained in all solid angles. Thus, the information provided by a vector near-field measurement is more complete than direct far-field measurements in the two principle plane cuts. In terms of system setup, near-field measurements is also more compact, and this is especially true for high-frequency antennas with large radiating apertures for which the far-field distance requirement is usually difficult to satisfy.

4.3.2.1 Measurement setup

The schematic of the overall system setup is shown in Figure. 4.11. The system is made up of a test channel and a phase reference channel.

In the test channel, the LO signal at 600 GHz is provided by a frequency synthesizer followed by an amplifier multiplier chain (AMC) with a total multiplication factor of 36, while the RF signal at 599.64 GHz is generated by another AMC with a same total multiplication factor of 36. The RF and LO signals are coupled to the superconducting HEB mixer through a beam-splitter of a 50 μm -thick Mylar film. The 360 MHz IF signal, after proper amplification and filtering, is directly sampled by a high-speed A/D converter (ADC).

The phase reference signal is generated by a millimeter mixer instead of another receiver. The output frequencies of the synthesizers for LO (16.667 GHz) and RF (16.657 GHz) are fed into a Ku-band mixer. The mixing of two signal yields a 10 MHz IF signal, which is used as the phase reference for the test IF signal at 360 MHz.

A raster scan which is 300 mm away from the aperture of HEB mixer and covers an area of $100 \times 100 \text{ mm}^2$ is performed to measure the near-field amplitude and phase distributions.

Meanwhile, both the amplitude and phase fluctuations of the system are measured by periodically (usually every 10 s) sampling a fixed reference position in the scanning area, which helps us to calibrate the shift of mixing gain and phase caused by time.

The measured superconducting HEB mixer is the same one as mentioned in section 4.3.1. Actually, the measured near-field beam-pattern is the convolution of signal source and HEB mixer. Nevertheless, when the beam waist of signal source is much smaller than that of the HEB mixer, the measured beam-pattern is a good approximation to the true near-field distribution of HEB mixer [15].

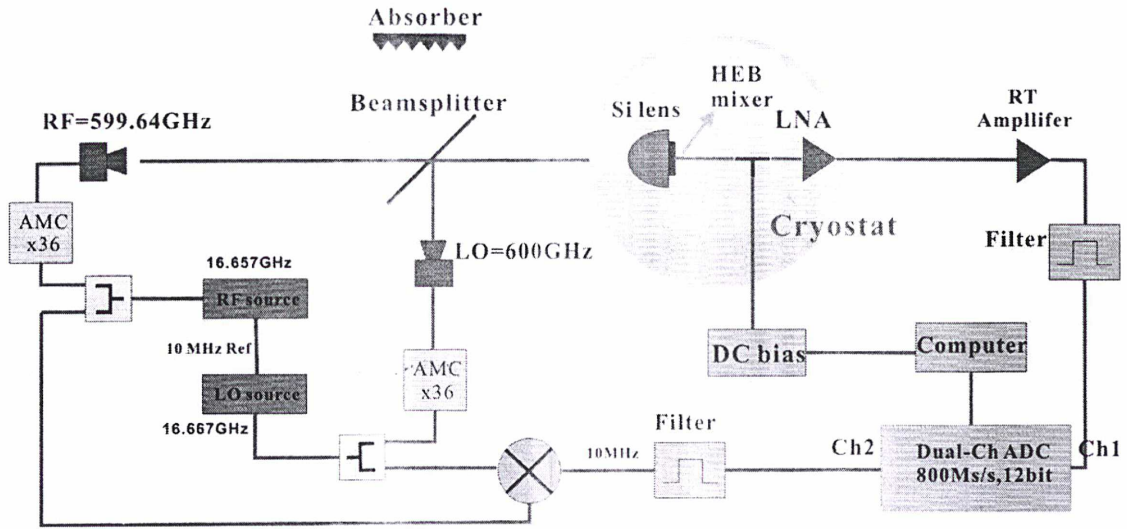


Figure 4.11: Schematic of the system setup.

4.3.2.2 Measurement result

Figure 4.12 illustrates the measured two-dimension amplitude and phase distribution of near-field beam pattern. Obviously the phase spectrum have good symmetry, which indicates that our measurement is reliable. Then by means of near-to-far (NTF) transformation, the far-field radiation pattern can be obtained.

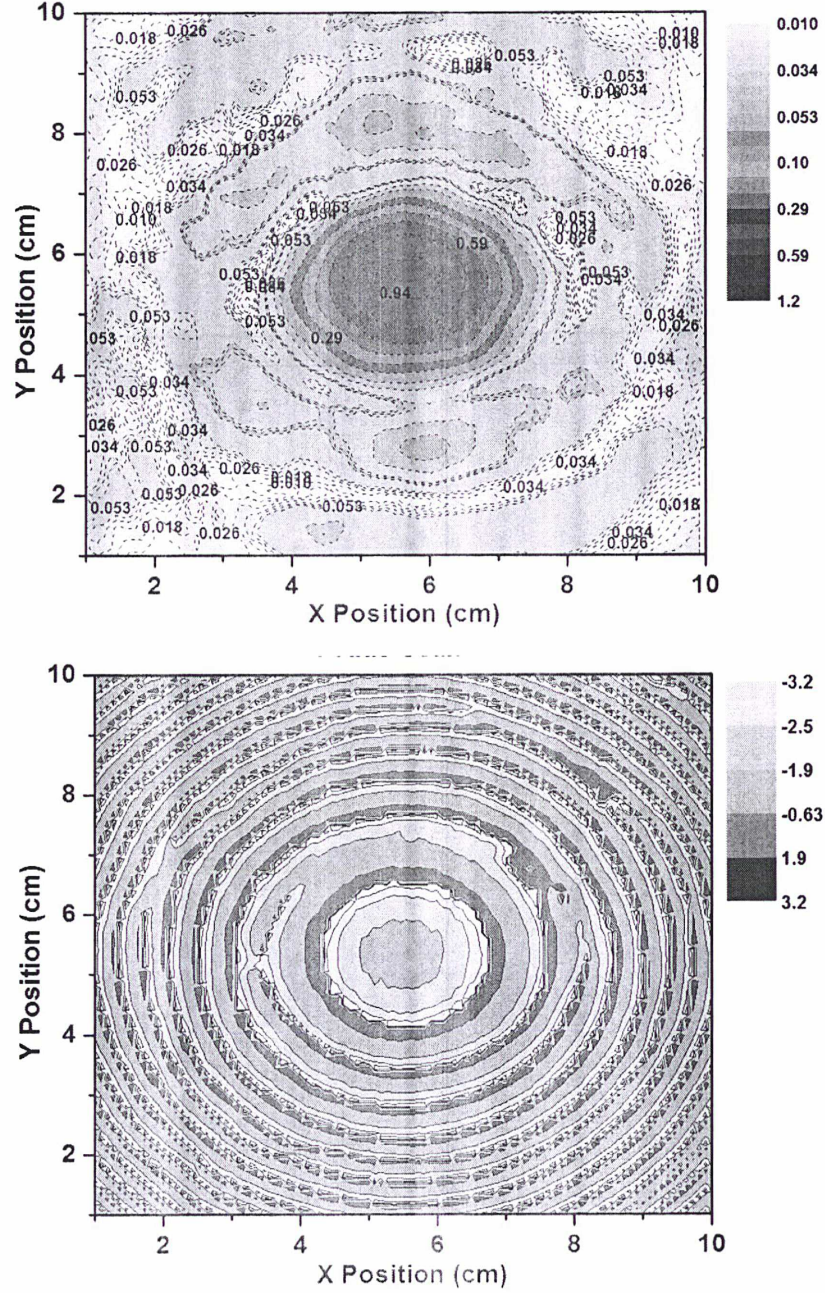


Figure 4.12: Measured near-field amplitude (upper) and phase (lower) spectrums at 600 GHz.

4.3.3 Comparison between near-field and far-field measurement

Figure 4.13 illustrates the comparison between the direct measured far-field beam pattern, the calculated far-field beam pattern by near-to-far (NTF) transformation and the result simulated by MoM/PO method. It is obvious that both main-lobe and first side-lobe of two

measured results accord well with simulation. The far-field beam pattern transformed from near-field measurement has higher signal-to-noise ratio than direct measured one, the second side-lobe can also be observed. However, the near-field vector measurement needs two RF sources and a long measuring time. It takes nearly 2.5 hour to perform a scan of an area of $100 \times 100 \text{ mm}^2$ while the direct far-field beam pattern measurement takes only several minutes to finish the testing and only needs one RF source.

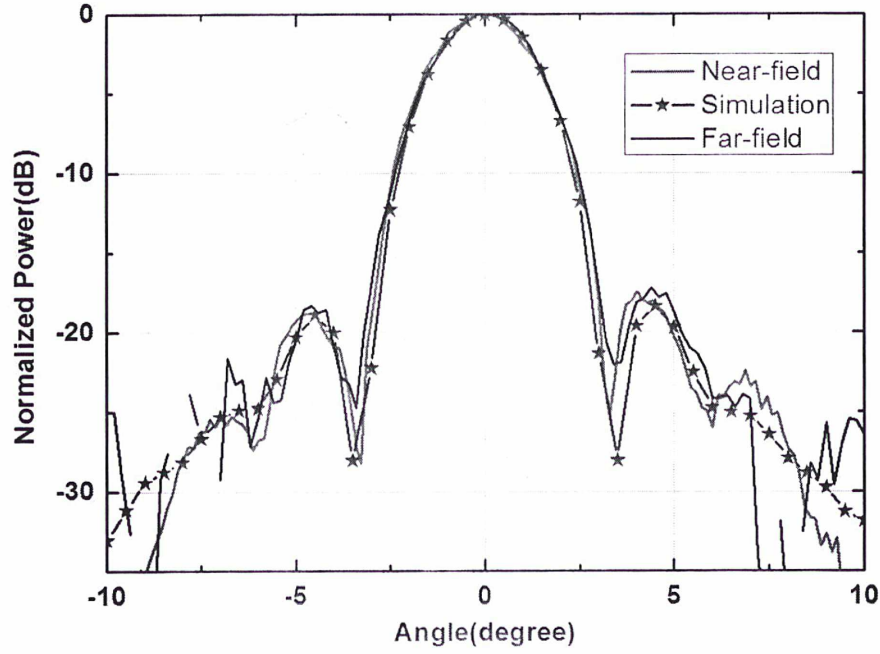


Figure 4.13: Comparison between two measured far-field beam patterns and simulation.

4.4 Effect of HEB bias voltage and bath temperature on far-field beam patterns

Many previous works have investigated the effect of lens and planar antenna on far-field beam-pattern [16, 17], while few works have been done to study the effect of HEB device itself. Therefore, we measured the far-field beam-patterns of a superconducting HEB mixer at different DC bias voltages and bath temperatures, and analyzed their relations. All measurements were performed by direct far-field beam pattern measurement to minimize the

risk of drift over time since it is faster.

Figure 4.14 illustrates the measured far-field beam pattern at different DC bias voltages of the mixer. It is obvious that the profile of beam-patterns does not change with the DC bias voltage while the signal-to-noise ratio (SNR) decreases with the increase of the DC bias voltage. This deterioration can be attributed to the decrease of HEB's sensitivity.

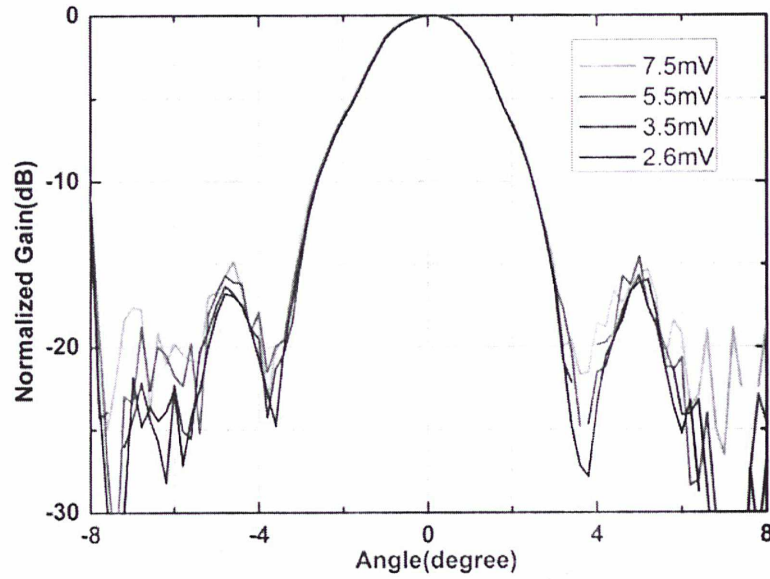


Figure 4.14: Measured far-field beam pattern at different DC bias voltages.

Figure 4.15 illustrates the measured far-field beam pattern at different bath temperature of the mixer. Obviously, the profile of beam-pattern doesn't change with HEB's bath temperature while the signal to noise ratio (SNR) is deteriorated when the bath temperature increases. This deterioration can also be attributed to the decrease of HEB's sensitivity. Many previous works [18, 19] measured far-field beam-pattern by heating HEB to a temperature slightly below the superconducting transition temperature. Our measurements prove that heating is unnecessary since it not only accelerates the consumption of liquid helium (if using liquid helium for cooling) but also decreases the SNR of measured beam-pattern.

In conclusion, both the DC bias and bath temperature don't change the profile of mixer's beam-pattern since the beam-pattern is mainly determined by the dielectric lens. However, they will affect the signal to noise ratio of measured beam-pattern since the direct detection sensitivity is dependent on them.

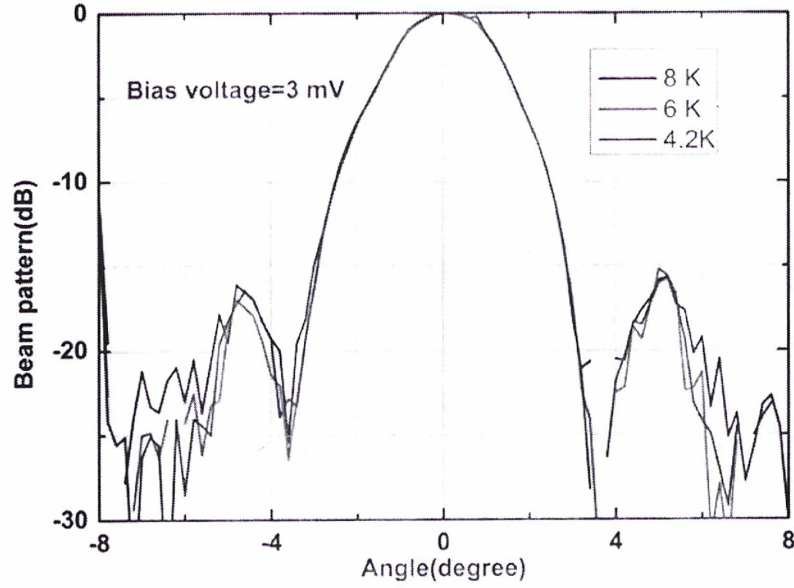


Figure 4.15: Measured far-field beam pattern at different bath temperatures.

4.5 Conclusion

In order to make simulations more close to the reality, we developed a quasi-optical vector test system to measure the silicon permittivity at cryogenic temperature. We found that the difference of silicon permittivity at two temperatures (77 K and 295 K) does affect the simulated far-field beam pattern of a quasi-optical superconducting HEB mixer. So it's desirable to use silicon's permittivity at low temperature in the beam pattern simulation of cryogenic mixers. Then, for getting a better understanding of the beam pattern, we measured the far-field beam patterns of the same superconducting HEB mixer by using a direct far-field measurement and vector near-field measurement system. Both measured results accord well with simulation, while the near-field measured result has higher signal-to-noise ratio. Finally, we investigated the effect of HEB bias voltage and bath temperature on measured far-field beam patterns. Neither DC bias nor bath temperature affected the profile of mixer's beam-pattern, but they affected the signal to noise ratio.

Bibliography

1. V. V. Parshin, R. Heidinger, B. A. Andreev, A. V. Gusev, and V. B. Shmagin, "Silicon as an advanced window material for high power gyrotrons," *Int. J. Infrared Millim. Waves*, vol. 16, no. 5, pp. 863–877, May 1995.
2. E.M. Gershenzon, G.N. Gol'tsman, I.G. Gogidze, A.I. Elant'ev, B.S. Karasik, and A.D. Semenov, "Millimeter and submillimeter range mixer based on electronic heating of superconducting films in the resistive state, " *Soviet Physics Superconductivity*, Vol. 3, pp. 1582-1597, 1990.
3. Sobol, Harold. "Applications of integrated circuit technology to microwave frequencies." *Proceedings of the IEEE*, 59.8 (1971): 1200-1211.
4. Reyes, Adolfo C., et al. "Coplanar waveguides and microwave inductors on silicon substrates." *Microwave Theory and Techniques*, IEEE Transactions on 43.9 (1995): 2016-2022.
5. J. Krupka, J. Breeze, A. Centeno, N. Alford, T. Claussen, and L. Jensen, "Measurements of permittivity, dielectric loss tangent, and resistivity of float-zone silicon at microwave frequencies" *IEEE Transactions on Microwave Theory and Techniques*, 54.11 (2006): 3995-4001.
6. P. GOY, M. Gross, S. Caroopen, J. Mallat, J. Tuovinen, A. Maestrini and M. Martinelli, "Millimeter-Submillimeter Vector Measurements in Free Space, and in Resonant Structures. Application to Dielectrics Characterization" *MRS Proceedings*, Vol. 631. Cambridge University Press, 2000.
7. Goldsmith, F. Paul, Institute of Electrical and Electronics Engineers, and Microwave Theory and Techniques Society. "Quasioptical systems: Gaussian beam quasioptical propagation and applications" *New York: IEEE press*, 1998.
8. J. W. Lamb, "Miscellaneous data on materials for millimetre and submillimetre optics." *International Journal of Infrared and Millimeter Waves* 17.12 (1996): 1997-2034.
9. Afsar, Mohamed Nurul, and Hua Chi. "Millimeter wave complex refractive index, complex dielectric permittivity and loss tangent of extra high purity and compensated silicon" *International journal of infrared and millimeter waves* 15.7 (1994): 1181-1188.
10. A. D. Semenov, H. Richter, H.-W. Hübers, B. Gunther, A. Smirnov, K. S. Il'in, M. Siegel, and J. P. Karamarkovic, "Terahertz performance of integrated lens antennas with a

- hot-electron bolometer” *IEEE Transactions on Microwave Theory and Techniques*, 55.2 (2007): 239-247.
11. M. Hajenius, J. J. A. Baselmans, A. Baryshev, J. R. Gao, T. M. Klapwijk, J. W. Kooi, W. Jellema, and Z. Q. Yang, “Full characterization and analysis of a THz heterodyne receiver based on a NbN hot electron bolometer,” *J. Appl. Phys*, vol. 100, p. 074507, 2006.
 12. W. Zhang, P. Khosropanah, J. R. Gao, T. Bansal, T. M. Klapwijk, W. Miao, and S. C. Shi, “Noise temperature and beam pattern of an NbN hot electron bolometer mixer at 5.25 THz,” *Journal of Applied Physics*, vol. 108, p. 093102, Nov 2010.
 13. <http://www.ni.com/labview>
 14. A. D. Yaghjw, “An overview of near-field antenna measurements,” *IEEE Trans. Antennas Propag.* **34**(1), 30–45 (1986)
 15. Z. Lou, J. Hu, K. M. Zhou, W. Miao, S. C. Shi, “A quasi-optical vector near-field measurement system at terahertz band,” *Review of Scientific Instrument*, Vol. 85, p. 064702, 2014.
 16. D.F. Filipovic, S.S. Gearhart, G.M. Rebeiz, “Double-Slot Antennas on Extended Hemispherical and Elliptical Silicon Dielectric Lenses,” *IEEE Transactions on Microwave Theory and Techniques*, Vol. 41, No. 10, pp. 1738-1749, 1993.
 17. Boriskin, A. V., Godi, G., Sauleau, R., & Nosich, A. I, “Small hemielliptic dielectric lens antenna analysis in 2-D: boundary integral equations versus geometrical and physical optics,” *Antennas and Propagation, IEEE Transactions on*, 56(2), 485-492, 2008.
 18. W. Zhang, J.R. Gao, M. Hajenius, W. Miao, P. Khosropanah, T. Klapwijk, and S.C. Shi. “Twin-slot antenna coupled NbN hot electron bolometer mixer at 2.5 THz,” *IEEE Trans on terahertz science and technology*, vol. 1, no. 2, (2011).
 19. H.-W. Hüber, A. D. Semenov, H. Richter, J. Schubert, S. Hadjiloucas, J.W. Bowen, G. N. Goltsman, B. M. Voronov, and E. M. Gershenzon, “Antenna Pattern of the Quasi-Optical Hot-Electron Bolometric Mixer at THz Frequencies,” *Proceedings of 12th International Symposium on Space Terahertz Technology*, pp. 286–296, (2001).

Chapter 5

Investigation of a 1.4-THz Quasi-optical HEB Mixer

Dome A, with an altitude of 4093 m, is presumably the most promising ground-based observing site for THz astronomy [1, 2]. Purple Mountain Observatory is planning to build a 5 m terahertz telescope (DATE5) there, with one important band centered at around 1.4 THz which is a frequency band where there is an abundance of molecular spectral lines and fine atomic structure spectral lines (e.g., high-J CO, H₂D⁺ and NII). In this chapter, we present in detail the design, fabrication, and characterization of a 1.4-THz quasi-optical superconducting HEB mixer integrated with a double slot antenna.

5.1 Mixer design

The 1.4-THz superconducting HEB mixer consists of a NbN microbridge, a twin-slot antenna and an elliptical lens. The NbN microbridge of 2 μm wide, 0.2 μm long and 3.5 nm thick is fabricated on a highly resistive and natively oxidized Si substrate. As shown in the upper plot of Figure 5.1, the microbridge is connected to the central conductor of a coplanar waveguide (CPW) transmission line by two Ti/Au contact pads. The CPW line couples radio frequency (RF) and local oscillator (LO) radiation from the twin-slot antenna to the NbN microbridge. The twin-slot antenna has a slot length L of 0.067 mm, a slot separation S of 0.03819 mm and a slot width W of 0.005 mm. A RF choke filter with three alternating high- and low-impedance quarter wavelength segments is adopted to prevent RF and LO radiation from leaking to the mixer's intermediate frequency (IF) output. The superconducting HEB device chip, fabricated on a 0.4 mm thick Si substrate, is mounted on the flat surface of an elliptical lens. The elliptical lens is an ellipsoid cut off at a plane perpendicular to its major

axis, with a major axis length of 5.228 mm and a minor axis length of 5 mm. The extension length of the elliptical lens is 1.149 mm, the structure of the lens is shown in the lower plot of Figure 5.1.

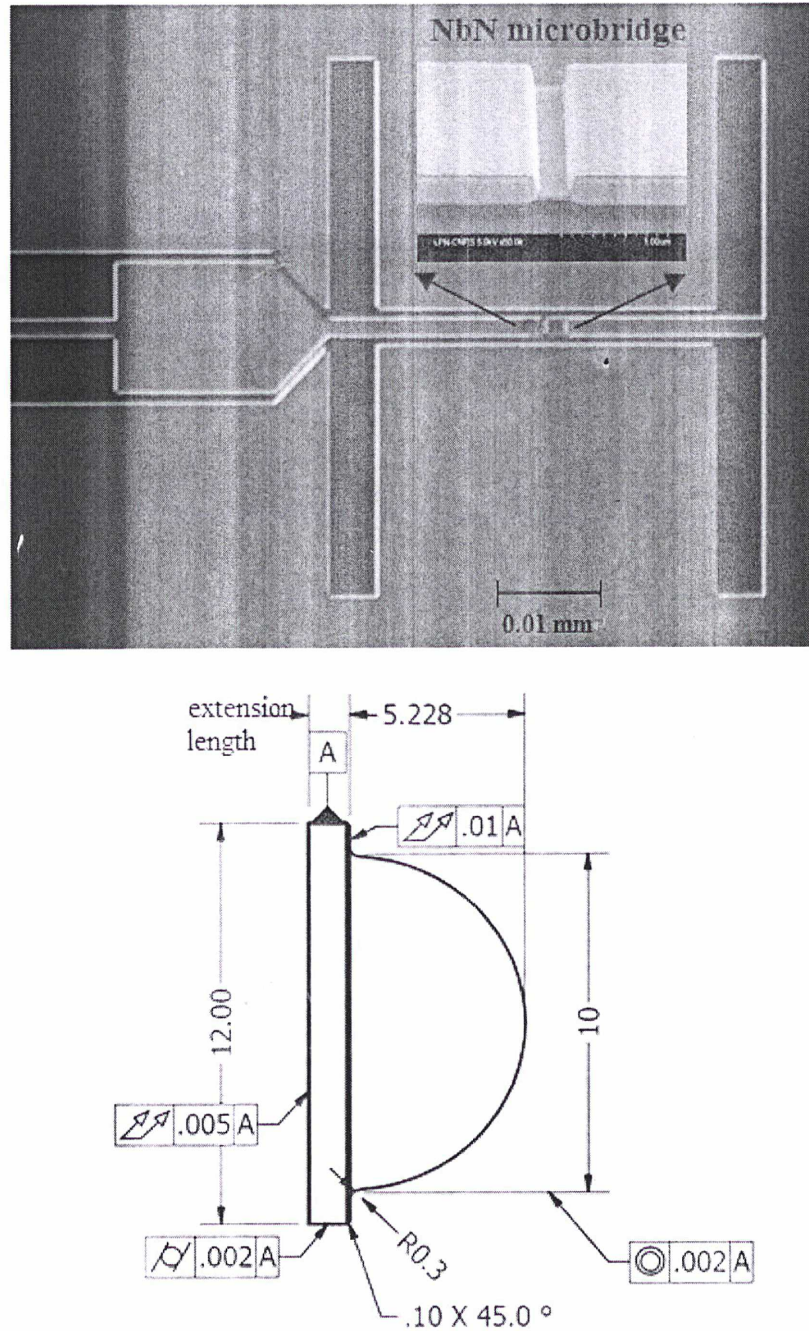


Figure 5.1: SEM picture of the planar antenna and a close-up view of the HEB device (upper) and schematic structure of the Si elliptical lens (lower).

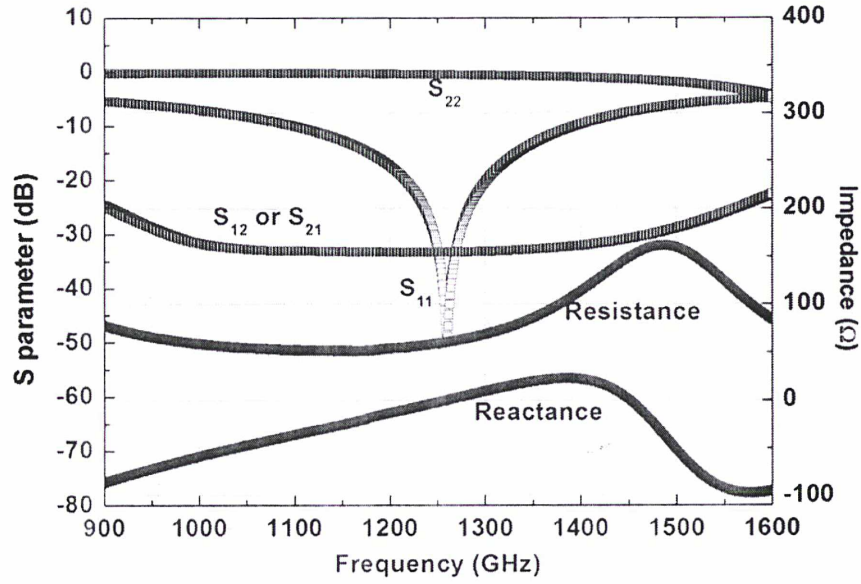


Figure 5.2: Simulated S parameter and resistance of the double slot antenna.

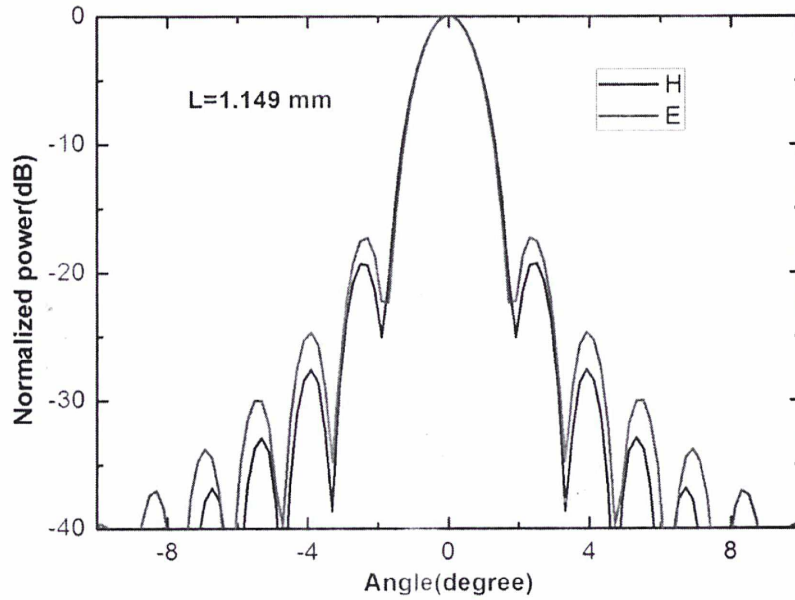


Figure 5.3: Simulated E-plane and H-plane far-field beam pattern at 1.4 THz.

Figure 5.2 illustrates the simulated resistance, reactance and S parameters of the double slot planar antenna by HFSS. Figure 5.3 illustrates the simulated far-field beam-pattern of the superconducting HEB mixer at 1.4 THz. The beam pattern has good symmetry in both E-plane and H-plane, the full widths of main lobe at -3 dB level is 3.4° and the side lobes are 17 dB below the main lobe.

5.2 Device fabrication

The fabrication of superconducting HEB device includes superconducting film and planar antenna. The key element for a HEB device is an ultrathin superconducting film that is typically with a thickness of several nm. The thin superconducting film used in this thesis is made of niobium nitride and is provided by Moscow State Pedagogical University (MSPU). It is deposited by DC reactive magnetron sputtering [3] that is the commonly used method for the deposition of high quality superconducting films on substrate. In this sputtering process, an argon ions gas, generated by a glow discharge, is feed into the vacuum chamber. The ions are accelerated by a DC voltage of some hundred Volts to a target consisting of the material to be deposited. The material is ejected isotropically from the surface of the target due to the momentum exchanges between the bombarding ions and the surface atoms. The nitrogen gas is also feed into the sputter chamber to react with the target material. After fabricating the superconducting film, the HEB electrodes, the antenna and the bonding pads can be patterned by electron beam (e-beam) lithography, deposition of metals, and lift-off.

The 1.3 THz superconducting HEB device was fabricated at LERMA by R. Lefevre. Unlike conventional processes adopting an additional superconducting interlayer to improve the contact quality, we deposit the Au contact pad directly on the NbN film after an in-situ cleaning. Moreover, only one Au layer was used to make the contact and antenna structure instead of two Au layers which represent the standard configuration in most of reported HEB fabrication process [4]. The contact resistance close to the HEB microbridge is then reduced.

Figure 5.4 shows a scheme of the main steps of the HEB fabrication process. The detail is as follow:

1. Deposition of a thin NbN superconducting film by DC reactive magnetron sputtering at MSPU. The typical thickness of the NbN film is around 3.5 nm.
2. Patterning the HEB electrodes, the antenna and the bonding pads at the same time by electron beam (e-beam) lithography, deposition of metals, and lift-off. For the deposition of metals, the sample was firstly cleaned *in situ* by ion beam etching with argon. Then we deposited 5 nm of Ti as adhesion layer followed by 200 nm of Au. Afterwards, we

removed the resist with trichloroethylene and rinsed the sample in two baths of acetone. In this step the length of the HEB was defined by the gap between its electrodes ranging from 100 to 200 nm.

3. Patterning a rectangle mask across the two HEB electrodes. The width of the bolometer (usually 2 μm) was defined at this stage.
4. Removing the unprotected NbN film, by reactive ion etching with SF_6 . An over-etching has been done to be sure that the unprotected NbN was completely removed
5. Removing the Ni mask which short-circuits the HEB electrodes. This was done by wet etching with nitric acid at 69 % for 6 min. Then the sample was rinsed with deionized water.
6. Covering the sample with a 10 nm thick SiN passivation layer to protect the devices from the ambient atmosphere. This was performed by plasma enhanced chemical vapor deposition at 280 $^{\circ}\text{C}$.

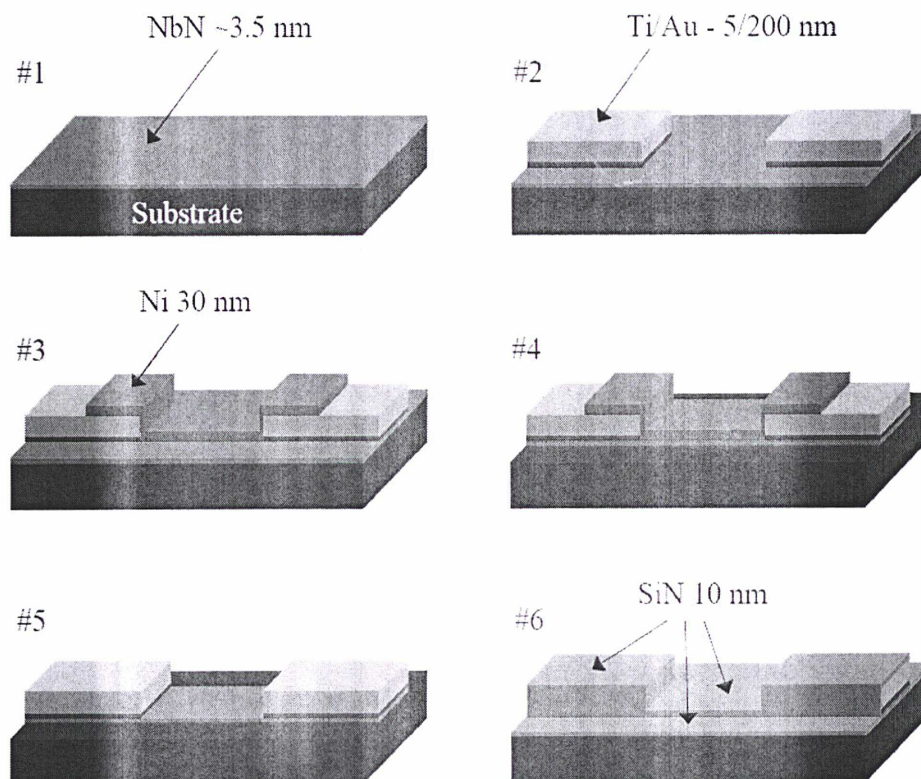


Figure 5.4: Scheme of the main steps of the HEB fabrication process [4].

5.3 DC characteristic

The measured I - V curve and R - T curve of this superconducting HEB mixer are shown in Figure 5.5. The critical current is nearly 250 μA . Two superconducting transitions can be observed at 5 K and 9.5 K, respectively, with the lower one due to the proximity effect at the NbN-Au interface [5] and the higher one due to the NbN microbridge itself. The normal state resistance is about 67.4 Ω .

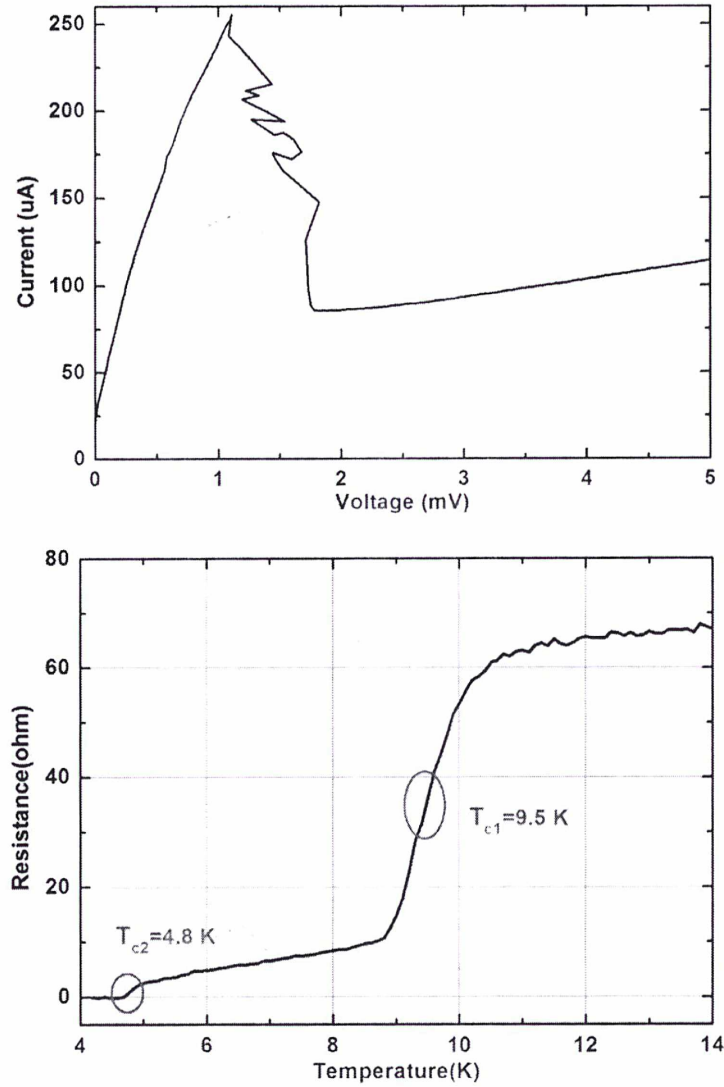


Figure 5.5: Measured I - V curve (upper) and R - T curve (lower) of the 1.4-THz superconducting HEB mixer.

5.4 Receiver noise temperature and IF bandwidth

5.4.1 Receiver noise temperature and analysis

The receiver noise temperature is usually used to characterize the noise performance of a receiver system. The common way to determine the equivalent noise temperature is the Y-factor method, in which the output powers of the receiver in a certain bandwidth Δf are compared when the system's input port is connected to a hot load and a cold load. In our measurement, the hot load and cold are 295 K and 77 K blackbody load respectively.

The Y-factor is defined as:

$$Y = \frac{P_{out,hot}}{P_{out,cold}} = \frac{P_{hot-load} + P_{receiver}}{P_{cold-load} + P_{receiver}} \quad (5.1)$$

where $P_{out,hot}$ and $P_{out,cold}$ are the receiver output powers with respect to the hot and cold blackbody loads, $P_{receiver}$ is the noise power of receiver itself.

According to Planck's law [6], the thermal power emitted in the bandwidth Δf from the blackbody at a temperature T is given by:

$$P(T, f) = \frac{hf}{e^{\frac{hf}{k_B T}} - 1} \Delta f \quad (5.2)$$

where $h = 6.626 \cdot 10^{-34} \text{ J}\cdot\text{s}$ and $k_B = 1.38 \cdot 10^{-23} \text{ J/K}$ are the Planck's and Boltzmann's constant respectively. In the limit of small $hf / k_B T$, the Planck's law can be approximated to Rayleigh-Jeans limit:

$$P(T, f) \approx k_B T \Delta f \quad (5.3)$$

Then Eq. 5.1 can be written as:

$$Y = \frac{P_{out,hot}}{P_{out,cold}} = \frac{Gk_B T_{hot} \Delta f + Gk_B T_{rec} \Delta f}{Gk_B T_{cold} \Delta f + Gk_B T_{rec} \Delta f} = \frac{T_{hot} + T_{rec}}{T_{cold} + T_{rec}} \quad (5.4)$$

where G and T_{rec} are the gain and equivalent noise temperature of the receiver, respectively.

From this equation, the receiver noise temperature can be determined:

$$T_{rec} = \frac{T_{hot} - Y \cdot T_{cold}}{Y - 1} \quad (5.5)$$

It should be noted that the approximation given by the Rayleigh-Jeans limit is no longer valid when the frequency is sufficiently high or the temperature is sufficiently low. In this case the equivalent blackbody radiation temperature is determined by the Callen-Welton radiation law:

$$T_{C-W} = T \frac{\frac{hf}{k_B T}}{e^{\frac{hf}{k_B T}} - 1} + \frac{hf}{2k_B} \quad (5.6)$$

For a cascade system composed of multiple amplifiers, the equivalent noise temperature of the whole system can be given by:

$$T_{total} = T_1 + \frac{T_2}{G_1} + \frac{T_3}{G_1 G_2} + \dots \quad (5.7)$$

Therefore, for the superconducting HEB mixer, the measured receiver noise temperature by Y-factor consists of three parts: RF noise T_{RF} , mixer noise T_{mixer} and IF noise T_{IF} . It can be expressed as:

$$T_{rec} = T_{RF} + \frac{T_{mixer}}{G_{RF}} + \frac{T_{IF}}{G_{RF} G_{mixer}} \quad (5.8)$$

The measurement setup is illustrated in Figure 5.6. The LO source is a solid state multiplier chain operating at 1.3 THz. The beam from the LO source is collimated by an objective Teflon lens, and then coupled into the cryostat through a 12.5 μm Mylar beam splitter. The cryostat has a 2 mm thick high-density polyethylene (HDPE) window and a Zitex G104 infrared filter. The mixer intermediate frequency (IF) output signal goes through a bias-tee and an isolator, and is then amplified by a cryogenically cooled low-noise amplifier (LNA) of 35 dB gain and a room temperature amplifier of 40 dB gain. The IF output signal is filtered at 1.5 GHz within a bandwidth of 80 MHz and recorded by a square-law detector.

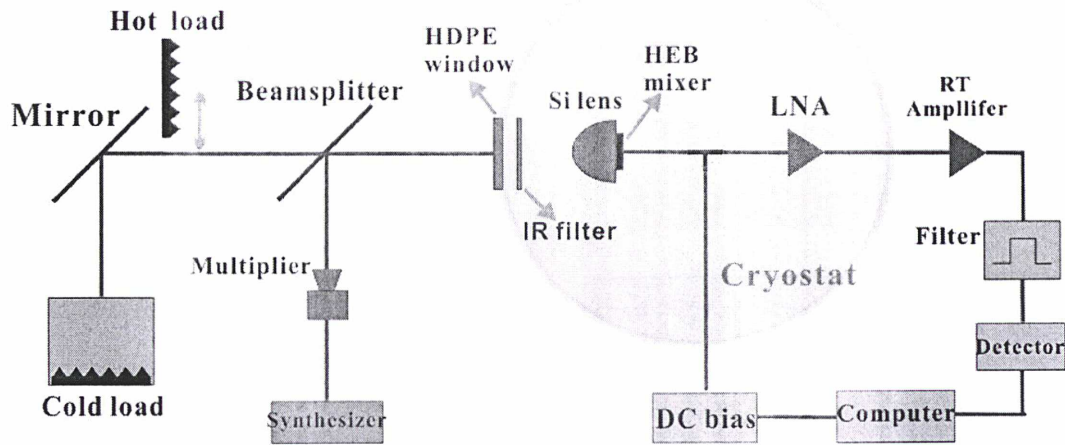


Figure 5.6: Schematic of the noise temperature measurement setup.

Figure 5.7 shows the I-V curves of the HEB mixer with different LO powers, the optimal region for noise temperature measurement is also marked.

Figure 5.8 shows the measured receiver noise temperature and the corresponding receiver IF output powers of 295 K and 77 K blackbody as a function of the HEB dc-bias voltage. Note that the temperatures of the hot and cold blackbody were calibrated to the effective radiation temperatures of 296 K and 81 K at 1.3 THz in terms of the Callen-Welton definition. In addition, the direct detection effect was compensated by adjusting the LO power [7] to make the IV curves unchanged between the hot- and cold-load measurement. The bias current changed 1 μ A due to the direct detection effect at the operating point. The absorbed LO power owing for adjusting is about 2 nW. It can be seen clearly that the measured lowest DSB receiver noise temperature is about 600 K, which is indeed a state of the art result, at a bias voltage of 0.4 mV and at a bath temperature of 4 K. The low optimal bias voltage can be attributed to the very small residual resistance.

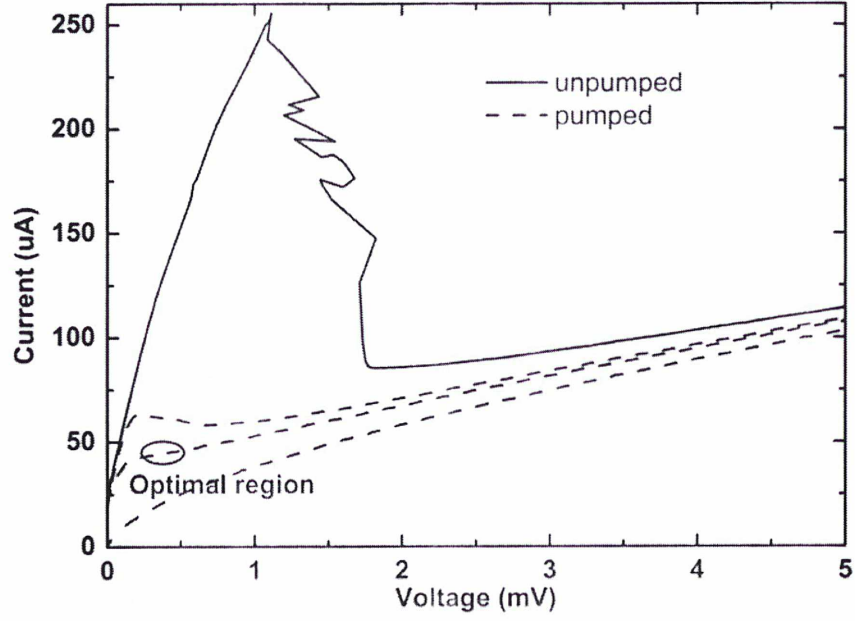


Figure 5.7: *I-V* curves of the HEB mixer with different LO powers, the optimal region is also plotted.

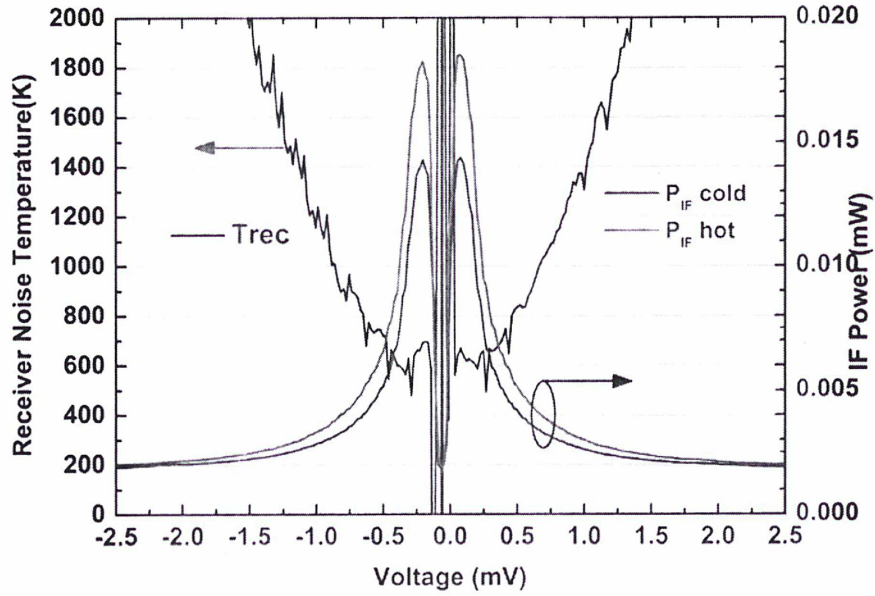


Figure 5.8: Measured receiver IF output power (right axis) for the hot-and cold-load at an optimal LO power and the corresponding DSB receiver noise temperature (left axis), shown as a function of the mixer dc-bias voltage.

The measured receiver noise temperature in the previous section includes RF noise T_{RF} , intrinsic noise of HEB device T_{mixer} and IF noise T_{IF} . Therefore, the estimation of RF noise and IF noise is very important for understanding the intrinsic noise behavior of HEB device

itself.

a) RF noise

Figure 5.10 shows the quasi-optical and electrical components in the signal path. The RF optics of the receiver system consists of a 12.5 μ m Mylar beam-splitter, positioned under an angle of 45°, a 2 mm HDPE vacuum window, a Zitex G104 IR filter, and the integrated lens antenna without anti-reflection coating. Note that the IF gain is not included in G_{total} .

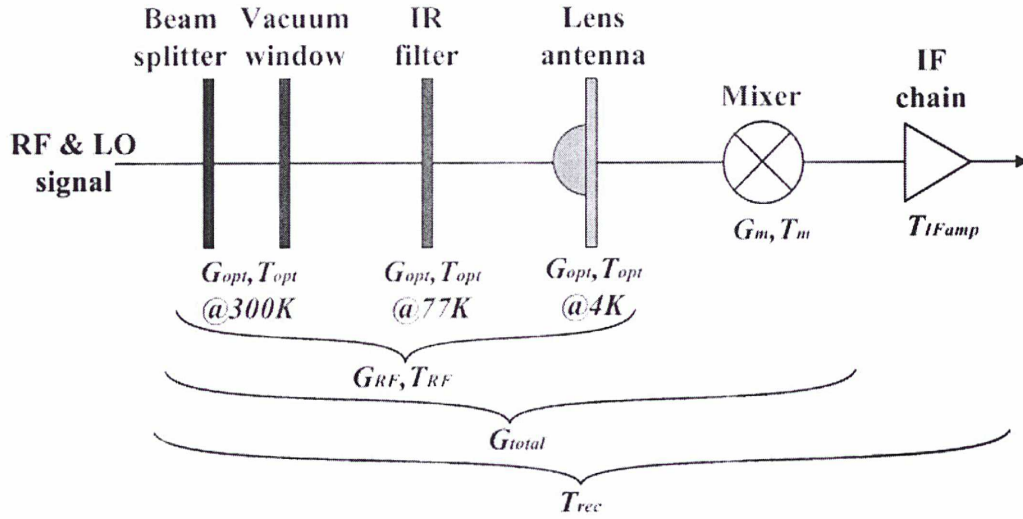


Figure 5.9: Gain and noise temperature of quasi-optical and electrical components in the signal path.

In order to evaluate G_{RF} and T_{RF} , each RF component should be separately considered because the RF components are at different temperatures, and they add an additional amount of blackbody power (noise) depending on their physical temperature. Then the equivalent input noise temperature T_{eq} of each RF component with a gain G is given by:

$$T_{eq} = T_{C-W}(T) \frac{1-G}{G} \quad (5.9)$$

According to Callen-Welton radiation law, $T_{C-W}(T)$ is related as stated in Eq. 5.6.

Using Eq. 5.9, we calculated the equivalent noise temperature and gain of each RF component at 1.3 THz. The calculated results are listed in Table 5.1. The gain of the 12.5 μ m Mylar beam-splitter is -0.97 dB (calculated from the transmittance shown in Figure 5.11) and the equivalent noise temperature is 75.25 K. The total gain of RF part of the receiver is -3.35

dB, and the equivalent noise temperature T_{RF} calculated from Eq. 5.7 is 152.78 K.

Table 5.1

GAINS AND NOISE TEMPERATURES OF THE QUASI-OPTICAL COMPONENTS AT 1.3 THz

	<i>Gain (dB)</i>	<i>Physical Twmp(K)</i>	<i>Callen-Welton Temp (K)</i>	<i>Noise Temp (K)</i>
Beam splitter	-0.97	300	301.0	75.25
Vacuum Windows	-0.56	300	301.0	41.05
Zitex G104	-0.22	77	80.9	4.26
Lens reflection	-1.5	4	30.3	12.49
Lens absorbtion	-0.1	4	30.3	0.7
Total	-3.35			152.78

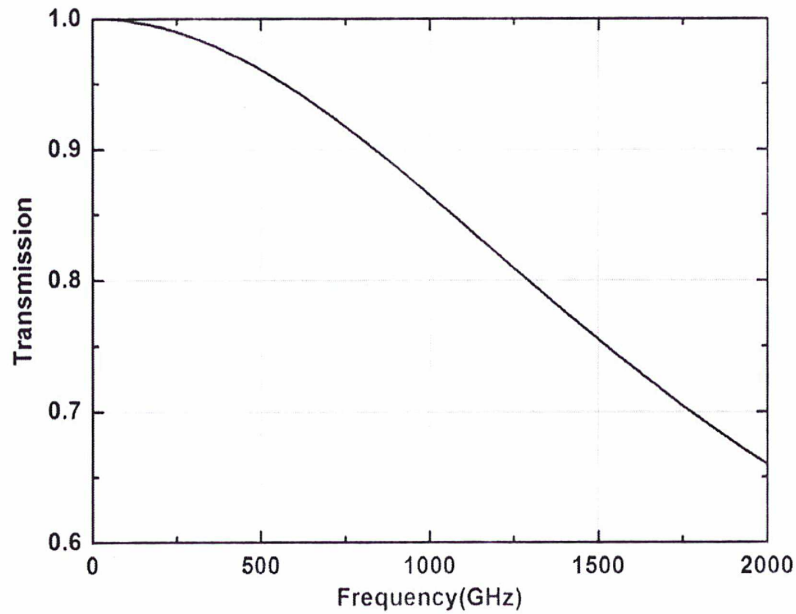


Figure 5.10: Transmission of a 12.5 μm Mylar beam-splitter in the frequency range from 0.1 to 2000 GHz

In addition, we measured the RF noise of the superconducting HEB mixer by a method developed by W. Miao [8]. The measurement setup is the same as the one for noise temperature measurement. At a constant bias voltage (e.g., at 1 mV), we simultaneously

recorded the bias current and the IF output power of the HEB receiver when the HEB mixer is slowly heated to its normal state. The IF output power of the HEB receiver needs to be accurately determined for two different input radiation temperatures (77 K and 300 K). Then we extracted the IF output power of the HEB receiver from the polynomial fitting of the measured IF output power versus the HEB bias current (P - I) curves, as shown in Figure 5. 11. According to this plot, the measured receiver IF output power versus input radiation temperature (P - T) curves for different bias current can be obtained. It should be noted that the mixer output noise decreases when the bath temperature of HEB mixer increases in the measurement. We can estimate the effect of the decrease of the mixer output noise on the IF

output power by $\frac{\Delta T_{out} P_{out}}{G_{RF} G_m (T_{rec} + T)}$, where ΔT_{out} is the variation of the mixer output noise

and can be calculated from hot spot model. Figure 5.12 shows the measured receiver IF output power versus input radiation temperature (P - T) curves after correcting this effect. The cross point of the IF-output-power lines is the measured RF noise temperature value. Apparently, it can be seen that the input RF noise temperature of the HEB receiver is about 145 K, which is very close to the calculated RF noise result of 152 K.

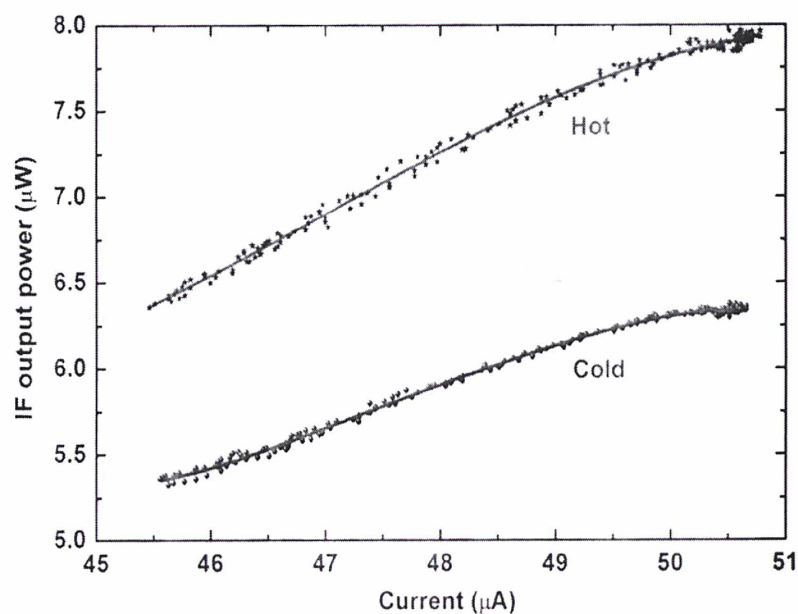


Figure 5.11: The measured and fitted IF output power versus the HEB bias current (P - I).

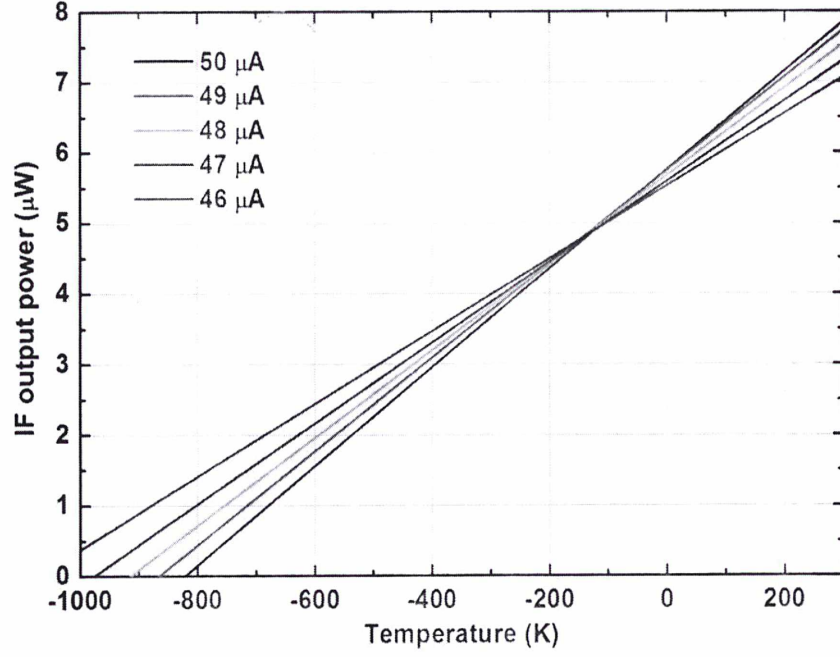


Figure 5.12: Measured receiver IF output power versus input radiation temperature (P - T) curves after correcting the effect of the decrease of mixer output noise on the receiver IF output power.

b) Antireflection coating

From the analysis of noise temperature and gain of each RF component in a quasi-optical system, we can find that the reflection loss of Si lens occupies near 50% of the total RF loss. This reflection loss is caused by the mismatching of dielectric constant between silicon and free space and can be eliminated by coating an antireflection film on the surface of the Si lens.

The reflectivity of the electromagnetic wave on the lens surface can be given by:

$$\Gamma^2 = \left(\frac{n-1}{n+1} \right)^2 \quad (5.10)$$

where n is the refractive index of Si. When $n=11.43$, the reflectance is about 30%. A 1/4 wavelength impedance transformer can be used to eliminate the reflection. The impedance transformer is a dielectric film with a dielectric constant of $\epsilon = \sqrt{\epsilon_{Si}}$ and a thickness of 1/4 wavelength. In this work, we chose Parylene C film with a thickness of 35.5 μm to be the impedance transformer.

According to Eq. 5.8, the receiver noise temperature can be rewritten as:

$$T_{rec} = T_{RF} + \frac{1}{G_{RF}} \left(T_{mixer} + \frac{T_{IF}}{G_{mixer}} \right) \quad (5.11)$$

Substituting RF loss, RF noise temperature (without anti-reflection coating) and the measured receiver noise temperature T_{rec} into Eq. 5.11, we can get $T_{mixer} + \frac{T_{IF}}{G_{mixer}} = 207 K$.

When the Si lens has an anti-reflection coating film, its reflection loss becomes 0 dB, therefore the new RF loss becomes -1.85 dB and the RF noise temperature becomes 133.7 K. Substituting them into Eq. 5.11, we can estimate the equivalent receiver noise temperature with an anti-reflection coating film is $T_{rec} = 450 K$, the anti-reflection coating can reduce the noise temperature of 150 K.

In addition, we measured the receiver noise temperature of this 1.4-THz superconducting HEB mixer with an anti-reflection coating on the lens. As shown in Figure 5.13, the measured noise temperature is 450 K, which accords well with calculated result.

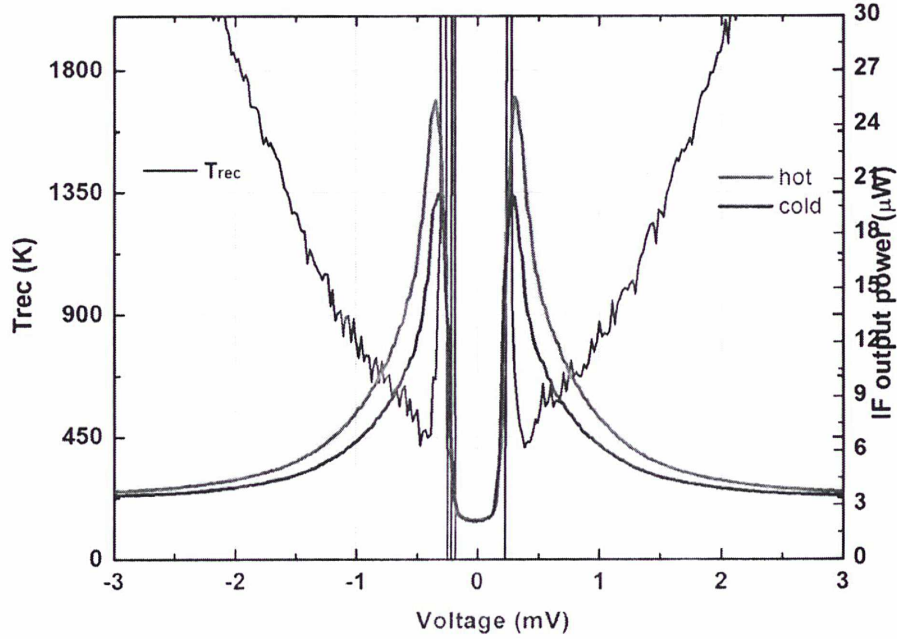


Figure 5.13: Measured receiver equivalent noise temperature of the 1.4-THz superconducting HEB mixer with an anti-reflection coating.

c) IF noise and conversion gain

After studying the RF noise and gain, we also need to know the IF noise temperature T_{IF} and conversion gain of the receiver system G_{total} .

The HEB mixer is heated to its normal state when measuring the IF noise temperature. Therefore, the HEB device is as a resistance and the gain of the mixer G_m is zero. Then the IF output power can be written as [9]:

$$P_{out} = G_{IF} k_B \Delta f [T_{IF} + (1 - \Gamma^2) T_{HEB}] \quad (5.12)$$

where k_B is Boltzmann's constant, Δf the bandwidth, T_{HEB} the temperature of HEB device. Γ is the reflection coefficient between the HEB device (normal state resistance, 67.4 Ω) and IF load resistance (50 Ω), and can be given by:

$$\Gamma = \frac{R_{HEB} - R_{IF}}{R_{HEB} + R_{IF}} \quad (5.13)$$

In the measurement, we recorded the IF output power of the HEB mixer at different temperatures and plotted the P - T curve in Figure 5.14. Then we linear fitted the curve and obtained the power P_0 at $T_{HEB} = 0K$ by oppositely elongating the fitted line. According to Eq. 5.12, P_0 can be written as:

$$P_0 = G_{IF} k_B \Delta f T_{IF} \quad (5.14)$$

Picking the other IF output power P_1 at high bath temperature and substituting both of them into Eq. 5.12 yields:

$$P_1 - P_0 = G_{IF} k_B \Delta f (1 - \Gamma^2) T_{HEB} \quad (5.15)$$

Combining Eq. 5.14 and Eq. 5.15, we can get:

$$T_{IF} = P_0 \cdot \frac{T_{HEB}}{P_1 - P_0} \cdot (1 - \Gamma^2) \quad (5.16)$$

where P_0 is the intercept and $\frac{T_{HEB}}{P_1 - P_0}$ is the inverse of the slope of the fitted line shown in

Figure 5.14. Therefore, the IF noise temperature of the 1.4-THz receiver system is:

$$T_{IF} = 17.7K \cdot [1 - (\frac{67.4\Omega - 50\Omega}{67.4\Omega + 50\Omega})^2] = 17.4K \quad (5.17)$$

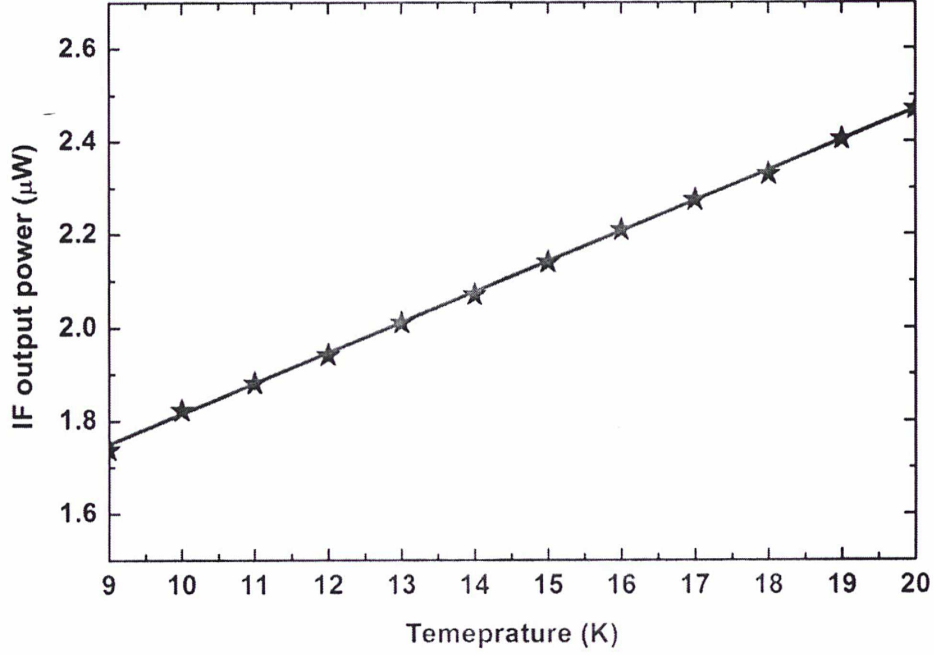


Figure 5.14: Measured IF output power of the HEB mixer at different temperatures and the linear fitted line.

The conversion gain G_{total} of the investigated HEB mixer can be evaluated using the U factor method. The U factor is defined as the ratio of the IF output power at the operating bias P_{295} to that at the zero dc bias without LO pumping P_{sc} , and is given by [10]:

$$U = \frac{P_{295}}{P_{SC}} = \frac{T_{295} + T_{rec}}{T_{bath} + T_{IF}} 2G_{total} \quad (5.18)$$

where T_{bath} is the effective radiation temperatures determined from their physical temperatures by the Callen-Welton formula. T_{IF} is the noise temperature of the IF chain. T_{rec} is the receiver noise temperature at the optimum bias point. Solving Eq. 5.18 for the total conversion gain G_{total} yields:

$$G_{total} = \frac{U(T_{bath} + T_{IF})}{2(T_{295} + T_{rec})} \quad (5.19)$$

Using this equation and the previous measured results of IF noise temperature and receiver noise temperature, we calculated the total DSB conversion gain $2G_{total}$ as a function

of the bias voltage at the optimal LO pumping level (shown in Figure 5.15). It can be seen that the maximum conversion gain is around -8 dB when the HEB mixer is biased at 0.4 mV. Subtracting the contributions of the quasi-optical components (-1.85 dB in this case, with antireflection coating) from G_{total} , the DSB conversion gain ($2G_{mixer}$) of the HEB device itself is about -6.15 dB.

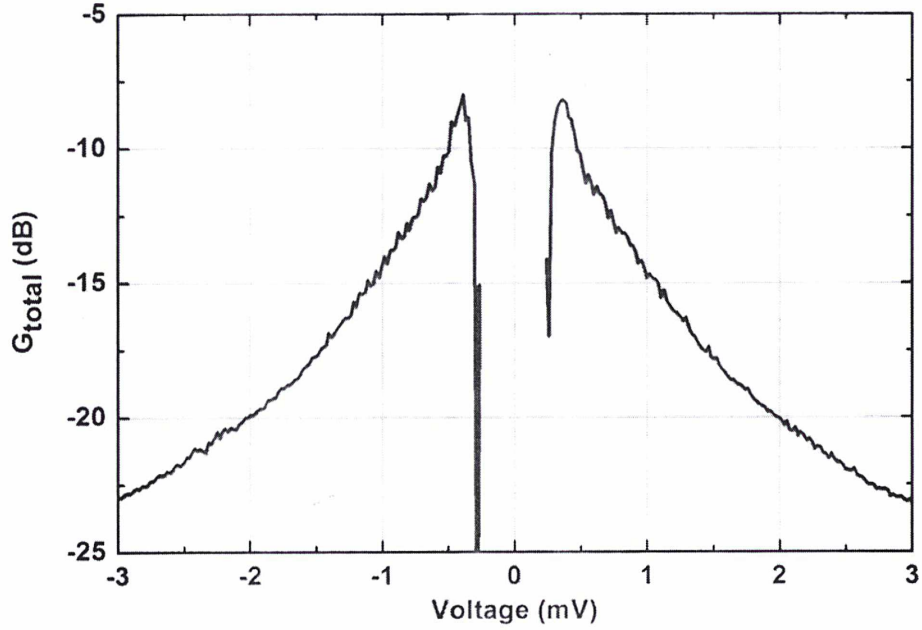


Figure 5.15: Total DSB conversion gain as a function of bias voltage at the optimal pumping.

Finally, since the receiver noise temperature, RF noise temperature, IF noise temperature, RF gain and conversion gain of the HEB device are all known, we can calculate the intrinsic noise temperature of the superconducting HEB device by Eq. 5.8. The calculated result of T_{mixer} is 225 K.

5.4.2 IF noise bandwidth

As mentioned in Chapter 2, the IF noise bandwidth of a HEB mixer is defined as the IF frequency at which the receiver noise temperature increases by a factor of two.

The measurement setup of IF noise bandwidth is nearly the same as that of noise temperature measurement. The difference is that the IF output power is recorded by a

spectrum analyzer instead of the square-law detector. The Y-factor method is used to calculate the receiver noise temperature as a function of IF frequency, as shown in Figure 5.16. The IF noise bandwidth can be obtained by fitting the data in Figure 5.16 with following equation:

$$T_{rec} = T_{opt} \left(1 + \left(\frac{f}{f_{IF,3dB}} \right)^2 \right) \quad (5.20)$$

where T_{opt} is the measured receiver noise temperature at optimal bias point, f is the IF frequency, $f_{IF,3dB}$ is the IF noise bandwidth. The value of $f_{IF,3dB}$ can be determined when the fitted curve accords well with the measured data. From the result shown in Figure 5.16, we obtain that the IF noise bandwidth of this HEB mixer is about 3 GHz.

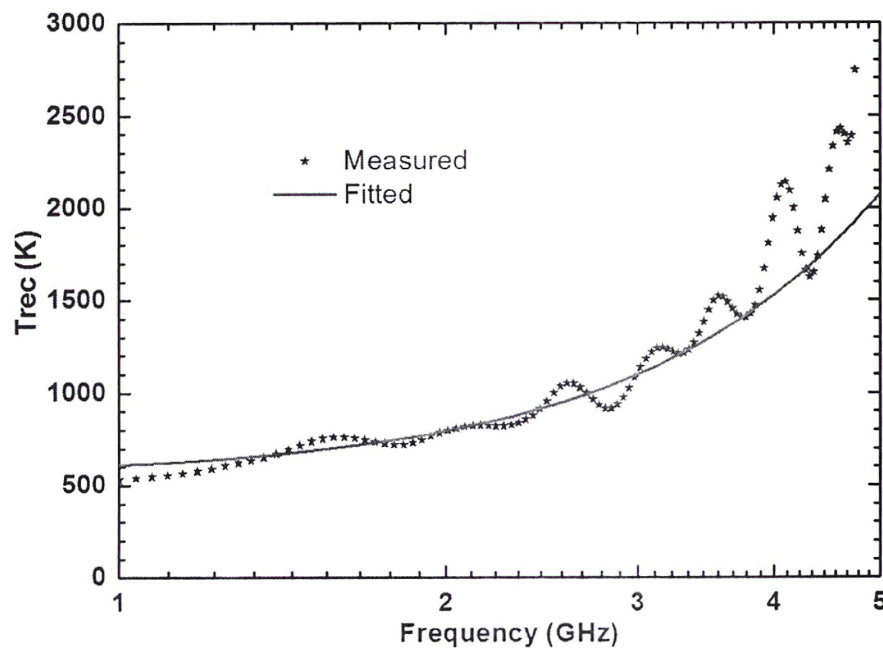


Figure 5.16: The IF noise bandwidth of the superconducting HEB mixer.

5.5 Intrinsic frequency response

The frequency response reflects the coupling efficiency of the mixer at different frequencies. In this section, we use a compact Fourier transform spectrometer (FTS) [11] to measure and calibrate the frequency response of the HEB mixer.

Figure 5.17 shows the schematic diagram of the compact FTS system. This FTS consists

of a Michelson interferometer with a mercury lamp providing broadband radiation. The FTS's beam splitter is a 25 μm thick Mylar. The signal from the mercury lamp was modulated by a chopper at about 27 Hz and the dc-current change of the HEB mixer was recorded by a lock-in amplifier synchronized with the chopper. The FTS was operated in a step-and-integrate mode. The maximum travel length is 41 mm and the step size is 10 μm , giving a frequency resolution of 3.66 GHz and a frequency bandwidth up to 7.5 THz.

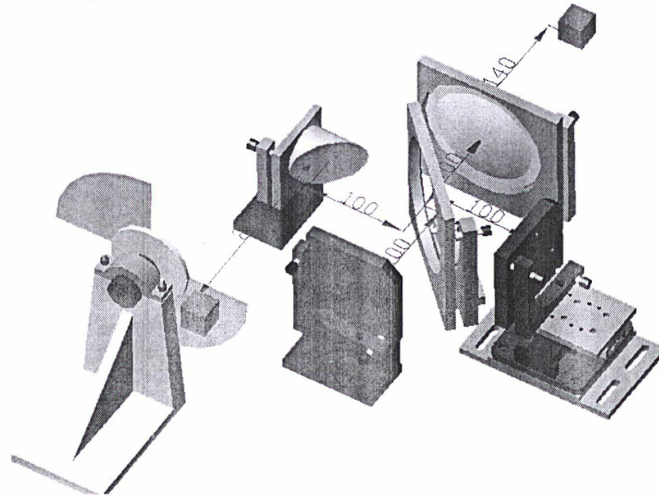


Figure 5.17: Schematic diagram of the compact FTS system.

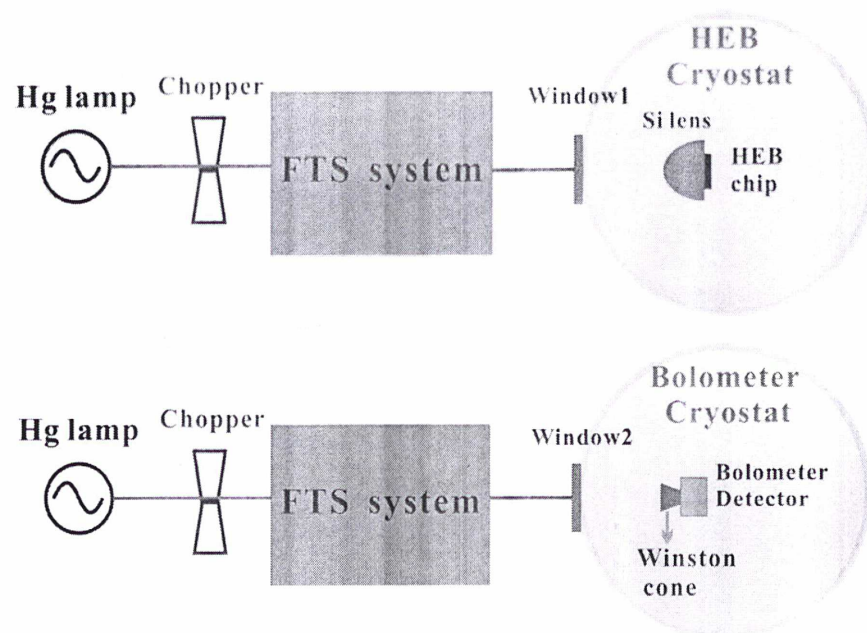


Figure 5.18: Measurement setup of frequency response of superconducting HEB mixer (upper) and setup of calibration measurement by Si bolometer (lower).

The measurement setup of frequency response is shown in the upper plot of Figure 5.18. Apparently, it can be seen that the directly measured frequency response of the HEB mixer includes the emission spectrum of the broadband signal source $S_{Hg}(\nu)$, the power transfer function of the FTS system $\eta_{FTS}(\nu)$, the air transmission $\eta_{air}(\nu)$, the transmission of the optical vacuum window and IR filter $\eta_{window1}(\nu)$, the transmission of silicon lens $\eta_{lens}(\nu)$ and the intrinsic frequency response of HEB device $\eta_{HEB}(\nu)$. In order to determine the intrinsic frequency response of the measured superconducting HEB device, we need to calibrate other responses.

The calibration measurement was done by a Si bolometer, the measurement setup is shown in the lower plot of Figure 5.18. According to two diagrams, the measured spectra of the HEB mixer ($S_{HEB}(\nu)$) and the Si bolometer ($S_{Bol}(\nu)$) can be expressed as:

$$\begin{aligned} S_{HEB}(\nu) &= S_{Hg}(\nu) * \eta_{FTS}(\nu) * \eta_{air}(\nu) * \eta_{window1}(\nu) * \eta_{lens}(\nu) * \eta_{HEB}(\nu) \\ S_{Bol}(\nu) &= S_{Hg}(\nu) * \eta_{FTS}(\nu) * \eta_{air}(\nu) * \eta_{window2}(\nu) * \eta_{Cone}(\nu) * \eta_{Si}(\nu) \end{aligned} \quad (5.21)$$

where $\eta_{lens}(\nu)$ is proportional to λ^2 because of diffraction limit, $\eta_{Cone}(\nu)$ the throughput of the Winston cone integrated in the Si bolometer (a constant), $\eta_{Si}(\nu)$ the frequency response of the Si bolometer (a constant) [12], $\eta_{window1}(\nu)$ the frequency response of vacuum window (2 mm HDPE) in HEB cryostat [13], and $\eta_{window2}(\nu)$ the frequency response of vacuum window and IF filter in Bolometer cryostat which can be found in [14]. The spectra measured by the HEB mixer and by the Si bolometer are shown in Figure 5.19, in which the air transmission calculated using an atmospheric model [15] is also plotted.

The intrinsic frequency response of the HEB device $\eta_{HEB}(\nu)$ can be determined by dividing $S_{HEB}(\nu)$ to $S_{Hg}(\nu)$, which can be given by:

$$\eta_{HEB}(\nu) = \frac{S_{HEB}(\nu)}{S_{Bol}(\nu)} * \frac{\eta_{window2}(\nu) * \eta_{Cone}(\nu) * \eta_{Si}(\nu)}{\eta_{window1}(\nu) * \eta_{lens}(\nu)} \quad (5.22)$$

Since all parameters on the right side of Eq. 5.22 are already known, the intrinsic frequency response of the HEB mixer $\eta_{HEB}(\nu)$ can be obtained straightforwardly.

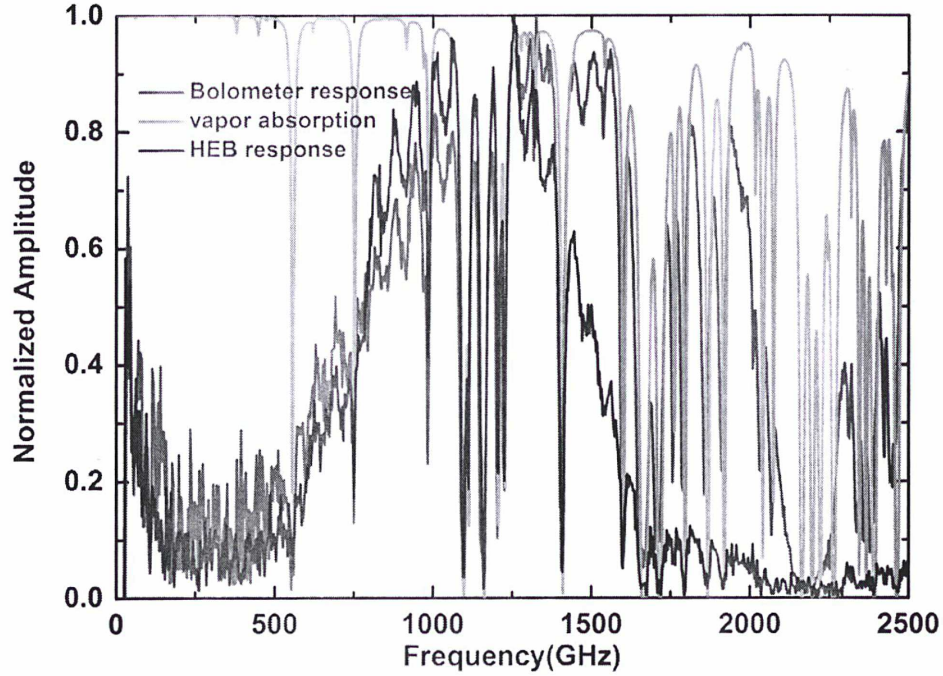


Figure 5.19: Measured frequency response spectrums of the HEB mixer and the Si bolometer without calibration. The air transmission line is calculated using an atmospheric model.

The calibrated frequency response of the 1.4-THz superconducting HEB mixer together with its fitted curve and residual are shown in Figure 5.20. Note that the singular data points caused by the water-vapor absorption line (shown in Figure 5.19) were removed. The calibrated intrinsic frequency response still includes the coupling efficiency between the planar antenna and HEB microbridge and the intrinsic direct-detection responsivity of the HEB device. Therefore, we theoretically calculated the coupling efficiency of the double slot antenna based on an infinite Si substrate using FEKO [16]. As shown in Figure 5.20, the simulated frequency response of the double slot antenna is in good agreement with the calibrated intrinsic frequency response of the HEB mixer, indicating that the intrinsic direct-detection responsivity of the HEB device is nearly frequency independent. Note that the normal state resistance is used as the resistance of HEB device in the coupling efficiency simulation of the double slot antenna. From Figure 5.20 we can also find that the coupling efficiency is quite high in the frequency range of 0.8~1.5 THz.

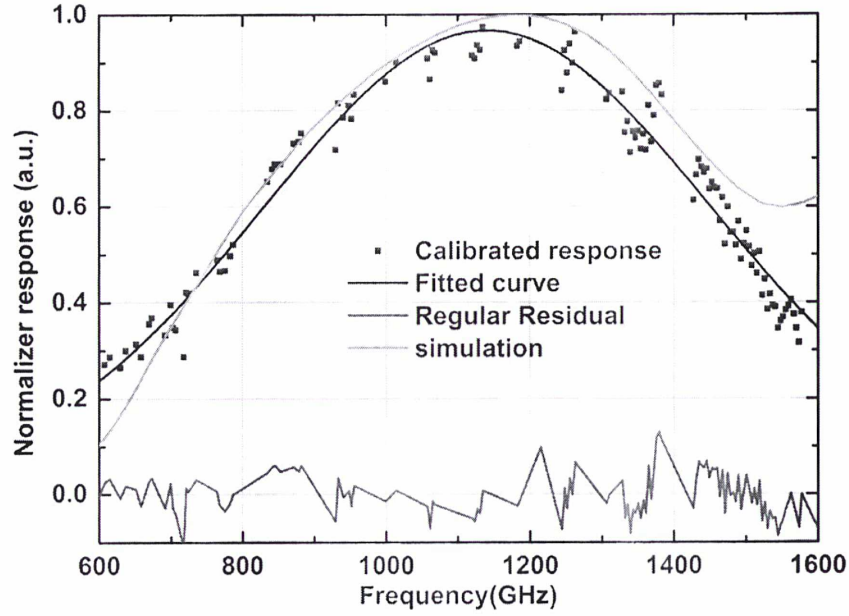


Figure 5.20: Calibrated spectral response (square symbol) of the HEB mixer and the simulated coupling efficiency of the twin-slot antenna (green line). The fitted curve (black line) for the calibrated response and its residual (red line) are also plotted.

5.6 Far-field beam pattern

The far-field beam pattern of this superconducting HEB mixer was measured by the vector near-field measurement system introduced in section 4.3.2. We obtained the far-field beam-pattern by means of the near-to-far (NTF) transformation. The far-field beam pattern was measured at 850 GHz since we don't have two signal sources at 1.4 THz.

The system is made up of a test channel and a phase reference channel. In the test channel, the LO signal is provided by a frequency synthesizer followed by an amplifier multiplier chain (AMC) with a total multiplication factor of 54, while the RF signal is generated by an AMC with a total multiplication factor of 72. The RF and LO signals centered around 850 GHz are coupled to the HEB mixer through a beam-splitter of a 50 μm -thick Mylar film. The 360 MHz IF signal, after proper amplification and filtering, is directly sampled by a high-speed A/D converter (ADC). The phase reference signal is generated by a millimeter mixer instead of another receiver. The output of the RF (11.81 GHz)

and LO (15.74 GHz) frequency synthesizers are fed into a 4 times multiplier and a 3 times multiplier, respectively, to generate two millimeter signals at 47.24 GHz and 47.22 GHz. The mixing of two signal by a Q-band mixer yields a 20 MHz IF signal, which is used as the phase reference for the test IF signal at 360 MHz.

A raster scan which is 350 mm away from the aperture of HEB mixer and covers an area of $100 \times 100 \text{ mm}^2$ is performed to measure the near-field amplitude and phase distributions. The measurement results are shown in Figure 5.21. Obviously the amplitude and phase distribution have a good Gaussian shape. Figure 5.22 shows the far-field beam patterns in E-plane and H-plane obtained by the near-to-far (NTF) transformation at 850 GHz, with a full width at -10 dB level of 3.4° in E-plane and 3.8° in H-plane. Clearly, the main beam is well collimated. The E-plane and H-plane side lobes are 15 dB and 20 dB below the main lobe. Figure 5.22 also shows the simulated far-field beam pattern (by GO/PO method) is in good agreement with the measured one.

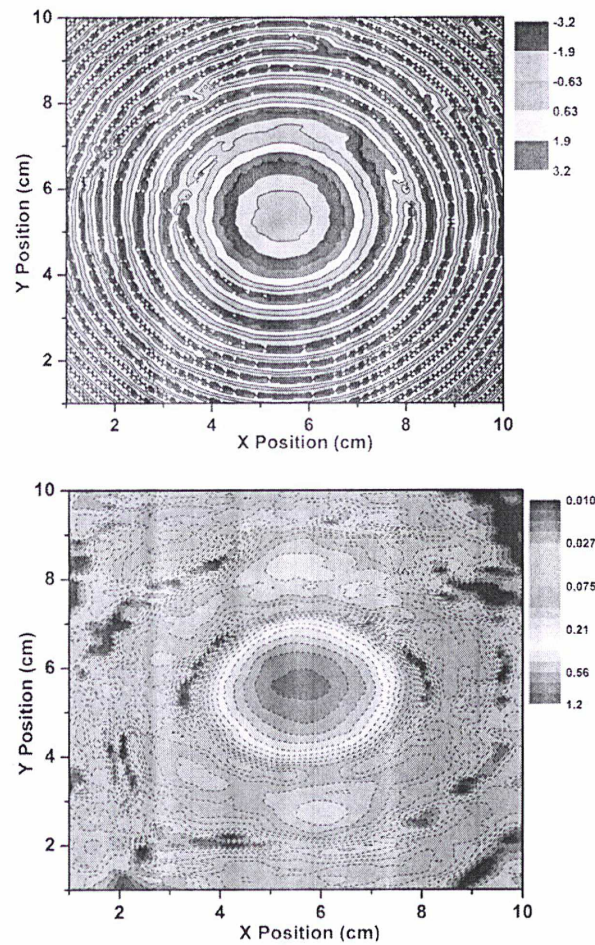


Figure 5.21: Measured near-field phase (upper) and amplitude (lower) spectrum at 850 GHz.

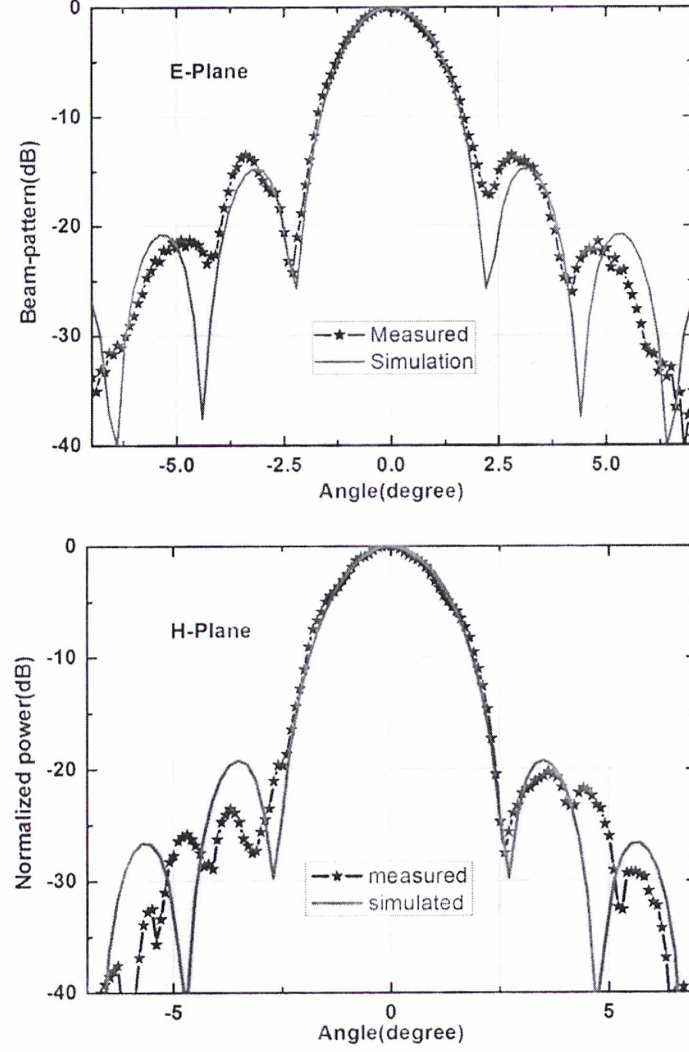


Figure 5.22: E-plane (upper) and H-plane (lower) far-field beam-patterns obtained by the near-to-far (NTF) transformation. Simulation results are also plotted for comparison.

5.7 Effect of lens's extension length on the mixer's performance

The characterizations in previous sections are performed by the elliptical lens with an extension length of 1.149 mm. In this section, we investigate the noise temperature and frequency response of the HEB mixer using elliptical lenses with different extension lengths. The corresponding far-field beam-patterns, directivity and Gaussicity have also been

simulated.

Four elliptical lenses with same ellipsoid shape but different extension length are selected. The extension lengths are 1.109 mm, 1.149 mm, 1.189 mm and 1.229 mm respectively. According to geometrical optics, the focus length c of major axis of the elliptical lens is determined by the major axis length b and the dielectric constant ϵ_r :

$$c = \frac{b}{\sqrt{\epsilon_r}} \quad (5.23)$$

Taking 11.43 as the silicon dielectric constant, the focus length is 1.549 mm (including the 0.4 mm thickness of HEB device chip). Therefore, when the extension length is 1.149 mm all the rays will focus to the major axis foci.

The noise temperature was measured at 1.3 THz using the Y-factor method. The measurement setup is illustrated in Figure 5.6. The measured double-sideband (DSB) noise temperatures of the superconducting HEB mixer with four extension lengths are shown in Figure 5.23. The superconducting HEB mixer was pumped to the same level by monitoring its I-V curve during all the measurements. It can be clearly seen from Figure 5.23 that the receiver noise temperatures are independent of the extension length.

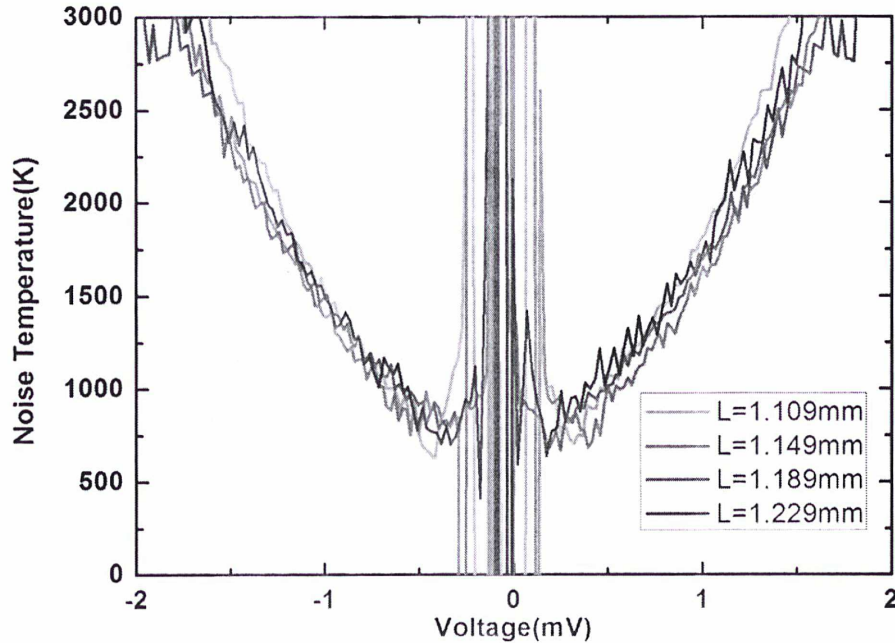


Figure 5.23: Measured DSB noise temperatures for the extension length of 1.109 mm, 1.149 mm, 1.189 mm and 1.229 mm at 1.3 THz.

The frequency response of the superconducting HEB mixer was measured by the compact Fourier transform spectrometer (FTS) mentioned in section 5.6. Note that the measurements were performed at a temperature close to the HEB's transition temperature to have a same direct-detection responsivity. The measured frequency responses are shown in Figure 5.24. The normalized frequency responses show limited dependence to the extension length too.

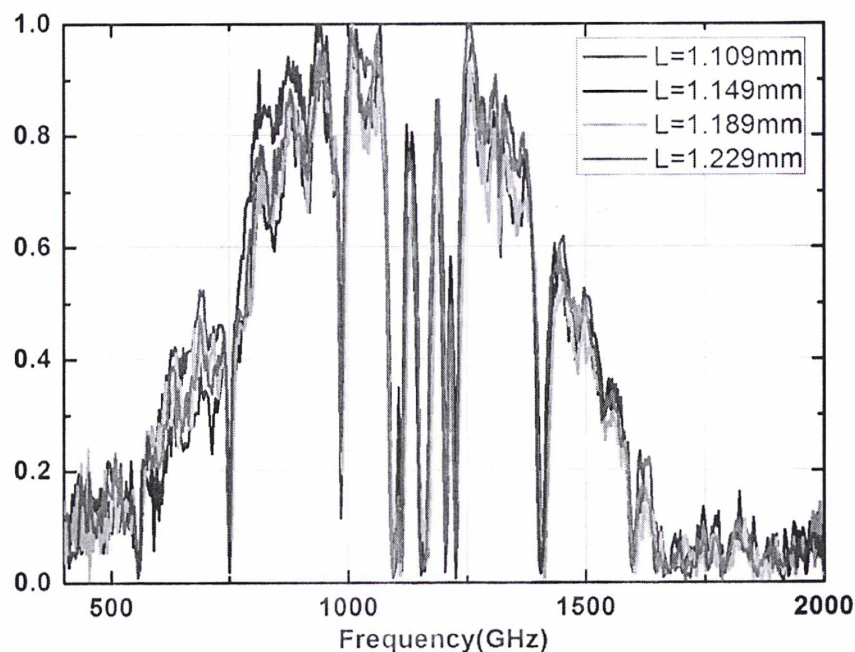


Figure 5.24: Measured frequency responses for the extension length of 1.109 mm, 1.149 mm, 1.189 mm and 1.229 mm.

In addition, we investigated the effect of extension length on far-field beam pattern. We simulated the E- and H-plane far-field beam pattern (GO/PO method) of the superconducting HEB mixer at 1.3 THz for the four extension lengths. As shown in Figure 5.25, the narrowest pattern occurs at $L=1.149$ mm, which appears the best solution as the main-lobe widths and the side-lobe levels increase at other extension lengths.

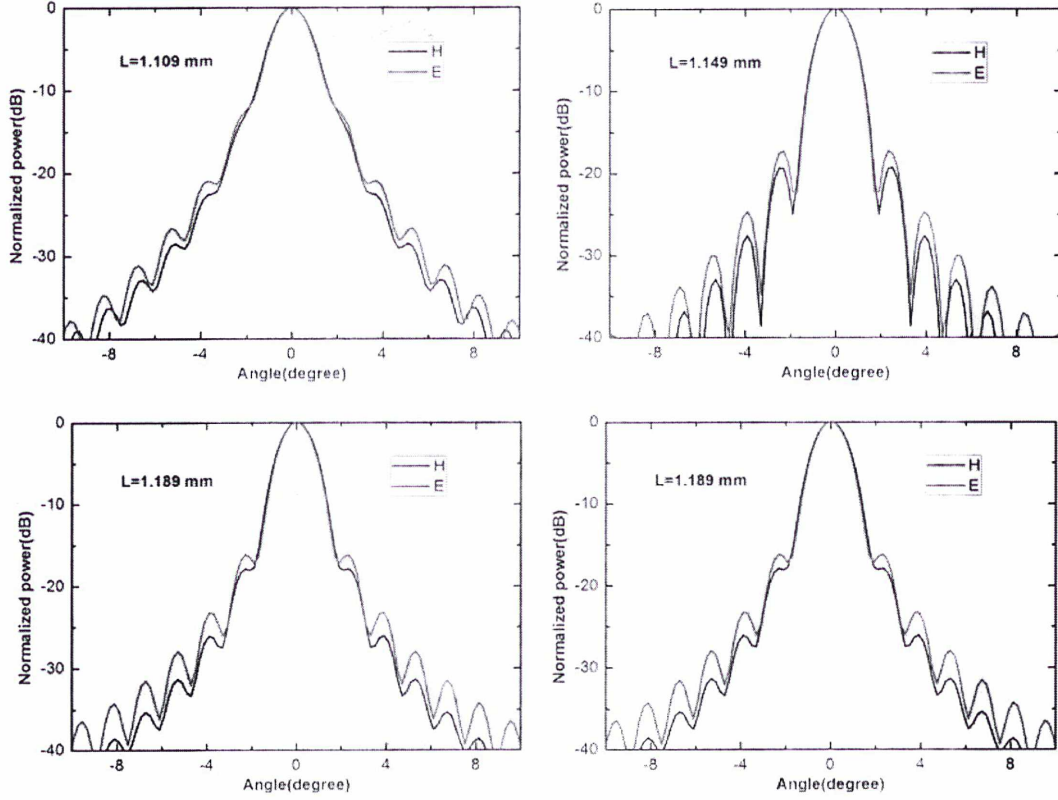


Figure 5.25: Simulated far-field beam-patterns for the extension length of 1.109 mm, 1.149 mm, 1.189 mm and 1.229 mm at 1.3 THz

The simulated peak directivity and the Gaussicity (coupling efficiency) as a function of the extension length are shown in Figure 5.26. The directivity has a peak of 39.4 dB at $L=1.149$ mm and remains within 1.0 dB of the peak between 1.12 mm and 1.19 mm. The Gaussicity has a peak of 90.98% at $L=1.149$ mm. Both peaks are centered at an extension length around $L=1.149$ mm, which is indeed the focus length of major axis of elliptical lens. The beam-waist width was also calculated. As shown in Figure 5.27, the peak of 4.1 mm is located around $L=1.149$ mm as expected. Similar simulations were done at 850 GHz to understand the frequency dependence of the above parameters. As plotted in Figure 5.26 and Figure 5.27, the peaks are mostly centered at $L=1.149$ mm too.

In conclusion, we found that the noise temperature and frequency response are nearly independent of the lens extension length, but the directivity, Gaussicity and beam-waist width are not the case. As far as the beam pattern is concerned, the optimum extension length is equal to the focus length of major axis of the elliptical lens.

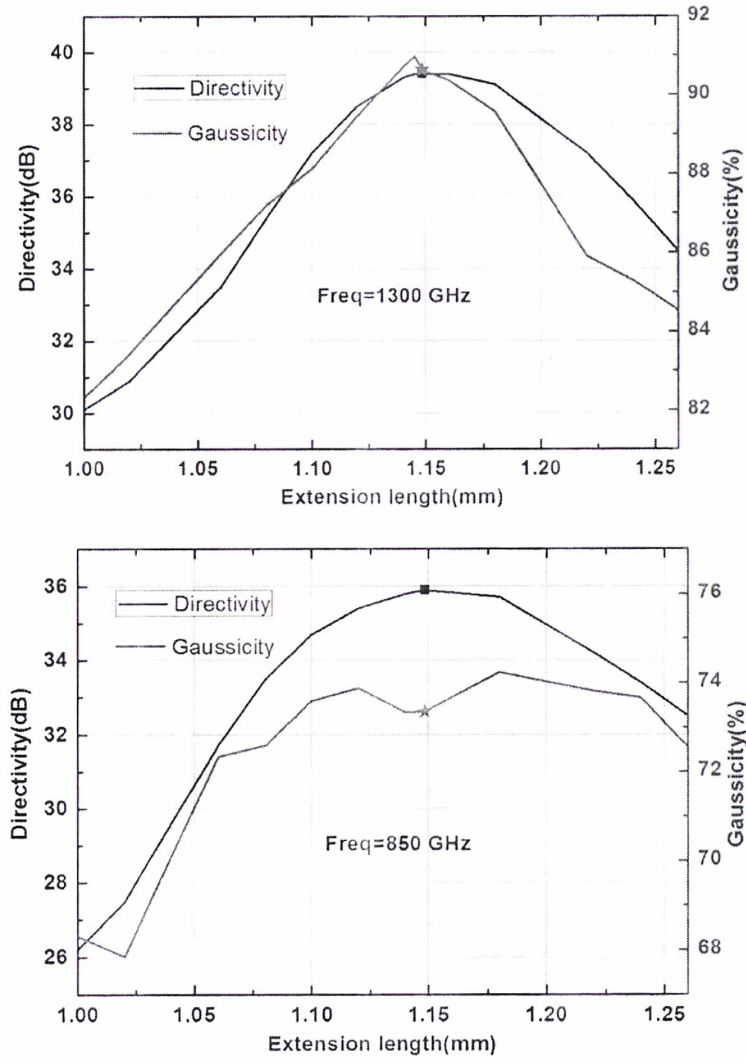


Figure 5.26: Calculated directivity and Gaussicity as a function of the extension length at 1300 GHz (upper) and 850 GHz (lower). The geometric focus point is denoted by symbols.

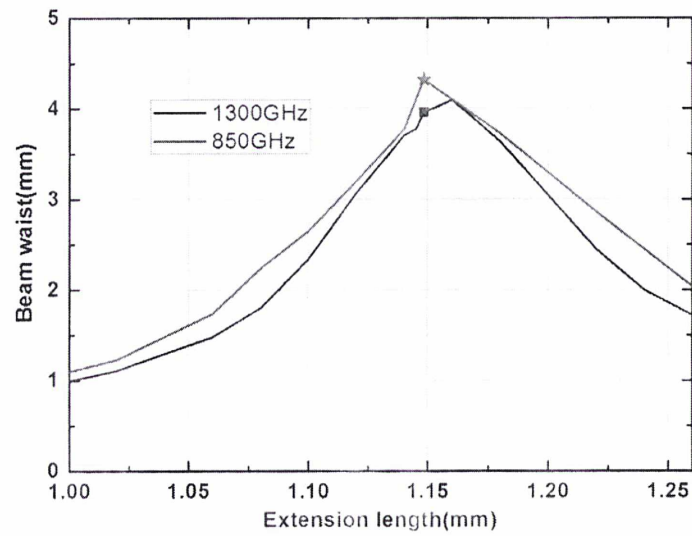


Figure 5.27: Calculated beam waist as a function of the extension length at 1300 GHz and 850 GHz. The geometric focus point is denoted by symbols.

5.8 Conclusion

We have designed and fabricated a quasi-optical 1.4 THz superconducting HEB mixer using integrated lens/double slot antenna. We have then performed a full characterization of the parameters related to the mixer's performance. The noise temperature measurement has demonstrated a state of the art sensitivity (600 K) at 1.3 THz. We have characterized the intrinsic frequency response of the HEB device by applying a new method, the RF bandwidth is from 0.8 THz to 1.5 THz. The near and far-field beam patterns of this mixer have been measured, analyzed and compared to the simulation. The simulated far-field beam pattern appears in good agreement with the measured one. We investigated the effect of the extension length of the elliptical lens on the noise temperature, the frequency response and the far-field beam pattern of the mixer. We found that the noise temperature and frequency response are nearly independent of the lens extension length, but the directivity, Gaussicity and beam-waist width are strongly dependent on the lens extension length.

Bibliography

1. X. Gong et al., "Dome A site testing and future plans," *EAS Publications Series*, Vol. 40, pp. 65-72, 2010.
2. C.A. Kulesa et al., "Pre-HEAT: submillimeter site testing and astronomical spectra from Dome A, Antarctica," *SPIE Astronomical Telescopes and Instrumentation. International Society for Optics and Photonics*, p. 701249, 2008.
3. P. Yagoubov, G. Gol'tsman, B. Voronov, L. Seidman, V. Siomash, S. Cherednichenko and E. Gershenson, "The bandwidth of HEB mixers employing ultrathin NbN films on sapphire substrate," in *Proc. of 7th International Symposium on Space Terahertz Technology*, pp. 290-302, 1996
4. R. Lefèvre, Y. Jin, A. Féret, T. Vacelet, W. Miao, L. Pelay, F. Dauplay, M. Ba-Trung, J. Spatazza, J.-C. Villégier, J.-M. Krieg, Y. Delorme, "Terahertz NbN hot electron bolometer

- fabrication process with a reduced number of steps.”*Proc. of 23rd International Symposium on Space Terahertz Technology, Tokyo, Japan*, pp. 127-130, 2012.
5. J. J. Baselmans, M. Hajenius, J. R. Gao, T. M. Klapwijk, P. A. J. de Korte, B. Voronov, and G. Gol’tsman, “Doubling of Sensitivity and Bandwidth in Phonon Cooled Hot Electron Bolometer Mixers,” *Applied Physics Letters*, Vol. 84, No. 11, pp. 1958-1960, 2004
 6. http://en.wikipedia.org/wiki/Planck's_law.
 7. Baselmans, J. J. A., et al. "Direct detection effect in small volume hot electron bolometer mixers." *Applied Physics Letters*, 86.16 (2005): 163503-163503.
 8. W. Miao, W. Zhang, K.M. Zhou, K. Zhang, W.Y. Duan, Q.J. Yao, and S.C. Shi, "Direct measurement of the input RF noise of superconducting hot electron bolometer receivers " *Applied Superconductivity, IEEE Transactions on* 23.3 (2013): 2300104-2300104.
 9. Sheng-Cai Shi, "Quantum-limited broadband mixers with superconducting tunnel junctions at millimeter and submillimeter wavelengths," *PhD dissertation*, 1996
 10. Pourya Khosropanah, “NbN and NbTiN Hot Electron Bolometer THz Mixers,” *PhD thesis*, Chalmers University of Technology, 2003.
 11. X.S. Cao and S.C. Shi. “Development of a compact THz FTS system,” *8th International Symposium on Antennas, Propagation and EM Theory*, Vol. 2-5, pp. 1498-1501, 2008
 12. Kenneth D. Kempfert, Eric Y. Jiang, Sberwin Oas, John Coffin. " Detectors for Fourier Transform Spectroscopy", [Online] Available: <http://mmrc.caltech.edu/FTIR/Nicolet/Nicolet%20Tech%20Notes/DetectorsforFTIR1204.pdf>
 13. [Online]. Available: <http://www.mtinstruments.com/thzlenses/>
 14. [Online]. Available: <http://www.infraredlaboratories.com/Bolometers.html>
 15. S. Paine, Am Atmospheric Model. [Online]. Available: <https://www.cfa.harvard.edu/~spaine/am/>
 16. FEKO: A computer code for the analysis of electromagnetic problems. EM Software & Systems-S.A. (Pty) Ltd., Stellenbosch, South Africa.

Chapter 6

Investigation of a 0.1-1.5 THz broadband HEB Mixer

6.1 Mixer design

The structure of the broadband superconducting HEB mixer is the same as mentioned in Chapter 3. The HEB microbridge together with the planar spiral antenna [1] is fabricated on a highly resistive Si substrate. The schematic of the planar spiral antenna is shown in Figure 6.1. The NbN microbridge of 2 μm wide, 0.2 μm long and 3.5 nm thick locates in the center of the spiral antenna, and is connected to the antenna by two Ti/Au contact pads. The HEB device chip is mounted on the flat surface of an elliptical lens with a major axis length of 5.228 mm and minor axis length of 5 mm. The extension length of the elliptical lens is 1.149 mm.

The operating frequency of the spiral antenna is designed from 0.1 THz to 1.5 THz. Parameters calculated from the Eq. 3.10 are listed in Table 6.1.

Table 6.1 Parameters of the spiral antenna designed from 0.1 THz to 1.5 THz

Frequency	a	δ	$\text{Max}\Phi$	r_0	d	D
THz				μm	μm	μm
0.1-1.5	0.32	1.5	11.2	5.5	8.4	300

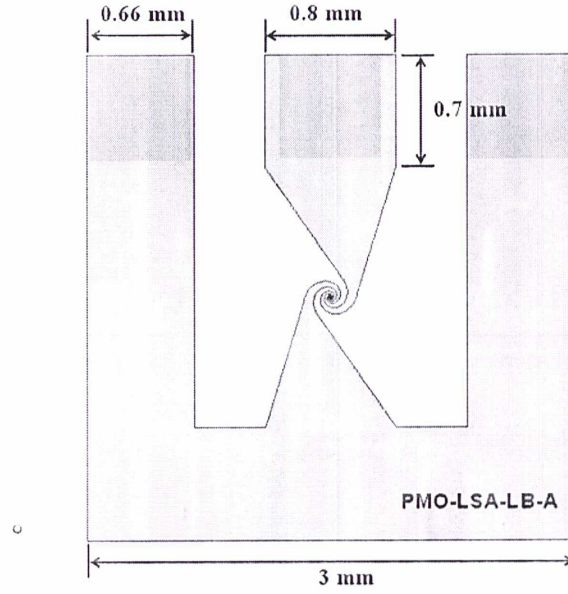


Figure 6.1: Schematic structure of the spiral antenna.

The simulated input resistance and reactance of the planar spiral antenna are shown in Figure 6.2. The resistance is about 80Ω and the reactance is small enough to be neglected within the frequency range of 0.1-1.5 THz.

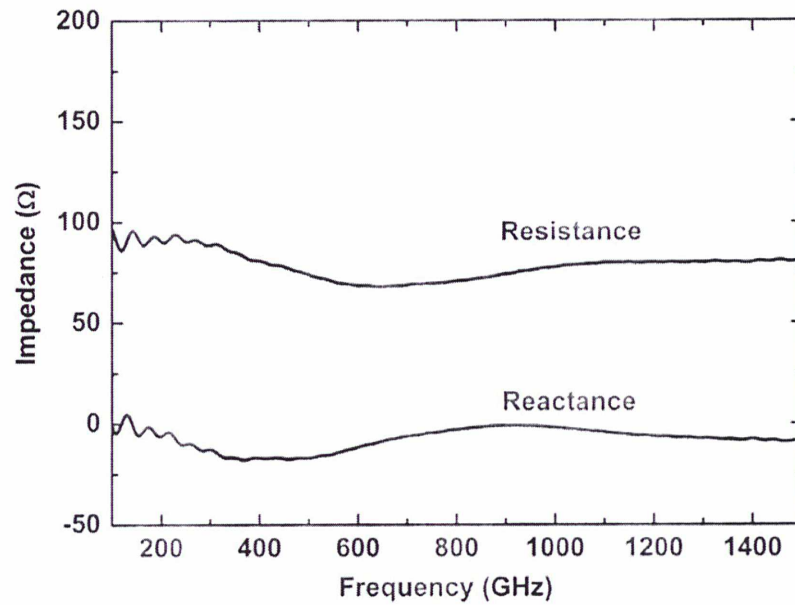


Figure 6.2: Input resistance and reactance of the planar spiral antenna

In addition, we simulated the E-plane and H-plane far-field beam pattern of this HEB mixer at 0.2 THz, 0.5 THz, 0.8 THz, 1.1 THz and 1.4 THz, as shown in Figure 6.3. It can be

seen clearly that the main-lobe is strongly dependent on the operating frequency, however the side-lobe levels are mostly at -17 dB.

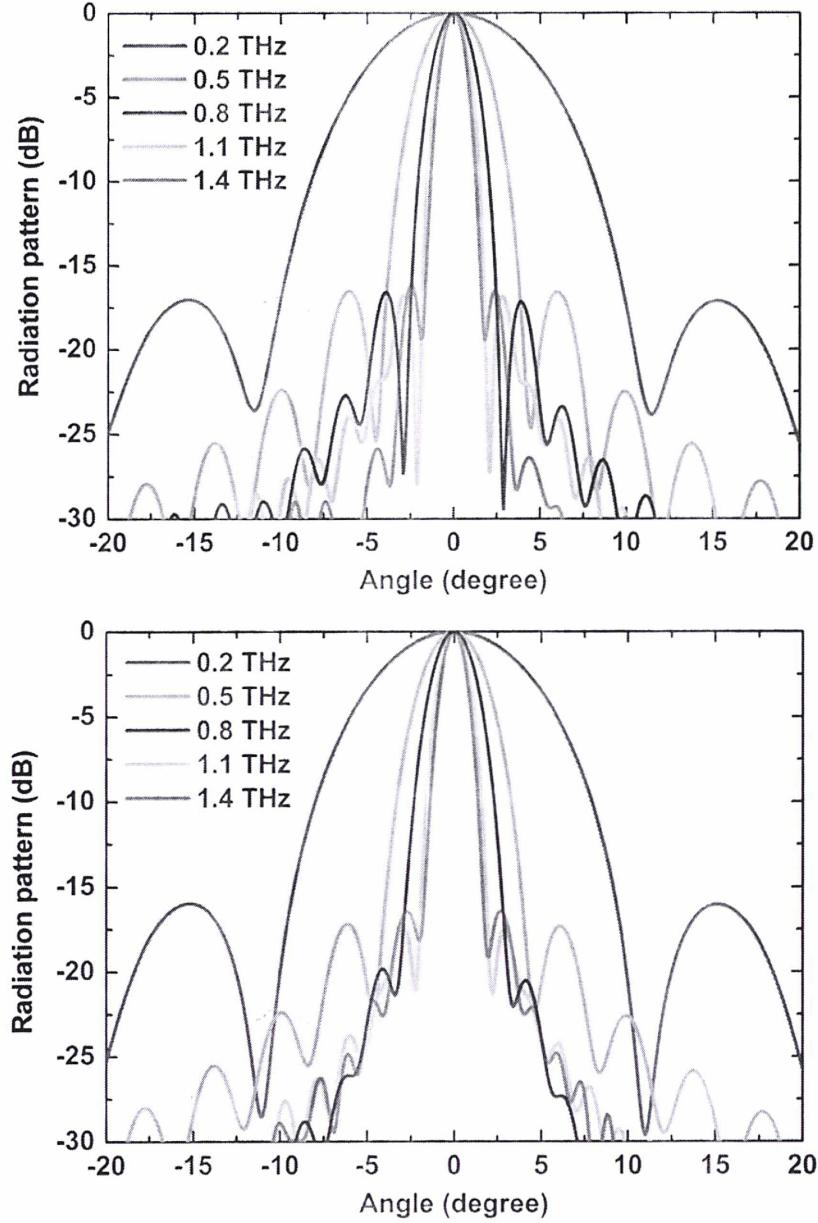


Figure 6.3: Simulated E-plane (upper) and H-plane (lower) far-field beam pattern of the spiral antenna coupled HEB mixer.

6.2 DC characteristic

The broadband superconducting HEB device used in this thesis is made of niobium

nitride and is provided by Moscow State Pedagogical University (MSPU) [2]. The measured I - V curve and R - T curve of this mixer are shown in Figure 6.4. The critical current is nearly 93 μA . Two superconducting transitions can be observed at 5.8 K and 7.4 K respectively, with the lower one due to the proximity effect at the NbN-Au interface and the higher one due to the NbN microbridge itself. The normal state resistance is 113 Ω .

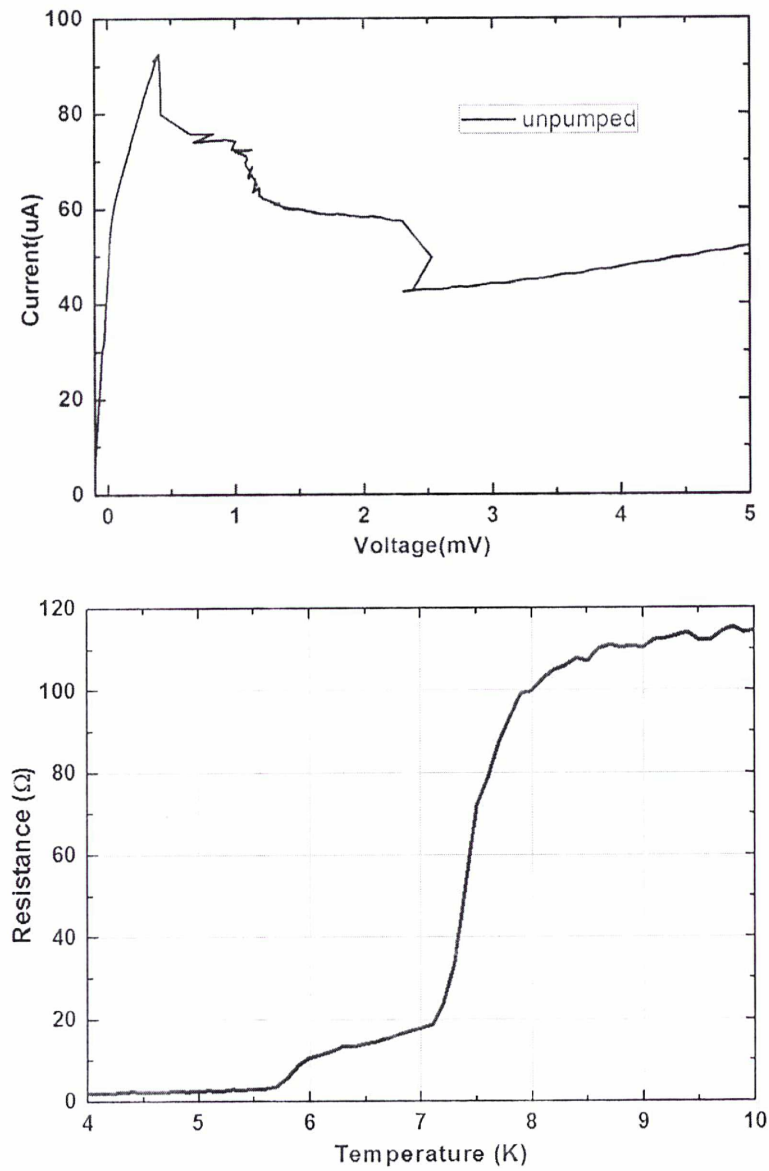


Figure 6.4: Measured I - V curve (upper) and R - T curve (lower) of the spiral antenna coupled superconducting HEB mixer.

6.3 Receiver noise temperature

The measurement setup of receiver noise temperature is illustrated in Figure 5.6. Since this is a broadband mixer, the noise temperature measurements were performed at 220 GHz, 330 GHz, 500 GHz, 850 GHz and 1300 GHz. The LO sources at 220 GHz, 330 GHz and 500 GHz are Gunn oscillators together with multipliers, and the LO sources at 850 GHz and 1300 GHz are solid state multiplier chains together with signal synthesizers.

Figure 6.5 illustrates the measured I - V curves at the optimal pumping level at five frequencies. The HEB mixer was always biased at 1 mV and 25 μ A. The HEB mixer wasn't pumped enough at 1.3 THz since the LO source output was too low. We can also find in Figure 6.5 that the well-pumped I - V curves at 220 GHz and 330 GHz still show negative resistance while the I - V curves at other frequencies don't. This can be attributed to the non-uniformly absorption of terahertz radiation in the superconducting microbridge when the photon energy of the incoming radiation is lower than the energy gap of the microbridge $\hbar\omega < 2\Delta_0$ [3].

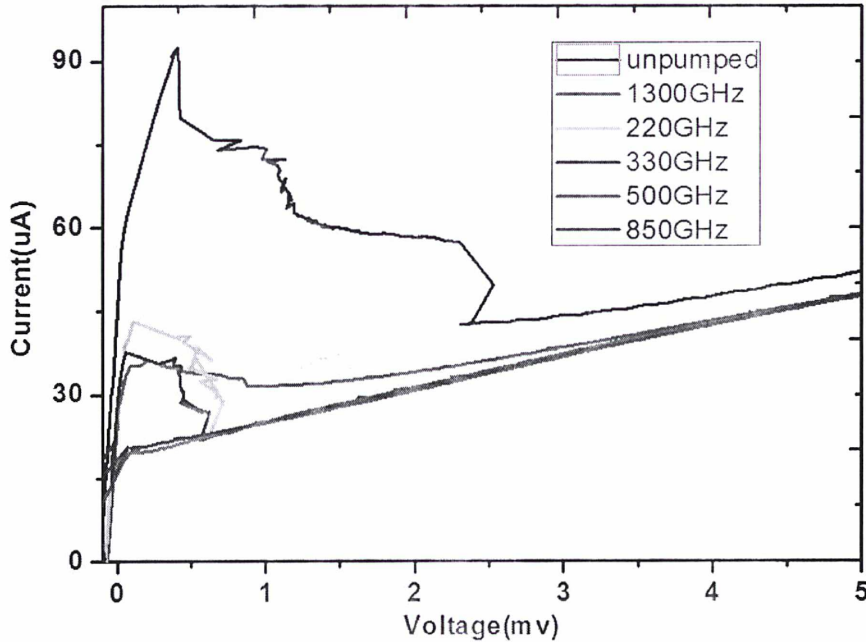


Figure 6.5: Pumped I - V curves of the HEB mixer at different frequencies.

Figure 6.6 shows the measured receiver noise temperature and the corresponding IF

output powers as a function of the HEB dc-bias voltage at five frequencies. The direct detection effect was compensated by adjusting the LO power [4] to make the IV curves unchanged between the hot- and cold-load measurement. The measured uncorrected DSB receiver noise temperatures are listed in Table 6.2. Note that the noise temperature at 1300 GHz is a little larger since the HEB device is not pumped to the optimal region.

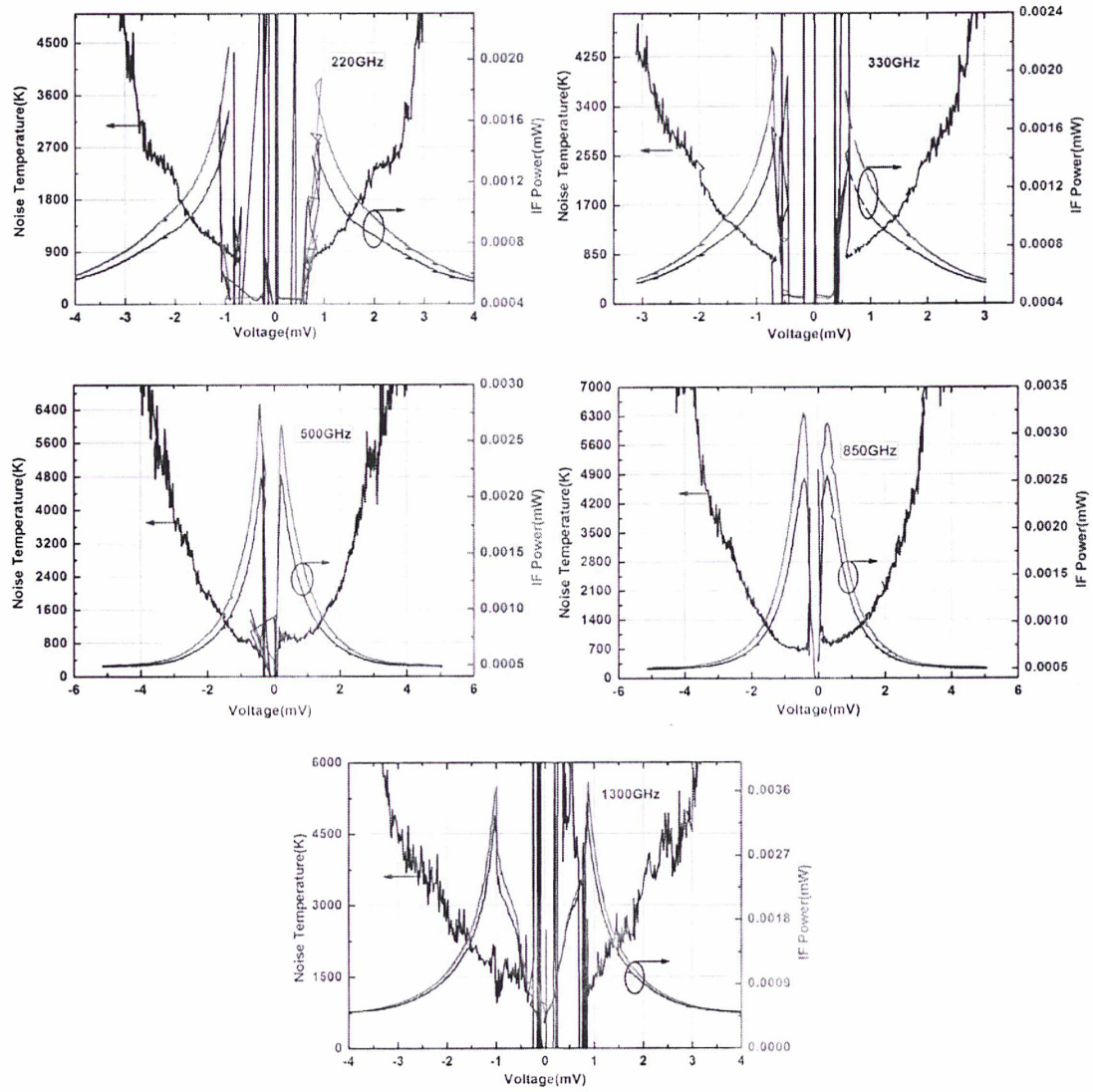


Figure 6.6: Measured receiver IF output powers and the corresponding receiver noise temperature as a function of the HEB dc-bias voltage at five frequencies.

Table 6.2 Measured uncorrected DSB receiver noise temperatures

Frequency(GHz)	220	330	500	850	1300
$T_{\text{rec}}(\text{K})$	950	850	800	700	1500

According to the analysis in section 5.4.1, we calculated the RF noise and gain of this superconducting HEB mixer at five frequencies, as listed in Table 6.3. The calculated RF noises are in the range of 23 K to 238 K.

Table 6.3 RF noise and gain

	220 GHz		330 GHz		500 GHz		850 GHz		1300 GHz	
	Noise	Gain	Noise	Gain	Noise	Gain	Noise	Gain	Noise	Gain
Beam splitter	2.42K	0.992	5.5K	0.982	12.5K	0.96	34.5K	0.897	218K	0.58
Window	13.2K	0.958	15.8K	0.95	16.5K	0.95	20.2K	0.94	42.6K	0.876
Zitex G104	4.1K	0.95	4.1K	0.95	4.1K	0.95	4.15K	0.95	4.27K	0.94
Lens reflect	2.6K	0.7	3.5K	0.7	5.2K	0.7	8.74K	0.7	13.4K	0.7
Total	23	0.63	30	0.62	40.2	0.61	72.8	0.56	238	0.334

In addition, we measured the IF noise bandwidth at 500 GHz and 850 GHz, as shown in Figure 6.7. The calculated IF noise bandwidth is 3.4 GHz@500 GHz and 3.5 GHz@850 GHz, showing no obvious dependence on RF frequency.

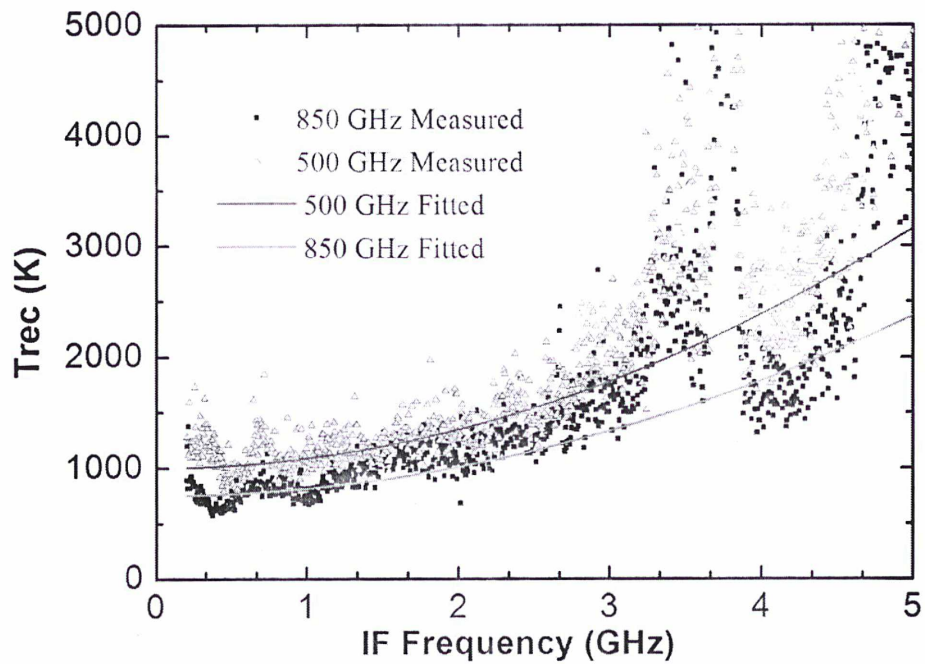


Figure 6.7: Measured IF noise bandwidth at 500 GHz and 850 GHz.

6.4 Spectral Response

A FTS system based on Martin-Puplett interferometer [5] was employed to measure the spectral response of the spiral antenna coupled superconducting HEB mixer. The schematic of this FTS is shown in Figure 6.8. The input signal is horizontal polarized at Polarizer 1, and is then divided by a 45° wire-grid, Polarizer 2, into two beams (reflected and transmitted) which have an angle of $\pm 45^\circ$ with horizontal plane respectively. Then they are reflected by a roof mirror and the polarization direction deflects 90 degrees. Therefore, both of them can pass through Polarizer 2 and no signal return to input port. Compared to a Michelson interferometer, a Martin-Puplett interferometer can provide a coupling efficiency much higher and a frequency dependence negligible since the wire grid is used instead of the dielectric film as beam splitter. The input ports of the FTS are two blackbodies with different temperatures (77 K and 295 K). The blackbody is made by terahertz RAMs and has a reflection less than -30 dB [6]. Roof mirror1 is fixed and Roof mirror2 is moveable. The maximum resolution of the FTS system is 6 GHz.

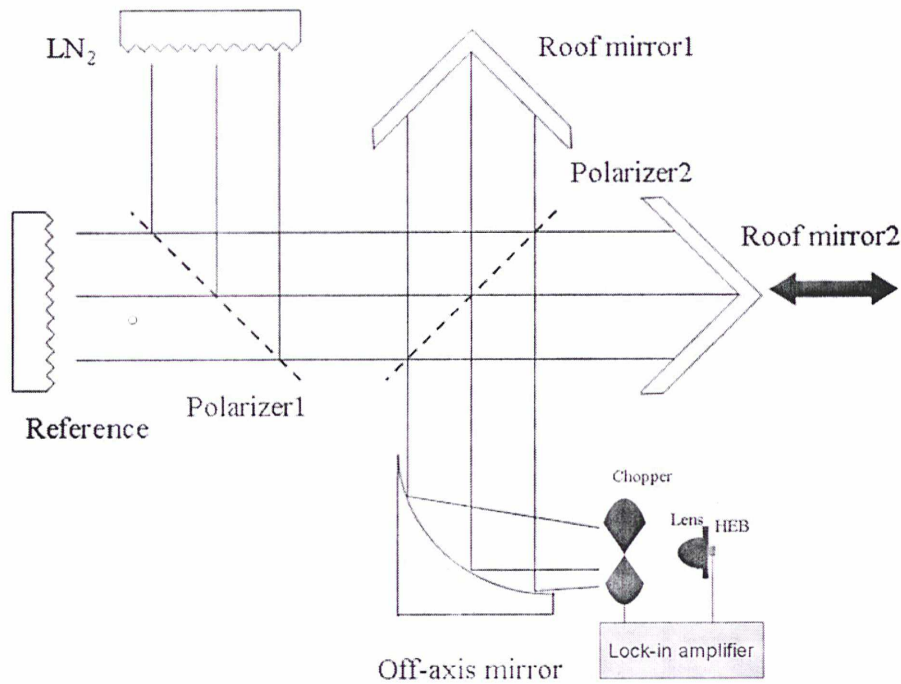


Figure 6.8: Schematic of the FTS system based on Martin-Puplett interferometer.

The directly measured spectral response by the FTS can be expressed as:

$$S_{HEB}(\nu) = [B_{295K}(\nu) - B_{77K}(\nu)] * \eta_{FTS}(\nu) * \eta_{optic}(\nu) * \eta_{HEB}(\nu) \quad (6.1)$$

where $S_{HEB}(\nu)$ is the measured spectral response, $B_{295K}(\nu) - B_{77K}(\nu)$ the input blackbody signal and can be calculated by Planck's law [7], $\eta_{FTS}(\nu)$ the frequency response of FTS system, $\eta_{optic}(\nu)$ the frequency response of optical components in measurement system, $\eta_{HEB}(\nu)$ the frequency response of HEB mixer.

The superconducting HEB mixer is operated as a direct detector. The input blackbody signal can be approximated to Rayleigh-Jeans limit in the frequency range of 0.2 THz - 2 THz, and then $B_{295K}(\nu) - B_{77K}(\nu)$ is frequency independent. What's more, $\eta_{FTS}(\nu)$ is also frequency independent since the reflection and transmission of wire grid is frequency independent. Therefore, the directly measured spectral response by the FTS is the combination of frequency response of optical components $\eta_{optic}(\nu)$ in measurement system and the frequency response of HEB mixer $\eta_{HEB}(\nu)$.

As presented in section 6.3, we have measured the noise temperature of the superconducting HEB mixer at five frequencies. Therefore, we can obtain the heterodyne spectral response of this mixer by using the measured Y-factor. Figure 6.9 illustrates the spectral response of the HEB mixer measured by an FTS in direct detection mode and by the Y-factor method in heterodyne mode. Not surprisingly, the heterodyne sensitivity closely follows the spectral response measured with the FTS. The data shows that this mixer has an input bandwidth of 0.2 THz - 2 THz, the peak response of the mixer is around 0.85 THz.

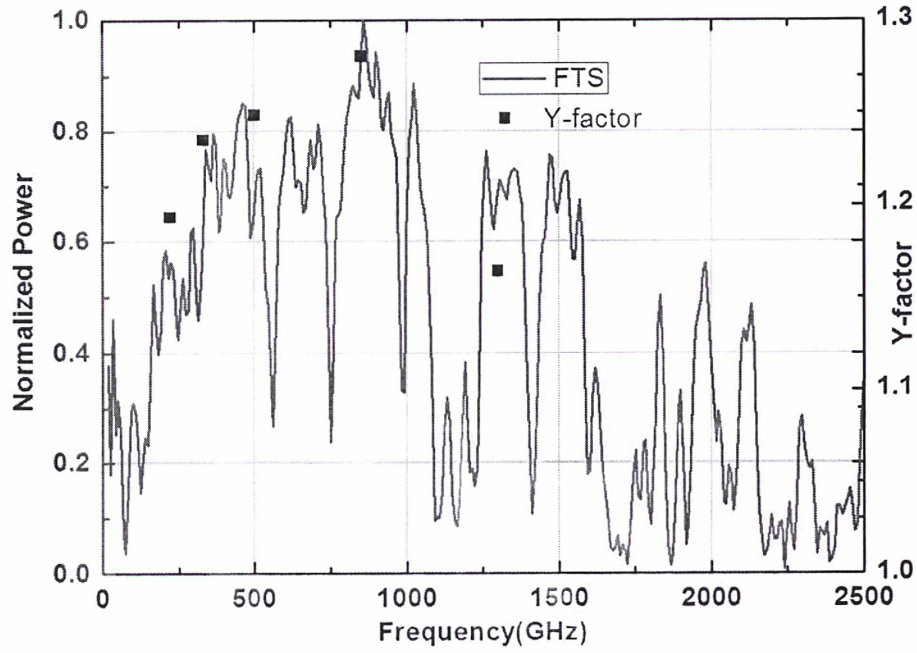


Figure 6.9: Spectral response of the HEB mixer measured in direct detection mode by an FTS (left axis) and in heterodyne mode using the Y-factor method (right axis)

6.5 Conclusion

In this chapter, we have designed and characterized a 0.1-1.5 THz wideband superconducting HEB mixer using integrated lens and spiral antenna. The measured R - T curve shows two superconducting transitions at 5.8 K and 7.4 K respectively. The noise temperature has been measured at five frequencies, the lowest noise appears at 850 GHz. The IF noise bandwidth has been measured at 500 GHz and 850 GHz, the result shows no obvious dependence on RF frequency. We also measured the spectral response of the HEB mixer in direct detection mode by an FTS and in heterodyne mode using the Y-factor method, the heterodyne sensitivity closely follows the spectral response measured with the FTS.

Bibliography

1. J.D.Dyson, "The equiangular spiral antenna", *IRE Trans. Ant.Prop.*, 7, 181, 1959.
2. P. Yagoubov, G. Gol'tsman, B. Voronov, L. Seidman, V. Siomash, S. Cherednichenko, and E. Gershenzon, "The bandwidth of HEB mixers employing ultrathin NbN films on sapphire substrate," in *Proc. of 7th International Symposium on Space Terahertz Technology*, pp. 290-302, 1996.
3. W. Miao, W. Zhang, J. Q. Zhong, S. C. Shi, Y. Delorme, R. Lefevre, A. Feret, and T. Vacelet, "Non-uniform absorption of terahertz radiation on superconducting hot electron bolometer microbridges" *Applied Physics Letters* 104, 052605 (2014); doi: 10.1063/1.4864763.
4. Baselmans, J. J. A., et al. "Direct detection effect in small volume hot electron bolometer mixers." *Applied Physics Letters*, 86.16 (2005): 163503-163503.
5. Sumner P.Davis, "Fourier Transform Spectrometry", *Academic Press* , 2001.
6. <http://www.terahertz.co.uk/>
7. http://en.wikipedia.org/wiki/Planck's_law.

Chapter 7

Conclusions

The objective of this thesis is to develop high sensitivity superconducting HEB mixers around 1.4 THz for the construction of the THz telescope at Dome A on the Antarctic plateau. This research work has concerned mainly the design and the characterization of quasi-optical HEB mixers using integrated lens antenna configuration. Particular efforts have been made to acquire a good understanding of the quasi-optical structure through a thorough and attentive study on the simulation and characterization of the radiation pattern of mixers with integrated lens antenna. Good agreements between simulations and experiments have been obtained and one of the mixers developed during the thesis has demonstrated the state of the art sensitivity at 1.4 THz.

The main achievements during this thesis can be summarized as follows:

- 1) A special vector test system has been developed to measure precisely the dielectric constant of high-resistivity silicon at 77 K and 295 K, a crucial parameter for the lens design. We have then analyzed the effect of this constant on the far-field beam pattern of the quasi-optical superconducting HEB mixer and found that the difference of the silicon permittivity at two temperatures (77 K and 295 K) does affect the simulated far-field beam pattern. So it's important to apply the silicon's permittivity at low temperature in the beam pattern simulation.
- 2) Two simulation methods (MoM/PO and GO/PO) of far-field beam pattern have been compared and analyzed in order to get efficient and reliable design. We found that the MoM/PO method can give a more precise beam pattern than GO/PO method. However, the GO/PO method is still suitable for simulations of electrically large objects which are difficult to be calculated by MoM/PO method. Measurements of beam pattern at 600 GHz have also been performed by both direct far-field method and vector near-field method, both measured results accord well

with simulation. We have also found that the far-field beam pattern transformed from near-field measurement has higher signal-to-noise ratio than the direct measured one. In addition, we have investigated the effect of HEB bias voltage and bath temperature on measured far-field beam patterns. Neither DC bias nor bath temperature affected the profile of mixer's beam-pattern, but both affected the signal to noise ratio.

- 3) A quasi-optical 1.4-THz superconducting HEB mixer using integrated lens/double slot antenna has been successfully developed. Full direct and heterodyne characterizations including R-T curve, noise temperature, conversion gain, beam pattern (far and near field), RF and IF bandwidth are performed. The noise temperature measurement has demonstrated a state of the art sensitivity (600 K) at 1.3 THz. We have characterized the intrinsic frequency response of the HEB device by applying a new method, the RF bandwidth is from 0.8 THz to 1.5 THz. The near-field and far-field beam patterns of this mixer have also been measured, analyzed and compared to the simulation. The simulated far-field beam pattern appears in good agreement with the measured one. Furthermore, the influence of lens' parameters on the performance of this mixer has been investigated. We have found that the noise temperature and frequency response are nearly independent of the lens extension length, but the directivity, Gaussicity and beam-waist width are strongly dependent on the lens extension length.
- 4) A 0.1-1.5 THz broadband superconducting HEB mixer using integrated lens and spiral antenna has been developed and analyzed. The noise temperature has been measured at five frequencies, the lowest noise appears at 850 GHz. The IF noise bandwidth has been measured at 500 GHz and 850 GHz, the result shows no obvious dependence on RF frequency. The measured spectral response of the HEB mixer in direct detection mode by an FTS accords well with that measured in heterodyne mode using the Y-factor method.

In conclusion, this work has provided a further understanding of superconducting HEB mixers and achieved the state of the art sensitivity at 1.4 THz. Hence, the results of this study can be of use and of benefit to the construction of the 5 m terahertz telescope (DATE5) at

Dome A.

Publication

1. K.M. Zhou, W. Miao, Z. Lou, J. Hu, S.L. Li, W. Zhang, S.C. Shi, R. Lefevre, Y. Delorme, and T. Vacelet, "A 1.4 THz Quasi-optical NbN Superconducting HEB Mixer Developed for the DATE5 Telescope," *IEEE Transactions on Applied Superconductivity*, 2015, 25(3): 1-5.
2. K.M. Zhou, Y. Delorme, R. Lefevre, F. Dauplay, A. Feret, T. Vacelet, Z. Lou, and S.C. Shi, "Far-field beam-pattern of a twin-slot HEB mixer at 600GHz," *Proc. SPIE 9275, Infrared, Millimeter-Wave, and Terahertz Technologies III*, 2014: 92750Z-92750Z-7.
3. K. M. Zhou, Y. Delorme, A. Feret, W. Miao, R. Lefevre, T. Vacelet, and S. C. Shi, "Twin slot antenna patterns of a quasi-optical HEB mixer at THz frequencies," *Microwave and Millimeter Wave Technology (ICMMT)*, 2012 International Conference on. Vol.5. IEEE, 2012.
4. K.M. Zhou, W. Miao, J. Hu, S.L. Li, R. Lefevre, Y. Delorme, and S.C. Shi, "Performance of a 1.3-THz Twin-Slot Antenna Superconducting HEB Mixer Integrated with Different Elliptical Lenses," Accepted by APMC 2015.
5. K.M. Zhou, W. Zhang, W. Miao, S.L. Li, and S.C. Shi, "Characterization of a spiral antenna coupled HEB mixer at THz frequency," *7th Europe/UK-China Millimetre Waves and Terahertz Technology Workshop*, 2014.
6. K.M. Zhou, Y. Delorme, A. Feret, R. Lefevre, T. Vacelet, W. Miao, and S.C. Shi, "Beam-pattern Measurements of Superconducting Hot Electron Bolometer Mixer at THz Frequency," *The 7th Terahertz Days Conference*, 2013.
7. S.L. Li, K.M. Zhou, W.Y. Duan, Z.H. Lin, Q.J. Yao, and S.C. Shi, "Effects of Multiple Reflections and Low-Frequency Interferences on Measured Terahertz Fourier Transform Spectra" *Photonics Asia. International Society for Optics and Photonics*, 2012: 856204-856204-6.
8. Z. Lou, J. Hu, K.M. Zhou, W. Miao, and S.C. Shi, "A quasi-optical vector near-field measurement system at terahertz band," *Review of Scientific Instruments*, 2014, 85(6): 064702.

9. W. Zhang, W. Miao, K.M. Zhou, S.L. Li, Z.H. Lin, Q.J. Yao, and S.C. Shi, "Heterodyne Mixing and Direct Detection Performance of a Superconducting NbN Hot-Electron Bolometer" *Applied Superconductivity*, IEEE Transactions on, 2011, 21(3): 624-627.
10. W. Miao, W. Zhang, K.M. Zhou, K. Zhang, W.Y. Duan, Q.J. Yao, and S.C. Shi, "Direct Measurement of the Input RF Noise of Superconducting Hot Electron Bolometer Receivers" *Applied Superconductivity*, IEEE Transactions on, 2013, 23(3): 2300104-2300104.
11. W. Miao, W. Zhang, K.M. Zhou, S.L. Li, K. Zhang, W.Y. Duan, and S.C. Shi, "Phase-locking of a terahertz solid-state source using a superconducting hot-electron bolometer mixer" *Superconductor Science and Technology*, 2013, 26(8): 085005.
12. W. Miao, W. Zhang, K.M. Zhou, Q.J. Yao, Y. Delorme, R. Lefevre, and S.C. Shi, "Direct detection behavior of a superconducting hot electron bolometer measured by Fourier transform Spectrometer" *Photonics Asia 2010. International Society for Optics and Photonics*, 2010: 78540B-78540B-6.
13. W. Zhang, W. Miao, S.L. Li, K.M. Zhou, S.C. Shi, J.R. Gao, and G.N. Goltsman "Measurement of the Spectral Response of Spiral-Antenna Coupled Superconducting Hot Electron Bolometers," *Applied Superconductivity*, IEEE Transactions on, 2013, 23(3): 2300804-2300804.
14. J. Li, S.C. Shi, D. Liu, K.M. Zhou, M.J. Wang, T.J. Chen, C.W. Chen, W.C. Lu, C.P. Chiu, and H.H. Chang, "Noise and Bandwidth of 0.5-THz Twin Vertically Stacked SIS Junctions," *Applied Superconductivity*, IEEE Transactions on, 2011, 21(3): 663-666.

